

**Development of electrocatalyst with better efficiency:
Revisiting
methanol oxidation process**

by

Pooja Shrikant Deshpande

10CC17A26002

A thesis submitted to the
Academy of Scientific & Innovative Research
for the award of the degree of
DOCTOR OF PHILOSOPHY
in
SCIENCE

Under the supervision of

Dr. BLV Prasad



CSIR-National Chemical Laboratory, Pune

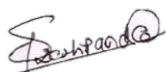


Academy of Scientific and Innovative Research
AcSIR Headquarters, CSIR-HRDC campus
Sector 19, Kamla Nehru Nagar,
Ghaziabad, U.P. – 201 002, India

April, 2023

Certificate

This is to certify that the work incorporated in this Ph.D. thesis entitled, “**Development of electrocatalyst with better efficiency: Revisiting methanol oxidation process**”, submitted by Pooja Shrikant Deshpande to the Academy of Scientific and Innovative Research (AcSIR), in partial fulfilment of the requirements for the award of the Degree of Doctor of Philosophy in Science, embodies original research work carried-out by the student. We further certify that this work has not been submitted to any other University or Institution in part or full for the award of any degree or diploma. Research material(s) obtained from other source(s) and used in this research work has/have been duly acknowledged in the thesis. Image(s), illustration(s), figure(s), table(s) etc., used in the thesis from other source(s), have also been duly cited and acknowledged.



(Signature of Student)

Pooja Shrikant Deshpande

Date: 05-April-2023



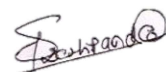
(Signature of Supervisor)

Bhagavatula L. V. Prasad

Date: 05-April-2023

STATEMENTS OF ACADEMIC INTEGRITY

I, Pooja Shrikant Deshpande, a Ph.D. student of the Academy of Scientific and Innovative Research (AcSIR) with Registration No. **10CC17A26002** hereby undertake that the thesis entitled “**Development of electrocatalyst with better efficiency: Revisiting methanol oxidation process**” has been prepared by me and that the document reports original work carried out by me and is free of any plagiarism in compliance with the UGC Regulations on “Promotion of Academic Integrity and Prevention of Plagiarism in Higher Educational Institutions (2018)” and the CSIR Guidelines for “Ethics in Research and in Governance (2020)”.



Signature of the Student

Date: 05-April-2023

Place: Pune

It is hereby certified that the work done by the student, under my/our supervision, is plagiarism-free in accordance with the UGC Regulations on “Promotion of Academic Integrity and Prevention of Plagiarism in Higher Educational Institutions (2018)” and the CSIR Guidelines for “Ethics in Research and in Governance (2020)”.

Signature of the Supervisor



Name: Bhagavatula L. V. Prasad

Date: 05-April-2023

Place: Pune

This thesis is dedicated to
my parents

For their never-ending affection, support, and encouragement

Acknowledgements

There are so many people whose encouragement, inspiration, and support are critical to attaining significant life objectives, especially if they involve portions of achieving one's most cherished dreams. My thesis is a big aim for me, and I am grateful to many people for their support and good wishes as I embark on this journey. I want to take this opportunity to thank everyone who, directly or indirectly, contributed to the scientific effort described in this thesis. I thank God for the blessings in my life, for giving me this opportunity, and for giving me the ability to succeed.

I would like to offer my heartfelt gratitude to my thesis supervisor, **Dr. BLV Prasad**, for his patience and assistance throughout my PhD program. I was concerned about how my medical condition might affect my ability to conduct research and obtain my degree. **Dr. BLV Prasad**, on the other hand, was not only accommodating, but also went above and above to ensure that I got the resources and assistance I needed to succeed. He was always willing to listen and offer assistance when I needed it. I am deeply grateful for his compassion and understanding. He has been a constant source of inspiration, pushing me to think more deeply about my research issues and leading me through the many stages of the research process. I am grateful to him for providing me with intellectual independence. He let me to pursue my research topics in my own unique way, while always offering the support and direction I required to stay on track.

Thank you for your constant support and understanding, sir. I could not have finished this degree without your support and encouragement, and I am appreciative for everything you have done for me.

I would also want to thank the members of my doctoral advisory committee, **Dr. S.K. Asha**, **Dr. Sreekumar Kurungot**, and **Dr. J. Nithyanandhan**, for their time, sound advice, and encouragement. I'd like to thank Dr. Ashish Lele, the current director of the CSIR-NCL, and Dr. Ashwini Kumar Nangia, the previous director, for enabling me to work at this prestigious organization and for giving the resources I required to do the research.

I am extremely grateful to Dr. T. Ajithkumar, Head of the Physical and Materials Chemistry Division, Dr. P. A. Joy (previous HoD) for their great assistance during my Ph.D. Thank you to the division staff members who aided me with routine office work. I want to thank the entire

administrative and non-teaching staff of CSIR-NCL (Pawar kaka, Rahil, Sunil, Geetanjali) for all of their assistance and support over the years.

I would like to thank everyone at NCL's Center for Materials Characterization division who has assisted me over the years. I sincerely thank Mr. S. S. Deo, Mr. R. S. Gholap, Venkatesh, Sheetal, Chetan, Tushar, Medha, and Shurti for their rapid support with the XPS, TEM, HRTEM, FESEM, and SEM measurements. Many thanks to Chetan Sir for accommodating my request for urgent slots.

I owe to thank **Dr. D.S. Reddy** (Organic Chemistry division, NCL Pune) for providing me with my initial exposure and experience in this laboratory and research during my B. Sc. and **Dr. Sunil Kulkarni** (S.P. College, Pune) for his assistance and guidance during my M.Sc. dissertation.

I would like to acknowledge the financial support provided by **DST-INSPIRE**, which enabled me to pursue my PhD studies.

I want to express my profound gratitude to the members of SAAM group, my lab mates Dr. Arun, Dr. Pravin, Dr. Poulami, Dr. Vijay, Dr. Shankar, Dr. Kaustav, Dr. Gargi, Dr. Abhijit, Dr. Jayesh, Mayur, Ashish, Hari, Maya, Arun, Umasharan and Viresh for their encouragement, direction, and contributions to my research. The lab members assistance and support made the study presented in this thesis possible. I would like to thank **Dr. Shankar** for his significant assistance and experience. He was always ready to answer my queries, troubleshoot problems, and advise on experimental design and analyses. Thank you to everyone at the SAAM group for making my time in the lab so meaningful and fulfilling.

I specially want to thank **Dr. Vijay Chaudhari**, who trained and assisted me in the usage of specialist equipment and techniques. His experience and direction were critical in assisting me in carrying out the studies reported in this thesis. I would like to express my heartfelt gratitude to **Dr. C.K. Subash** for his assistance and direction in writing the thesis.

I'd want to thank all of my NCL friends, including Mahindra, Amrish, Sanket, Mayur (Jr), govind, Pratik, Himanshu, Ravi, Vinita, Inderjeet, as well as my girls Priya, Priyanka, Supriya (helping for assisting in ISPIRE-fellowship), Amrita, Kalyani, Manali, Monika, Anuradha, Kranti and Chandan for such a lovely memory.

I would thanks to my childhood friend **Ankita** for her unending encouragement and support. I will be eternally grateful to her for what she has done for me. I want to acknowledge my in-

laws, **Shital Nardekar and Lata Nardekar** for their help and understanding. They have been like second parents to me, always willing to lend a helping hand or offer sound advice. Their continuous support has been a source of comfort to me during this journey. I would like to thank my sister-in-laws **Samta and Akshaya** for being with me at difficult times and encouraging me to do good work.

Finally, I would like to express my gratitude to my parents **Shrikant and Vijaya Deshpande**. Their love and care have provided me with courage and motivation, and I could not have finished this journey without them. Love you Amma for your unconditional love and support. I always want to be like you. I would like to thank my lovely and supportive brother **Prasad**, my little stars **Rihaunsh and Ashvi** for making me smile and extended family for their support, encouragement, and understanding. Their faith in me has been a constant source of motivation, and their encouragement has given me the confidence to pursue my aspirations.

I am eternally grateful to my husband, **Dr. Swapnil Nardekar**, for his understanding, patience, and sacrifice. Throughout this long and difficult process, he has been my rock and cheerleader, always available to provide a listening ear or offer words of support. His faith in me has been the fire that has kept me going through the most difficult moments. Thank you so much, Swapnil, for not letting me give up on my aspirations and for giving me wings to fly high. I appreciate you making special meals for me and other small favours. I'd like to thank all of my teachers, from elementary school to graduate school, specially to **Kedar sir** and **Kodeshwar mam** and **Belsare sir** (my class teachers) for instilling in me good morals and knowledge. I could not have finished my research without the help of all of these lovely folks.

Pooja S. Deshpande

Table of Contents

Chapter-1: Introduction

1.1 Introduction	(2)
1.2 Fuel cell and its type.....	(2)
1.3 DMFC	(4)
(a) Concept and principles of DMFC	(5)
(b) Type of DMFC and drawbacks	(6)
1.4 Methanol oxidation reaction (MOR)	(8)
1.5 Electrocatalytic study.....	(10)
1.6 Statement of the problem	(13)
1.7 Objective of the thesis	(13)
(a) Methodology	(13)
1.8 Outline of the thesis	(13)
1.9 References	(15)

Chapter-2: Revisiting MOR mechanism

2.1 Introduction	(21)
2.2 Experimental	(23)
2.3 Result and Discussion	(24)
(a) Intermediate species responsible for the origin of I_b	(24)
(b) Nature of intermediate species	(26)
(c) Factor influencing I_b	(28)
2.4 Conclusion	(30)
2.5 References	(32)

Chapter 3: New descriptor of efficiency and its validation with commercially available catalysts

3.1 Introduction	(36)
3.2 Experimental	(37)
3.3 Electrochemical measurements	(37)
3.4 Result and Discussion	(38)
3.5 Conclusion	(42)
3.6 Reference	(43)

Chapter-4: Improved performance of Co-Pt Alloy with a trace amount of Mn

4.1 Introduction	(46)
4.2. Experimental	(47)
(a) Synthesis of nanoparticles	(47)
(b) Characterizations of $Pt_x(MnCo)_{1-x}$ nanoparticles	(47)
(c) Electrochemical measurements	(48)
4.3. Result and Discussion	(49)
(a) Crystal structure and microstructural analysis	(49)
(b) Electro-catalytic properties of $Pt_{100-x}(MnCo)_x$ alloys	(55)
4.4 Validation of new criterion (I_f/I_{Co})	(60)
4.5. Plausible explanations for elevated MOR activity of $Pt_{100-x}(MnCo)_x/C$ catalysts...	(62)
4.6. Conclusion	(64)

4.7. Reference	(65)
----------------------	------

Chapter-5: Highly efficient Pt_x(CoNiM)_{100-x} quaternary anode catalysts for methanol electrooxidation

5.1 Introduction	(71)
------------------------	------

5.2. Experimental	(72)
-------------------------	------

(a) Synthesis of nanoparticles	(72)
--------------------------------------	------

(b) Characterizations of Pt _x (CoNiM) _{100-x} alloy	(72)
---	------

(c) Electrochemical Measurements	(73)
--	------

5.3. Result and Discussion	(74)
----------------------------------	------

(a) Crystal Structure and Microstructural Analysis	(75)
--	------

(b) Electro-catalytic properties of Pt _x (CoNiM) _{100-x} alloys	(76)
---	------

5.4. Conclusion	(78)
-----------------------	------

5.4. Reference	(79)
----------------------	------

Chapter-6: Final Thoughts and Future Prospects

6.1 Summary of the Thesis	(82)
---------------------------------	------

6.2 Scope for future work	(83)
---------------------------------	------

6.3. Methodology	(84)
------------------------	------

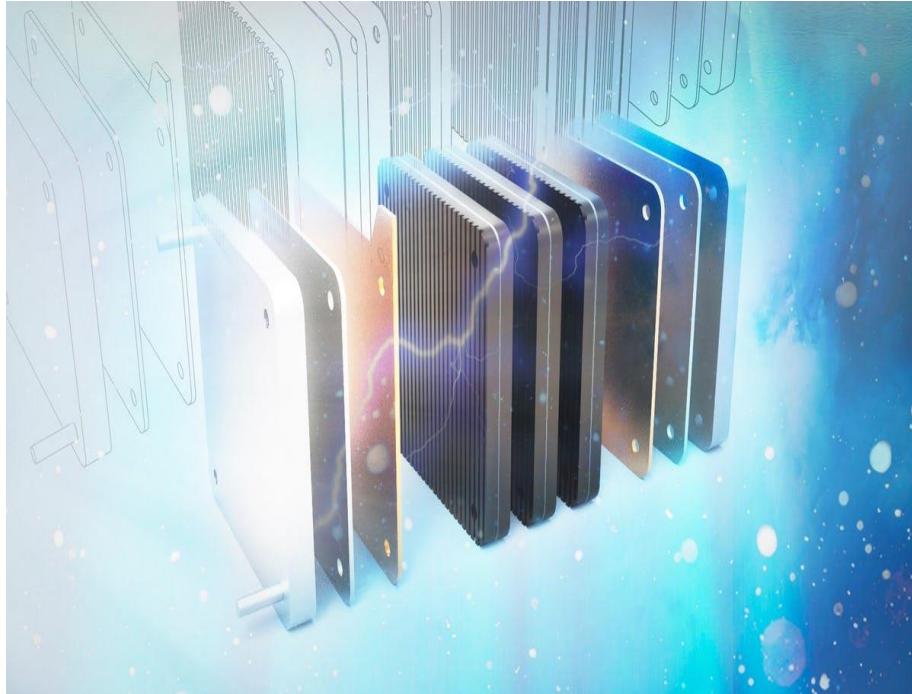
(a) Preparation of MEA	(84)
------------------------------	------

6.4. Reference	(86)
----------------------	------

Abstract and List of publication	(89)
--	------

Chapter-1

Introduction



(Taken from <http://inogen.com.tr/en/p/fuel-cell>)

The backdrop of the research done for this thesis is presented in this chapter, along with information on the current energy crisis presenting fuel cells as an alternative, sustainable, and environmentally friendly source of energy. One class of such fuel cells is direct methanol fuel cells (DMFCs) which is the central topic of this thesis. In particular, the anode catalyst for methanol oxidation reaction (MOR) employed in DMFCs is our main focus. With this background, this Chapter presents the factors that affect DMFC efficiency, especially MOR, and also discusses the main challenges being faced by researchers. Finally, the motivation to carry out the work embodied in this thesis and the objectives of our work are mentioned.

1.1 Introduction:

The search for alternative energy sources that can support the world's rising population and being environmentally friendly simultaneously is at the forefront of research in the framework of increased awareness of sustainable development.[1] Concurrently the need for energy is also intensifying due to both the growing human population and the rising modernization of technology. The vast majority of electricity we use today is generated by fossil fuels. Internal combustion engines (ICE) powered by fossil fuels account for over 90% of global transportation. Using a lot of fossil fuels raises the amount of greenhouse gases in the atmosphere dramatically.[2-4] In addition to such environmental concerns, it is claimed that fossil fuels are unsuitable for long-term use due to limited supply, geopolitical constraints, and high extraction costs.[5] The availability of other renewable energy sources, such as sun and wind, relies greatly on the local climate and surroundings, making them unavailable whenever needed. The bulk of electronic devices nowadays, such as chargers for mobile phones, cameras, computers, and other devices, require energy 24/7 and 365 days. Currently, all these devices depend in the form of rechargeable batteries that are charged with an external electrical power source.[6] Producing rechargeable batteries from mined minerals (such as lithium, lead, manganese, zinc, silver, nickel, and mercury) has social and environmental consequences because natural resources are limited.[7] As a result, increasing our dependency on such systems may have an additional adverse influence. Such growing or never-ending demands of energy and unsatisfactory solutions available today are making researchers to seek alternative energy sources. The fuel cell has the potential to provide solution to this problem addressing most of the concerns raised above.

1.2 Fuel cell and its type:

Fuel cell research began in the 1800s, but it has become increasingly popular in the past three decades. A fuel cell is an electrochemical device that, in the presence of a catalyst, transforms the chemical energy of a fuel (such as hydrogen, methanol, etc.) and an oxidant (such as air, pure oxygen) into electricity, heat, and water.[8] The non-polluting nature of fuel cells makes them highly appealing.[9,10] Anode, cathode, and electrolyte are the three main components, which constitute a fuel cell. The fuel and oxidant are constantly delivered to the anode and cathode chambers, respectively. Power is generated by the chemical reaction that occurs at the electrode of a fuel cell.

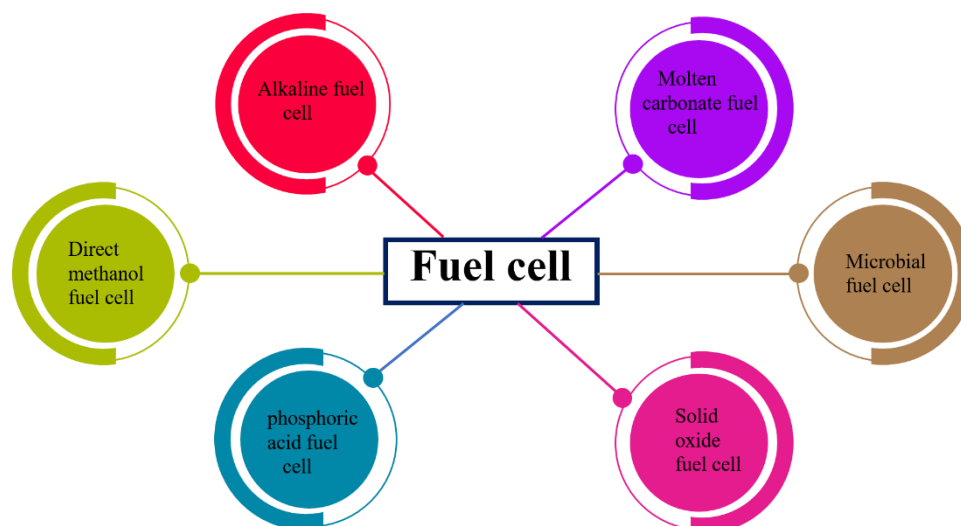


Figure 1.1: Types of fuel cell.

As of right now, there are six main categories of fuel cells (please see figure 1.1 and table 1.1), including (1) proton exchange membrane fuel cell (PEMFC), which also includes direct methanol fuel cell (DMFC), (2) alkaline fuel cell (AFC), (3) phosphoric acid fuel cell (PAFC), (4) solid oxide fuel cell (SOFC), (5) molten carbonate fuel cell (MCFC), and (6) microbial fuel cell (MFC).[16-21] Among these, PEMFC, DMFC, AFC, PAFC, and MFC can be run at low temperatures between 50 and 200 °C and are also known as low-temperature fuel cells, whereas MCFC and SOFC function at high temperatures between 650 and 1000 °C and are known as high-temperature fuel cells.

In the last twenty years, the interest in all types of fuel cells increased dramatically not only due to their high efficiency and zero emission of potentially pollutant gases but also due to their outstanding simplicity and absence of moving parts which make them a potential alternative to ICEs.[11]The potential uses of fuel cells range from permanent power generation in the megawatt range to portable devices that run on a few watts, such as mobile, laptop computers.[12] Depending on the application, the fuel cell may use hydrogen, alcohol, methane, and different organic and inorganic reducing agents such as hydrazine and H₂S. The most often utilized of these is hydrogen. However, any hydrocarbon or other hydrogen-containing fuel that breaks down into hydrogen either thermally or catalytically can also be used as fuel.

The majority of automotive utilize PEMFC technology, which is powered by hydrogen. Although hydrogen is the best fuel for PEMFCs, commercialization is hindered by the clean generation of hydrogen, challenges related to on-board storage, and dearth of consumer H₂

transportation facilities. H_2 consumes up to 3000 times more space than an equivalent volume of gasoline, even at 1000 bar pressure.[13-14] A benefit of using liquid fuel over hydrogen is that it is easier to store, transport, and has a higher energy density.[15-17]

	Low Temperature Fuel Cell (Catalyst Required)			High Temperature Fuel Cell (Catalyst not required)		
Type	PMFC	DMFC	AFC	PAFC	SOFC	MCFC
Electrolyte	Ion exchange polymer membrane	Polymer membrane	Potassium hydroxide	Phosphoric acid	Ceramic	Molten carbonate
Operating temperature	60-90 °C	60-130 °C	60-90 °C	190-210 °C	800-1000 °C	650 °C
Power range	Up to 250 kW	< 10 kW	Up to 20 kW	> 50 Kw	> 200 kW	> 1 MW
Fuel	Hydrogen	Methanol	Hydrogen	Natural gas, biogas, Hydrogen	Natural gas, biogas, Hydrogen	Natural gas, biogas, Hydrogen

Table 1.1: Type of fuel cell classified based on operating temperature and fuel used in it.

1.3 DMFC:

Among different types of fuel cells, DMFCs are attracting a lot of attention due to their low operating temperature, reasonably less pollution, high reliability, low noise, quick refueling, facile charging, and easy maintenance. As implied by its name, DMFCs use methanol as fuel.[18-20] In DMFCs, methanol is injected straight into the cell and there is no need to convert it into hydrogen. Anodes extract hydrogen by dissolving methanol in water during a chemical process, which reduces the overall cost of fuel cells due to the avoidance of a reformer. Furthermore, methanol is an appealing fuel due to its low cost, simplicity of carrying and storing, high level of energy density, and, most significantly, the fact that it can be made from renewable biomass or natural gas is all advantages. One of the end products of "liquid sunshine," which is made from carbon dioxide (CO_2) and solar energy, is methanol. This makes it crucial for the future solution of energy and environmental issues.[21] In comparison to compressed hydrogen at 1000 bar, methanol is much more affordable (per unit of energy) and

has a better volumetric and gravimetric energy density (even higher in comparison to liquid hydrogen).[22-23] Methanol has a volumetric energy density of 17,900 kJ/L, which is about three times more than hydrogen. Interestingly, 99 g of hydrogen are present in one litre of methanol as opposed to 71 g in one litre of liquid hydrogen. "Methanol in its own right is an excellent fuel in liquid form as it can be mixed with gasoline in any proportion, easily stored, and transported," said Dr. George A. Olah, recipient of the 1994 Nobel Prize in Chemistry. "It can be considered as a universal energy carrier that could eventually replace all the hydrocarbons and ethanol".[24] Thus, this remarkable property of methanol makes DMFC an excellent power source for electronic vehicles and portable electronic applications.

(a) Concept and principles of DMFC:

Fundamentally, DMFC is a PEMFC with methanol as fuel. The key component of DMFC is the membrane electrode assembly (MEA), where anode and cathode are separated by polymer electrolyte membrane (PEM), where Nafion is the most frequently used membrane.[25] In DMFC, two different types of reactions often take place: one, the methanol oxidation reaction (MOR), that happens at the anode, while the other, the oxygen reduction reaction (ORR), occurs at the cathode (Please see figure 1.2). In DMFC, water and methanol mixture are directly fed to the anode as a fuel where the methanol oxidised to CO_2 , releasing 6 H^+ and 6 e^- in the process. There is no emission of harmful substances such as nitrous oxide and sulphur oxide therefore it is less harmful to the environment. As MOR is a 6 e^- process it involves a lot of intermediates like carbon monoxide (CO), formaldehyde, formic acid, etc. The formation of these intermediates during oxidation of methanol makes overall MOR sluggish.[26] The proton generated during the MOR then moves from anode to cathode across a Nafion membrane, while at the same time, the generated electrons also flow from anode to cathode through an external circuit. At the cathode, oxygen molecule reacts with the electron and proton to generate water. When methanol is oxidised by OH^- ions in an alkaline fuel cell, water is produced at the anode rather than the cathode, and OH^- ions are transported from the cathode to the anode in place of protons.

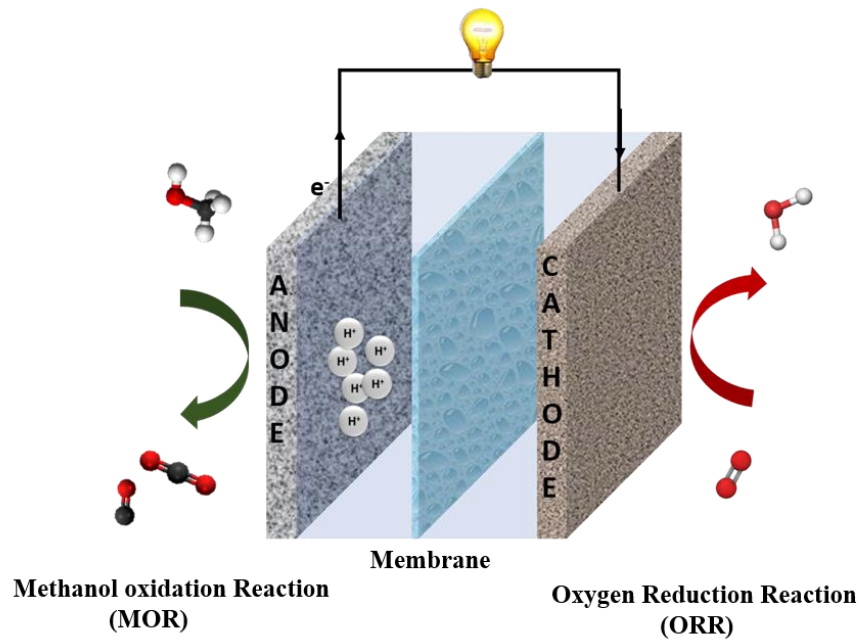
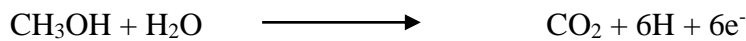


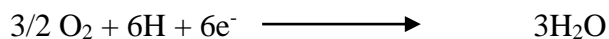
Figure 1.2: A schematic of DMFC operation with a polymer electrolyte membrane as the electrolyte.

The following is a representation of the reaction in an acidic and a basic media.

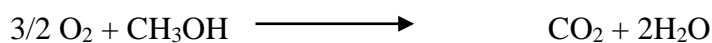
Anode reaction:



Cathode reaction:



Overall reaction:



The DMFC has a 1.21 V thermodynamic potential and a 96.4% thermodynamic conversion efficiency, which is substantially higher than ICE.[27]

(b) Type of DMFC and drawbacks:

The DMFC are classified into two types.

1. Passive DMFC.
2. Active DMFC.

In passive DMFC, the reactant, such as methanol on the anode side and oxygen on the cathode side, are provided up to the catalyst layer and the reaction products, such as CO₂ and water, are taken out of the cell by passive methods, such as passive diffusion, passive capillary action, and passive natural convection, etc. In active DMFC, the fuel and oxygen are supplied by external supply, such as pump, blower, etc. Due to its straightforward design, compact size, and lower parasitic power losses than active DMFC, passive DMFC draws a lot of interest. [28-30] Passive DMFC is an excellent replacement for traditional batteries since it does not require any additional or auxiliary components.[31] Thus DMFCs have the potentiality to replace batteries since, in theory, methanol has a higher specific energy density than some of the finest rechargeable batteries, such as lithium-polymer and lithium-ion polymer systems. This indicates the long operation time for portable devices and more power will be available in DMFC-based devices to meet consumer demands. For example, while rechargeable batteries need an hour to refill a depleted power pack, DMFCs would just need a minute to restore the fuel.[32-34] Despite all these benefits, there are still a few obstacles that need to be removed before DMFC can replace the current battery and be widely used as a source for portable devices.

It is important to understand the disadvantages of DMFC since the commercialization or advancement of any system is critically dependent on knowing the limitations of current science and technology. As a result, it is critical to emphasize the areas where change would be particularly beneficial. DMFC has the following drawbacks:

1. As MOR is the rate-determining step in DMFC, the total efficiency of the DMFC is dependent on the catalyst utilized as the anode where MOR occurs. The anode's activity must be increased, either by increasing the working temperature of the fuel cell, which is currently limited by the use of a nafion membrane, or by identifying improved electrocatalysts for MOR.
2. Pt is the most frequently used catalyst in DMFCs. The Pt loading currently being used is closer to 2 mg/cm² to obtain an acceptable power density for DMFC. However, such high dependency on Pt ultimately drives up the price of DMFC overall. It cannot enter the market unless Pt loading is less than 1 mg/cm². [35]
3. To balance water sensitivity and decrease methanol crossover, which is the major issue that results in mix-potential and lowers DMFC efficiency, the membrane characteristics must be improved.

It is in this premise that we started working on DMFCs with a particular emphasis on MOR.

1.4 Methanol oxidation reaction (MOR):

In DMFC, MOR takes place at the anode. Pt is the most commonly used anode catalyst in DMFC for MOR. The outstanding electrocatalytic activity of Pt towards MOR is believed to derive from its unique electronic structure i.e. $5d^96s^1$. Due to this electronic structure, it could either easily gain or lose electrons from or to the ligand, which in this case happens to be methanol and other intermediates formed during the reaction. Here, the interaction between Pt and ligand should be moderate for an efficient reaction. In a detailed study, Peng et al. have shown that the high performance of Pt is related to the increase of d-orbital vacancies and high state of density around the Fermi level.[36]

It is well known that chemical/electrochemical reactions involve one or two intermediates. However, during the oxidation of methanol, many intermediates such as CO_2 , formaldehyde, formic acid, etc have been seen under the same reaction conditions.[37]

This finding implies that reactions can take many different routes, including

1. Step by step dehydrogenation to adsorbed CO which on oxidation gives CO_2 (Indirect path);
2. Formation of CO_2 without formation of CO (Direct path);
3. Partial oxidation to formic acid and/or formaldehyde

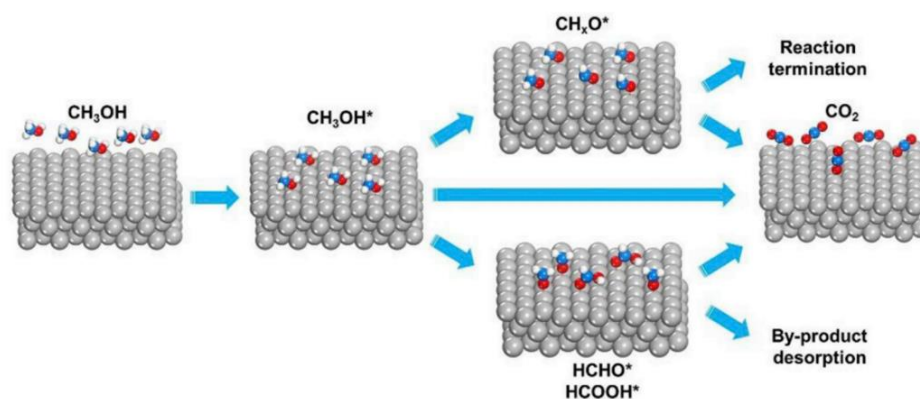
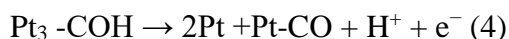
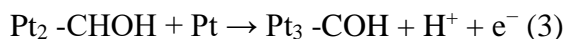
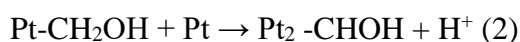


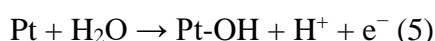
Figure 1.3: An illustration of the process of methanol oxidation reaction occurring on anode catalyst (taken from reference 21).

The schematic (Figure 1.3) represents the parallel pathways of MOR that are proposed in literature. From this it is clear that MOR involves three steps: methanol dehydrogenation, water degradation, and removal of CO_2 . Some of the processes/reactions that occur during these three steps are captured below.

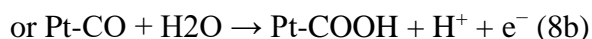
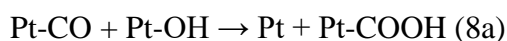
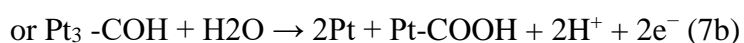
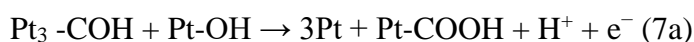
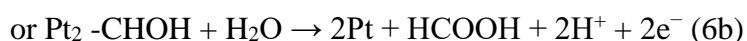
Methanol dehydrogenation to produce adsorbed intermediates



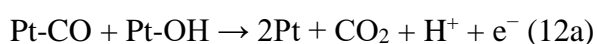
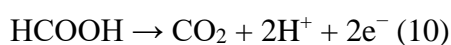
Water degradation to generate oxygenated species



Carbon contained species removal to liberate active Pt sites



Carbon dioxide formation to complete the overall reaction



Interestingly, all the above reactions are possible in MOR.[35] As MOR involves 6 e⁻ transfer, it is very complicated reaction and understanding of the mechanism is still lacking. In addition, considerable ambiguities also exist regarding the rate of the reaction and also with respect to the intermediates present on the surface.

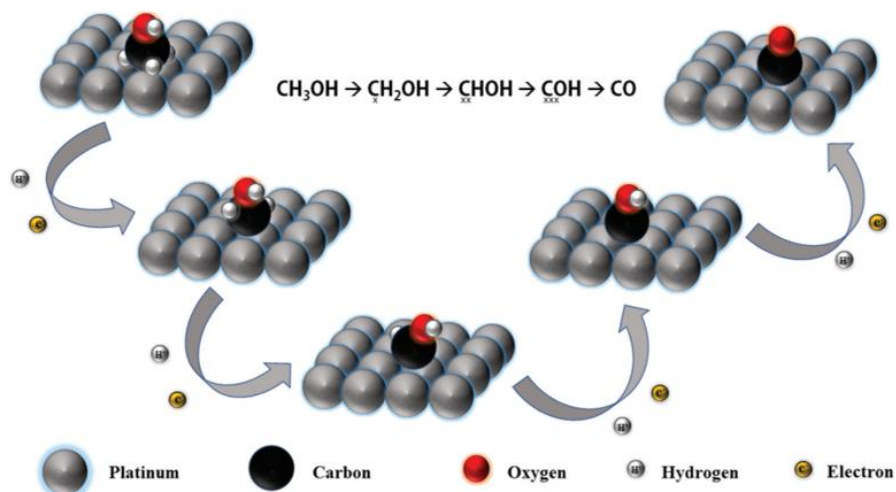


Figure 1.4: An illustration of the formation of CO on platinum surface by successive stripping of hydrogen atoms during MOR (taken from reference 41).

Kunimatsu et al. were the first to make a significant contribution to the understanding of MOR. They claimed CO is the most prominent intermediate species formed during MOR [38]. Buschmann et al.[39] and Willsau et al.[40], on the other hand, employed in-situ techniques to analyze the MOR intermediates based on the number of electrons and concluded that CHO is the real intermediate not CO. These are only two of the major ambiguities that are reported. More details of these ambiguities are further discussed in Chapter-2.

Among various intermediate formed during MOR, CO is believed to be adsorbed on the platinum surface, blocking many active sites of platinum and making them unavailable for further oxidation of methanol under the DMFC operating condition.[41] This phenomenon is known as CO poisoning (figure 1.4). To address the issue of CO poisoning, alloying of Pt with other metals (M) like Ru, Co, Cu, Ni, Fe, and Sn etc. is suggested. Most commonly used bimetallic catalyst for MOR is RuPt/C.

1.5 Electrocatalytic study:

Unlike in many other devices where the catalytic efficiency has to be tested in the true device architecture, in case of electrocatalysis cyclic voltammetry has been widely used to analyse the electrocatalyst and determine its efficacy. Typically, two oxidation peaks make up the cyclic voltammogram (CV) of MOR (Figure 1.5): I_f in the forward scan (anodic scan) and I_b in the backward scan (cathodic scan). I_f represents the oxidation of remaining unoxidized CO (from the second cycle) on the surface together with the methanol to CO_2 conversion.

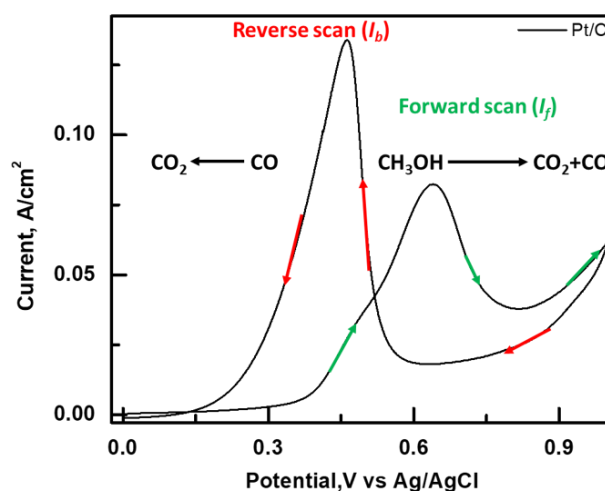


Figure 1.5: Cyclic voltammogram recorded using 20% Pt/C in 0.5 M H₂SO₄ and 1 M methanol solution (Scan rate: 50 mV/s).

On the other hand, I_b represents the oxidation of residual methanol. The electrocatalytic activity of the catalyst is quantified in terms of electrochemical surface area (ECSA), mass activity or specific activity, and the I_f/I_b ratio. A high I_f/I_b ratio result has been implicated to represent an electrocatalyst that is more resistant to CO poisoning which has been put forward by Liu et al. based on the MOR mechanism proposed by Manoharan and Goodenough in 1992.[42] Although many researchers still use this I_f/I_b criterion to predict the efficiency of the catalyst many researchers disagree with this as they consider the I_b peak to be associated with other intermediates and not CO. Hence the validity of the I_f/I_b criterion is under tremendous scrutiny. The following table (1.2) shows the ambiguity in the CV analysis for MOR. These ambiguities are further discussed in detail in Chapter-2.

Despite great progress made in the application of bimetallic alloys as MOR catalysts, a material that displays better activity and durability than commercial Pt-based catalysts is still elusive. Recently, few reports claimed that addition of a small quantity of another metal to the bimetallic system can effectively enhance the durability of Pt-based bimetallic catalysts making it better tolerant to CO poisoning.[50-51] In addition, ternary Pt-based alloy is likely to show better activity than a single or bimetallic alloy due to change in the electronic and structural property of Pt.[52] Therefore, it is expected that trimetallic alloys of the variety PtMX (where M is transition metal) could further enhance the durability as well as display better electrocatalytic performance. To make DMFCs commercially viable, researchers are still exploring this topic.

Year	Technique used	Assumption	Reference
1992	CV	<ul style="list-style-type: none"> ▪ I_f and I_b have a different chemical origin. ▪ I_f/I_b is actually a criterion to study poisoning. 	Ref-42
2012	in-situ SEIR	<ul style="list-style-type: none"> ▪ I_f and I_b share the common chemical origin. ▪ I_f and I_b are due to oxidation of freshly adsorbed methanol. 	Ref-43
2016	CV	<ul style="list-style-type: none"> ▪ I_b is due to methanol oxidation synchronized with reduction of metal oxide. 	Ref-44
2016	EIS	<ul style="list-style-type: none"> ▪ I_b is not related to the residual intermediate CO. (Depends on the coverage of free pt surface available for methanol reaction.) 	Ref-45

Table 1.2: Ambiguity in the CV analysis for MOR.

The I_f/I_b criteria also fail and cannot be used for those catalysts where the peak during the backward scan is absent. The table 1.3 contains some examples.

	Catalyst used	Potential window	Observation	Reference
1	RuPt/CNT	0-0.6 V	No reverse peak	Ref-46
2	CO_xCu_y/CNF	0-1 V	No reverse peak	Ref-47
3	Ni polyhedral NCs	0-1 V	No reverse peak	Ref-48
4	Ni-B-Co	0-1 V	No reverse peak	Ref-49

Table 1.3: Problems associated with I_f/I_b criteria.

It is clear from the preceding discussion that there are some issues with the commercialization of DMFCs, primarily owing to catalyst designing which critically depends on the proper understanding of MOR mechanism. The development of MOR catalyst is hampered by the uncertainty around the MOR mechanism, thus we took this as a problem statement and chose to thoroughly investigate the MOR mechanism to develop superior electrocatalyst.

1.6 Statement of the problem:

It is in this context that we formulated the following objectives that we wanted to achieve during the course of work carried out as part of this thesis.

1.7 Objective of the thesis:

- (1) Understanding the methanol oxidation reaction mechanism.
- (2) To find better descriptor of efficiency and its validation with commercially available catalysts.
- (3) Development of new catalysts.

(a) Methodology:

The most active and extensively researched material, commercial Pt on carbon (20% Pt/C), was selected as the electrocatalyst for the experiment carried out to gain deeper insights of MOR mechanism. In order to comprehend the nature and function of intermediate species involved in MOR, we conducted a systematic CV experiment on Pt/C. By choosing the proper potential range and scan direction, the origin of reverse peak I_b was investigated. We deduced from this experiment that I_b is due to the oxidation of CO, and the CO stripping experiment supported this conclusion. Additionally, it was determined that the CO produced during the oxidation of methanol behaved in a diffusion-controlled manner, negating its full responsibility for the adsorption-based electrode poisoning. Therefore, we concluded that it would be inappropriate to evaluate the electro-catalyst performance in MOR using the I_f/I_b paradigm.

We attempted to determine the criteria to assess the poisoning of the catalyst during MOR after successfully examining the MOR process. We developed a novel criterion that addresses the surface adsorption of CO by conducting a straightforward experiment based on the suggested mechanism. We also used catalysts that are readily accessible in the marketplace to validate this requirement. Finally, based on experimental results and fundamental information from CV analysis, we synthesized new catalysts that exhibit improved activity and stability for MOR. With the use of UV, PXRD, and electron microscopy, the findings were analysed.

1.8 Outline of the thesis:

The thesis, "**Development of electrocatalyst with better efficiency: Revisiting methanol oxidation process,**" would combine all of the aforementioned findings as well as the gradual development of the various materials. There are four separate chapters in this thesis.

Following the chapter titles are short summaries of each chapter.

Chapter-1: Introduction to DMFC and MOR.

Brief background of the work and the motivation to carry out the work embedded in the thesis are included in this chapter.

Chapter-2: Revisiting MOR mechanism.

This chapter focuses on resolving existing controversy related to the mechanism for MOR. Based on experimental findings, a new mechanism has been proposed for MOR.

Chapter-3: Establishing a new efficiency descriptor for MOR and its validation with commercially available catalysts.

This chapter mainly focuses on the lacunae present in existing criteria (I_f/I_b) to judge CO poisoning and ways to overcome it by proposing new criteria.

Chapter-4: Improved performance of Co-Pt Alloy with a trace amount of Mn.

In this chapter, we show the effect of a trace amount of Mn on the activity and stability of CoPt alloy toward MOR.

Chapter-5: Highly efficient $Pt_x(CoNiM)_{100-x}$ quaternary anode catalysts for methanol electrooxidation.

This chapter deals with the synthesis of multi-metallic alloy by simple microwave method. More specifically, we synthesized a quaternary alloy out of Pt, Co, Ni, and Fe/Ru metal. According to our findings, a quaternary metal alloy including containing 50% Pt and 50% of all other metals performs better.

Chapter-6: Final thoughts and future prospects.

This chapter summarizes the salient features of the work done in this thesis and provides a roadmap on the future scope of this work.

1.9 References:

1. Wakihara M. Recent developments in lithium ion batteries. *Materials Science and Engineering: R: Reports*. 2001 Jun 1;33(4):109-34.
2. Van Vliet O, Brouwer AS, Kuramochi T, van Den Broek M, Faaij A. Energy use, cost and CO₂ emissions of electric cars. *Journal of power sources*. 2011 Feb 15;196(4):2298-310.
3. Dunn S. Hydrogen futures: toward a sustainable energy system. *International journal of hydrogen energy*. 2002 Mar 1;27(3):235-64.
4. Sabo S. *Towards Sustainable Urban Mobility in Europe: Decoupling Transports externalities and Economic Development*.
5. Bent R, Orr L, Baker R, editors. *Energy: Science, policy, and the pursuit of sustainability*. Island Press; 2002.
6. Yuda A, Ashok A, Kumar A. A comprehensive and critical review on recent progress in anode catalyst for methanol oxidation reaction. *Catalysis Reviews*. 2022 Jan 2;64(1):126-228.
7. Liu Y, Zhu Y, Cui Y. Challenges and opportunities towards fast-charging battery materials. *Nature Energy*. 2019 Jul;4(7):540-50.
8. Socolow R, Hotinski R, Greenblatt JB, Pacala S. Solving the climate problem: technologies available to curb CO₂ emissions. *Environment: Science and Policy for Sustainable Development*. 2004 Dec 1;46(10):8-19.
9. Sheng T, Lin X, Chen ZY, Hu P, Sun SG, Chu YQ, Ma CA, Lin WF. Methanol electro-oxidation on platinum modified tungsten carbides in direct methanol fuel cells: a DFT study. *Physical Chemistry Chemical Physics*. 2015;17(38):25235-43.
10. Sharma S, Pollet BG. Support materials for PEMFC and DMFC electrocatalysts—A review. *Journal of Power Sources*. 2012 Jun 15; 208:96-119.
11. Schultz T, Zhou S, Sundmacher K. Current status of and recent developments in the direct methanol fuel cell. *Chemical Engineering & Technology*. 2001 Dec;24(12):1223-33.
12. Icardi UA, Specchia S, Fontana GJ, Saracco G, Specchia V. Compact direct methanol fuel cells for portable application. *Journal of Power Sources*. 2008 Feb 1;176(2):460-7.
13. Ogden JM, Steinbugler MM, Kreutz TG. A comparison of hydrogen, methanol and gasoline as fuels for fuel cell vehicles: implications for vehicle design and infrastructure development. *Journal of power sources*. 1999 Jun 1;79(2):143-68.

14. Armaroli N, Balzani V. The hydrogen issues. *ChemSusChem*. 2011 Jan 17;4(1):21-36.
15. Carrette L, Friedrich KA, Stimming U. *Fuel Cells-Principles. Types, Fuels and Applications*.
16. Wang C, Bai S, Xiong Y. Recent advances in surface and interface engineering for electrocatalysis. *Chinese Journal of Catalysis*. 2015 Sep 1;36(9):1476-93.
17. Samimi F, Rahimpour MR. Direct methanol fuel cell. In *Methanol* 2018 Jan 1 (pp. 381-397). Elsevier.
18. Yang Z, Berber MR, Nakashima N. A polymer-coated carbon black-based fuel cell electrocatalyst with high CO-tolerance and durability in direct methanol oxidation. *Journal of Materials Chemistry A*. 2014;2(44):18875-80.
19. Lei W, Li M, He L, Meng X, Mu Z, Yu Y, Ross FM, Yang W. A general strategy for bimetallic Pt-based nano-branched structures as highly active and stable oxygen reduction and methanol oxidation bifunctional catalysts. *Nano Research*. 2020 Mar;13(3):638-45.
20. Jia J, Zhao L, Chang Y, Jia M, Wen Z. Understanding the growth of NiSe nanoparticles on reduced graphene oxide as efficient electrocatalysts for methanol oxidation reaction. *Ceramics International*. 2020 Jun 1;46(8):10023-8.
21. Xia Z, Zhang X, Sun H, Wang S, Sun G. Recent advances in multi-scale design and construction of materials for direct methanol fuel cells. *Nano Energy*. 2019 Nov 1; 65:104048.
22. Aricò AS, Baglio V, Antonucci V. Direct methanol fuel cells: history, status and perspectives. *Electrocatalysis of direct methanol fuel cells*. 2009 Sep 23:1-78.
23. Basak PR, Kausshik N, Biswas S. Methanol as energy carrier. *Search*. 2010; 13:2.
24. Olah GA. Beyond oil and gas: the methanol economy. *Angewandte Chemie International Edition*. 2005 Apr 29;44(18):2636-9.
25. Okonkwo PC, Belgacem IB, Emori W, Uzoma PC. Nafion degradation mechanisms in proton exchange membrane fuel cell (PEMFC) system: A review. *International journal of hydrogen energy*. 2021 Aug 10;46(55):27956-73.
26. Iwasita T. Methanol and CO electrooxidation. *Handbook of fuel cells—fundamentals, technology and applications*. 2003; 2:603-24.
27. LaConti AB, Hamdan M, McDonald RC. *Handbook of fuel cells—fundamentals, technology and applications*. Wiley, New York, NY. 2003; 3:647.
28. Verma LK. Studies on methanol fuel cell. *Journal of power sources*. 2000 Mar 1;86(1-2):464-8.

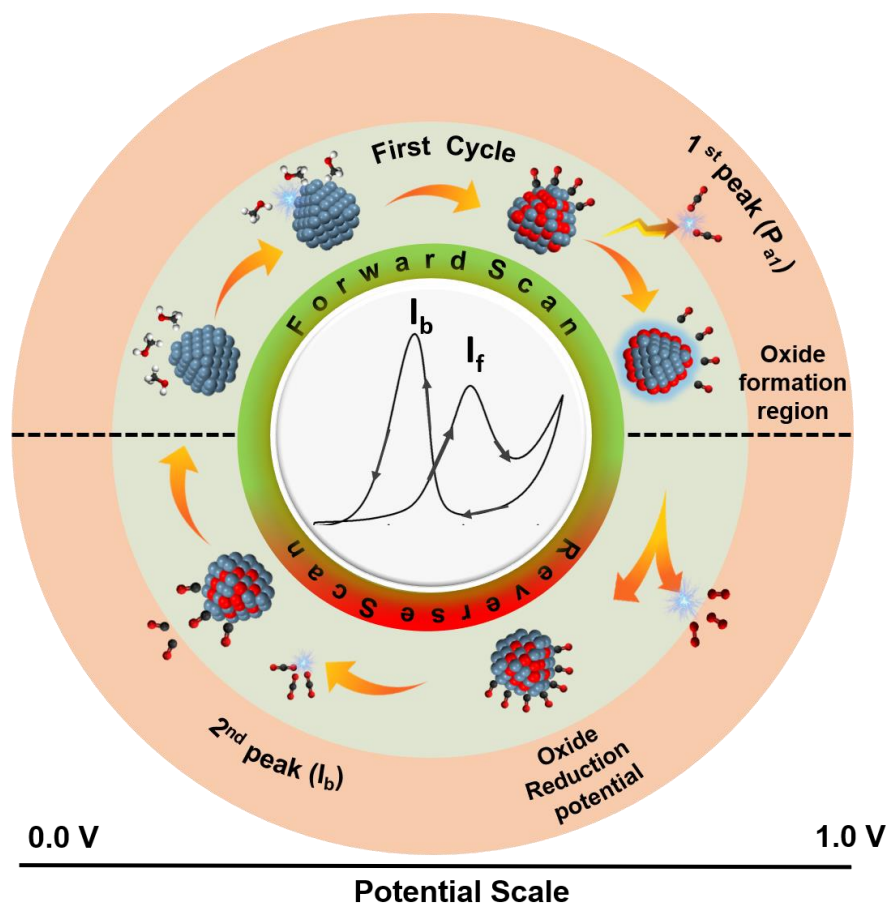
29. Liu JG, Zhao TS, Chen R, Wong CW. The effect of methanol concentration on the performance of a passive DMFC. *Electrochemistry Communications*. 2005 Mar 1;7(3):288-94.
30. Faghri A, Guo Z. An innovative passive DMFC technology. *Applied Thermal Engineering*. 2008 Sep 1;28(13):1614-22.
31. Zhao TS, Chen R, Yang WW, Xu C. Small direct methanol fuel cells with passive supply of reactants. *Journal of Power Sources*. 2009 Jun 15;191(2):185-202.
32. Park JY, Lee JH, Kang S, Sauk JH, Song I. Mass balance research for high electrochemical performance direct methanol fuel cells with reduced methanol crossover at various operating conditions. *Journal of Power Sources*. 2008 Mar 15;178(1):181-7.
33. Dillon R, Srinivasan S, Arico AS, Antonucci V. International activities in DMFC R&D: status of technologies and potential applications. *Journal of Power Sources*. 2004 Mar 10;127(1-2):112-26.
34. Dyer CK. Fuel cells for portable applications. *Journal of Power Sources*. 2002 Apr 1;106(1-2):31-4.
35. Gong L, Yang Z, Li K, Xing W, Liu C, Ge J. Recent development of methanol electrooxidation catalysts for direct methanol fuel cell. *Journal of energy chemistry*. 2018 Nov 1;27(6):1618-28.
36. H. Peng, Y. Xie, Y. Nie, *Journal of Central South University of Science and Technology*. 2007; 38(1): 98-101.
37. Wala M, Simka W. Effect of anode material on electrochemical oxidation of low molecular weight alcohols—A review. *Molecules*. 2021 Apr 9;26(8):2144.
38. Kunimatsu K. The infrared spectrum of linearly adsorbed CO species produced by chemisorption of methanol on a smooth platinum electrode at high anodic potentials. *Journal of Electroanalytical Chemistry and Interfacial Electrochemistry*. 1983 Mar 10;145(1):219-24.
39. Buschmann HW, Wilhelm S, Vielstich W. On the study of methanol oxidation by electrochemical sims. *Electrochimica Acta*. 1986 Aug 1;31(8):939-42.
40. Willsau J, Wolter O, Heitbaum J. On the nature of the adsorbate during methanol oxidation at platinum: A DEMS study. *Journal of electroanalytical chemistry and interfacial electrochemistry*. 1985 Apr 10;185(1):163-70.

41. Stamenkovic V, Mun BS, Mayrhofer KJ, Ross PN, Markovic NM, Rossmeisl J, Greeley J, Nørskov JK. Changing the activity of electrocatalysts for oxygen reduction by tuning the surface electronic structure. *Angewandte Chemie*. 2006 Apr 28;118(18):2963-7.
42. Mancharan R, Goodenough JB. Methanol oxidation in acid on ordered NiTi. *Journal of Materials Chemistry*. 1992 Jan 1;2(8):875-87.
43. Hofstead-Duffy AM, Chen DJ, Sun SG, Tong YJ. Origin of the current peak of negative scan in the cyclic voltammetry of methanol electro-oxidation on Pt-based electrocatalysts: a revisit to the current ratio criterion. *Journal of Materials Chemistry*. 2012;22(11):5205-8.
44. Zhao Y, Li X, Schechter JM, Yang Y. Revisiting the oxidation peak in the cathodic scan of the cyclic voltammogram of alcohol oxidation on noble metal electrodes. *RSC advances*. 2016;6(7):5384-90.
45. Chung DY, Lee KJ, Sung YE. Methanol electro-oxidation on the Pt surface: revisiting the cyclic voltammetry interpretation. *The Journal of Physical Chemistry C*. 2016 May 5;120(17):9028-35.
46. Li L, Xing Y. Methanol electro-oxidation on Pt-Ru alloy nanoparticles supported on carbon nanotubes. *Energies*. 2009 Sep 16;2(3):789-804.
47. Barakat NA, El-Newehy M, Al-Deyab SS, Kim HY. Cobalt/copper-decorated carbon nanofibers as novel non-precious electrocatalyst for methanol electrooxidation. *Nanoscale research letters*. 2014 Dec;9(1):1-0.
48. Li J, Zuo Y, Liu J, Wang X, Yu X, Du R, Zhang T, Infante-Carrió MF, Tang P, Arbiol J, Llorca J. Superior methanol electrooxidation performance of (110)-faceted nickel polyhedral nanocrystals. *Journal of Materials Chemistry A*. 2019;7(38):22036-43.
49. Yaqoob L, Noor T, Iqbal N, Nasir H, Mumtaz A. Electrocatalytic performance of NiNH₂BDC MOF based composites with rGO for methanol oxidation reaction. *Scientific reports*. 2021 Jun 28;11(1):1-8.
50. Huang X, Zhao Z, Cao L, Chen Y, Zhu E, Lin Z, Li M, Yan A, Zettl A, Wang YM, Duan X. High-performance transition metal-doped Pt₃Ni octahedra for oxygen reduction reaction. *Science*. 2015 Jun 12;348(6240):1230-4.
51. Li K, Li X, Huang H, Luo L, Li X, Yan X, Ma C, Si R, Yang J, Zeng J. One-nanometer-thick PtNiRh trimetallic nanowires with enhanced oxygen reduction electrocatalysis in acid media: Integrating multiple advantages into one catalyst. *Journal of the American Chemical Society*. 2018 Nov 2;140(47):16159-67.

52. Stamenkovic V, Mun BS, Mayrhofer KJ, Ross PN, Markovic NM, Rossmeisl J, Greeley J, Nørskov JK. Changing the activity of electrocatalysts for oxygen reduction by tuning the surface electronic structure. *Angewandte Chemie*. 2006 Apr 28;118(18):2963-7.

Chapter-2

Revisiting MOR mechanism



Many previously unknown facts regarding MOR mechanism have been disclosed in this chapter by re-investigating the cyclic voltammetric (CV) response of methanol oxidation in acidic medium utilizing Pt/C as an electro-catalyst. Systematic CV study indicated that the peak during the cathodic scan in CV for MOR is primarily due to CO electro-oxidation. According to the findings, the current response of this peak is not entirely responsible for adsorbed species. This demonstrates the need to reconsider the assumption of associating the ratio of anodic vs. cathodic peak currents to CO poisoning, which is commonly used to evaluate electrode performance in MOR.

2.1 Introduction:

In the introduction chapter we have discussed about the DMFC and the reaction occurring at DMFC, namely MOR and ORR. Out of these two reactions, MOR is considered to be a rate-determining step and the overall efficiency of DMFC depends on catalyst used for MOR. As a result, the quest for novel MOR electrocatalysts has become an extremely active research area.[1–5] Despite the vigorous efforts by many groups, the discovery of an electro-catalyst material with constant performance that is economically feasible is still at large, mainly because of our inadequate understanding of the precise MOR mechanism. As discussed in the introduction chapter, we would like to note that although significant progress has been achieved in defining the MOR mechanism and pinpointing the precise performance-determining steps [6–17], there are still certain ambiguities that we believe are preventing the systematic development of novel catalysts.

Attempts to understand the MOR mechanism began several decades ago. As mentioned in the previous Chapter, there are significant disputes on the intermediates formed during MOR. Using a combination of Infra-Red (IR) spectroscopy and electrochemistry methods, Kunimatsu et al. made the first notable contributions by establishing that CO is a significant intermediate species during MOR.[6–9] Later, the focus of MOR mechanism research switched to the identification of distinct intermediates using a variety of combined electro-analytical and spectroscopic approaches. These studies revealed that along with CO, formic acid, formaldehyde, and acetic acid are generated as intermediates during the early stages of MOR [13,17–20], though over time CO₂ becomes the only resulting product of MOR. Later, Buschmann et al.[10] and Willsau et al.[11] used in-situ differential electrochemical mass spectroscopy (DEMS) and in-situ secondary ion mass spectroscopy (SIMS) respectively to analyse the MOR intermediates based on the number of electrons involved in the electrochemical conversion of intermediates to CO₂. They concluded that CO is not an intermediate and that CHO is the real intermediate, contradicting the findings of Kunimatsu et al.

However, it has been proven that CHO is a very active intermediate in nature and, with the help of surface oxides on the electrode surface, it gets ultimately transformed to CO.[10, 11] Subsequent to these early studies Mancharan and Goodenough through detailed studies also identified CO as the intermediate[12], lending support to the CHO to CO hypothesis. Goodenough et al. not only concluded the intermediate to be CO, but also suggested a criterion

for assessing the electro-catalyst performance in MOR, by simply conducting a cyclic voltammetric experiment as detailed below.[12]

Figure 2.1 shows the typical CV for MOR that is generally observed when platinum on carbon is utilized as a catalyst. In anodic (I_f) and cathodic (I_b) scans, it mostly exhibits one peak each and as can be seen unlike the routine CV traces both these peaks display current in the positive direction. According to Goodenough and colleagues, some of the CO that is created during the anodic scan (I_f) oxidizes to CO_2 at a higher anodic potential. The leftover CO then gets adsorbed on the electrode surface, where it is converted to CO_2 upon scan reversal (I_b). Based on this mechanism, Goodenough and co-workers attributed the decline in electrocatalyst performance to "CO poisoning" and linked the peak current at I_b to the amount of adsorbed or unoxidized CO.[12] Furthermore, they proposed the peak current ratio (commonly referred to as I_f/I_b) as a marker for evaluating electro-catalyst performance in MOR. Their hypothesis was that the higher the I_f/I_b , the greater the CO tolerance and thus the better the electrode performance.

Despite the fact that the I_f/I_b ratio is the most widely accepted and used marker test to date, attempts to re-evaluate the MOR mechanism gained momentum, and new mechanisms and marker tests for MOR began to emerge.[13-16] Among these, the studies by Hofstead-Duffy et al., Zhao et al., and Chung et al. are the most relevant.[14-16] For example, Hofstead-Duffy et al. used in-situ Surface Enhance Infrared Absorption Spectroscopy (SEIRAS) to evaluate the MOR mechanism on Pt/C and PtRu/C and proposed that the electrochemical process associated with I_f and I_b shared the same chemical origin[14], i.e. both peaks correspond to electro-oxidation of methanol and are not related to any oxygenated carbon (formate, CO, CO_2). Zhao et al. and Chung et al. supplemented this proposal with different experimental approaches. Zhao et al. began the CV measurements without methanol and then added methanol during the early stages of the cathodic scan, observing the peak I_b as soon as they added methanol.[15] As a result, they concluded that because the potential scan direction at the time of methanol addition is cathodic, the possibility of methanol electro-oxidation to CO is negligible, and thus the species contributing to the I_b is not CO. They also claimed that I_b is linked to methanol oxidation rather than any oxygenated carbon species. At the same time, Chung et al, using combined CV and electrochemical impedance spectroscopy (EIS), proposed a similar process occurring at I_b , i.e. methanol electro-oxidation only.[16] These arguments, however, have a flaw. Hofstead-Duffy et al., for example, support their claims by correlating IR intensity changes for methanol within the potential region of I_f , I_b peaks in MOR CV.[14] However,

their findings show that the observed current for both CV peaks is comparable, whereas the corresponding IR intensities of the species claimed to be responsible for these two peaks are vastly different. The claims made by Zhao et al. and Chung et al. that the process occurring at I_b is the electro-oxidation of methanol and has nothing to do with any oxygenated carbon species have a similar flaw. It should be noted that, despite recording CV in the cathodic direction, they ignored the fact that the potential at which the scan began was sufficient to oxidize methanol.[15,16]

To summarize the preceding discussion, it is clear that there is a great deal of ambiguity in the CV analysis for MOR, the majority of which is associated with the process occurring at I_b . As a result, we believe that careful CV analysis and gaining deeper insights into the electrochemical phenomenon associated with I_b may aid in resolving the problem and providing a clear picture of MOR interpretation.

On this basis, we sought to comprehend

- (1) What are the intermediate species responsible for the origin of I_b ?**
- (2) What is the nature of those intermediate species?**
- (3) What factors influence I_b ?**

For these studies, we chose commercial Pt on carbon (20% Pt/C) as an electro-catalyst material because it is the most studied and standard material.

2.2 Experimental:

CV experiments were carried out in a three-electrode system with a CHI660B potentiostat. The working electrode was formed by depositing electro-catalyst material on a 3 mm diameter glassy carbon disc. Sonication was used to disperse 10 mg of 20% Pt/C (Johnson Matthey, Batch#108X029) in 1 mL of a 1:1 water:ethanol mixture containing 0.5% Nafion, which was then drop-casted on a glassy carbon electrode and allowed to dry at room temperature. As reference and counter electrodes, Ag/AgCl (3 M KCl) and Pt mesh were used. Unless otherwise specified, an electrolytic medium of 0.5 M H_2SO_4 was used, and MOR was performed with a concentration of 1 M methanol. The inert atmosphere was maintained by bubbling nitrogen gas during the electrochemical measurements. For MOR, the electrode was stabilized by recording repetitive CVs (usually 20 cycles) until a stable voltammogram was obtained, and then the data was collected.

CO stripping experiments were carried out in a CO-saturated 0.5 M H₂SO₄ solution. For 15 minutes, CO gas (99% purity) was bubbled, and the electrode potential was held at -0.2 V for 5 minutes. The stripping was carried out in a nitrogen-saturated 0.5 M H₂SO₄ solution.

2.3 Result and Discussion:

Figure 2.1 depicts the CV obtained using 20% Pt/C in 0.5 M H₂SO₄ and 1 M methanol, which is consistent with the typical MOR CVs reported in the literature.[17]

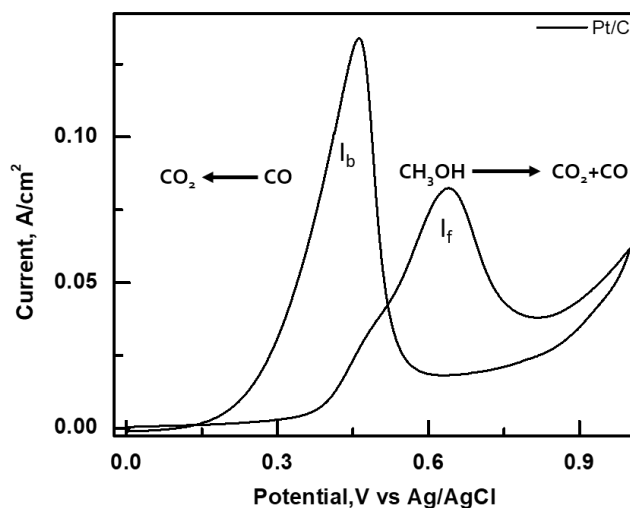


Figure 2.1: Cyclic voltammogram recorded using 20% Pt/C in 0.5 M H₂SO₄ and 1 M methanol solution (Scan rate: 50 mV/s).

We conducted a series of systematic CV experiments in order to gain a better understanding of this process. As most of the controversies are associated with the origin of I_b and nature of the species responsible for it, we decided to study this aspect in detail.

(a) Intermediate species responsible for the origin of I_b :

To begin, we measured the CV for MOR with Pt/C at different anodic potential limits, as shown in Figure 2.2(a). The black curve in Figure 2.2(a) corresponds to the CV profile where the potential is varied from 0 V to +1.0 V to 0 V. Similarly, the red curve represents the CV profile, in which the potential is varied from 0 V to +1.6 V to 0 V. In both instances, I_f was seen at the same potential of about 0.7 V. The inset of Figure 2.2(a) shows that as the anodic potential limit is increased, the position of the peak I_b shifts (from 0.4 V to 0.29 V) to the left, indicating that the separation between the I_f and I_b peaks changes (inset Figure 2.2(a)). Proceeding further, we precisely selected the potential value between I_f and I_b and used the same (0.5 V) as the starting potential to record the MOR CV in the cathodic scan direction (Figure 2.2(b)). The goal of this strategy is to completely avoid the electrochemical process associated with I_f by

beginning the scan at a lower potential than I_f 's onset potential, so that it is clear whether I_b is truly associated with I_f or whether the processes occurring at these two potentials are independent of each other.

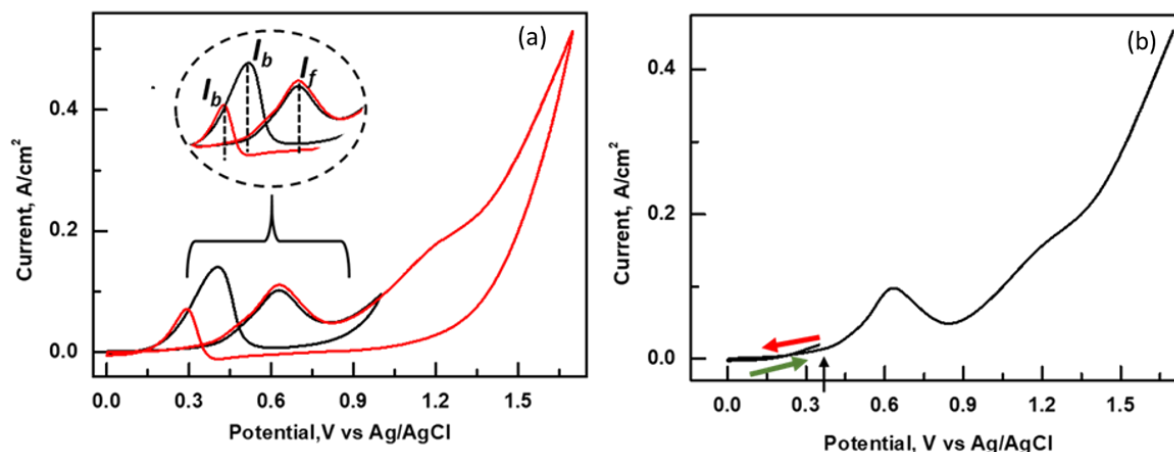


Figure 2.2: CV recorded using Pt/C in 0.5 M H_2SO_4 and 1 M methanol at Scan rate 50 mV/s. (a) Representative CVs recorded at end potential 1 V (Black) and 1.6 V (Red). The separation between the peaks increases as the anodic potential limit is changed (inset Figure 2.2 (a)) (b) CV started in the negative scan direction with start potential 0.5 V.

Figure 2.2(b) clearly shows that when the CV is recorded in the cathodic direction by starting the scan at 0.5 V, I_b does not appear. If I_b is indeed associated with methanol oxidation, as suggested by Zhao et al. and others[14-16], it should have appeared in this experiment as long as methanol was present in solution regardless of starting potential. Thus, based on the appearance of the peak at the potential corresponding to I_b when we started the scan at 0.5 V and went in the cathodic direction, we believe that the appearance of I_b [15,16] is definitely due to species formed at higher than 0.5 V irrespective of the scan direction. This clearly demonstrates that I_f and I_b are related, and I_b appears only after methanol oxidation occurs leading to the formation of oxidised species. We recorded different sets of CVs for MOR in the cathodic direction by varying the starting potential in a systematic way to support our hypothesis that the appearance of I_b is due to the over-potential at which the scan was started. We actually started our experiments well below the onset potential of I_f and gradually increased the starting potential to just above it (Figure 2.3). Figure 2.3 clearly shows that I_b is insignificant when the start potential is less than the onset potential of I_f . I_b began to appear as the starting potential approached the value of I_f , and when we began the scan at a potential greater than I_f , the intensity (current value) of I_b gradually increased.

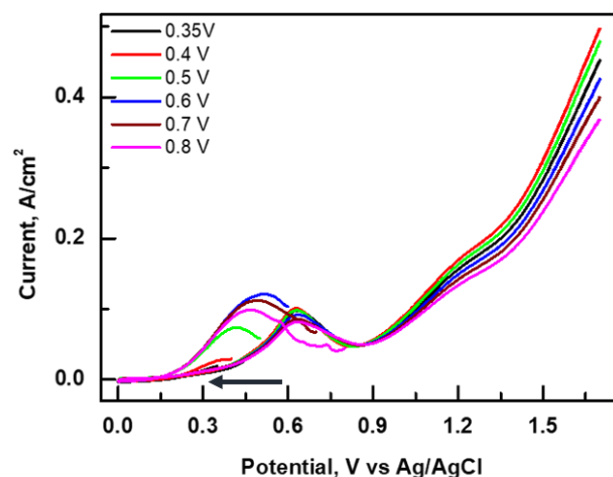


Figure 2.3: CV recorded using Pt/C in H₂SO₄ and methanol with scan rate 50 mV/s at different cathodic start potential (a legend in Figure corresponds to start potential).

Thus, our experiments clearly demonstrated that I_b is not connected with methanol oxidation, but rather to the new species, formed when the starting potential is close to or greater than I_f . As previously stated, various intermediates of MOR have been identified using various in-situ techniques.[10,11,13] However, we believe that the majority of these species will be unstable or will eventually be converted to CO, or in a few cases, their overall observed concentration in the system will be very low.[10] When the claims of different intermediates being formed and their observed concentrations are compared to the charges associated with I_b , it is difficult to believe that only these intermediates can contribute to the total current observed for I_b . Furthermore, the dependence of I_b on I_f suggests that I_b is due to electro-oxidation of CO, though we cannot completely rule out the contribution of other intermediates to I_b .

(b) Nature of intermediate species:

By considering all of the fact that pointed out CO as the most likely electro-active intermediate during MOR, we performed the following experiment to unambiguously confirm that the species formed by methanol oxidation at potentials close to or higher than I_f is CO. For this, we first performed a linear sweep voltammetry (LSV) (0 V to 1 V) experiment in methanol (experimental conditions: 20% Pt/C in 0.5 M H₂SO₄ and 1 M methanol), then transferred the same electrode into an electrochemical cell containing 0.5 M H₂SO₄ and measured the CV (Figure 2.4). As shown in Figure 2.4(b), the first cycle has an anodic peak at 0.56 V that is absent in subsequent cycles. This is typical of electrochemical CO stripping processes.[18-20] Interestingly, the position and characteristics of the peak around 0.5 V match with peak at I_b and CO stripping experiment, implying that the peak is due to CO. Thus, this experiment and

the above-mentioned arguments[10-12] confirm CO as an intermediate of MOR when the potential is at or above the potential of I_f and clearly shows that I_b is due to the oxidation of CO.

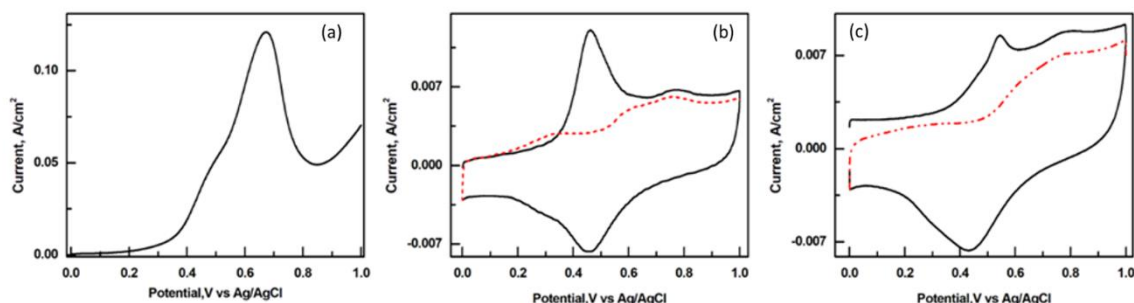


Figure 2.4: (a) LSV recorded using Pt/C in H_2SO_4 and methanol at 50 mV/s (b) CV recorded in 0.5 M H_2SO_4 at 50 mV/s after recording the LSV in 0.5 M H_2SO_4 and 1 M methanol (c) CO stripping experiment carried out in 0.5 M H_2SO_4 solution at 50 mV/s.

After confirming that CO is one of the species responsible for the I_b peak, we proceeded to assess its role as a catalyst poison, as suggested by Goodenough and colleagues. Because CO poisoning has been linked to its adsorption on the catalyst, its behaviour should align with other surface-adsorbed species in CV.[21]

To test this, we recorded the CVs for MOR at various scan rates. We first examined the variation of peak current for I_b with respect to scan rate. Figure 2.5(a) shows that the current value associated with I_b varies linearly with respect to the square root of the scan rate. Linear fitting of I_b current plotted against scan rate, on the other hand, is poor (Figure 2.5(b)). This clearly indicates that the species responsible for this peak is diffusion controlled. It is well recognized that for the plot $\log(v)$ vs. $\log(I_b)$, slope of a diffusion-controlled process is 0.5.[22,23] So, the electrochemical nature of the species responsible for I_b was confirmed further by plotting the $\log(v)$ vs. $\log(I_b)$ (Figure 2.5(c)), with slopes of 0.45 for I_b which is close to the expected values for diffusion-controlled processes. As a result of this analysis, it is clear that the electro-oxidation of CO at I_b is diffusion controlled. This confirms that some of the CO that is contributing to I_b reaches the electrode surface from the solution. This raises a question is this CO really poisoning the surface?

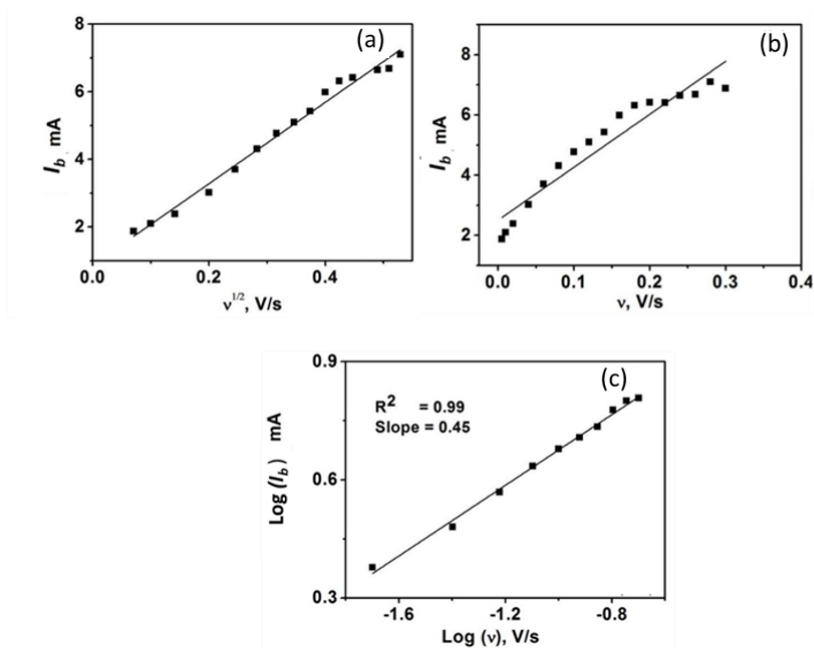


Figure 2.5: (a) Variation of peak current for I_b with respect to square root of scan rate (b) variation of peak current for I_b with respect to the scan rate and please note that in this case the fit is very poor (c) Linear relationship between logarithm of I_b peak current and logarithm of scan rate.

(c) Factor influencing I_b :

During MOR, Pt oxides are known to get formed on the electrode surface. We conducted the following experiment to investigate the role and dependence of Pt-oxide on the origin of the I_b peak. We have recorded MOR CV at higher scan rate with different potential window. The MOR CVs recorded at different anodic potential limits and at a higher scan rate (300 mV/s) (Figure 2.6) clearly showed the presence of a peak corresponding to the reduction of the surface oxide layer on the catalyst, which occurs at a positive potential compared to the I_b potential where CO oxidation occurs (Figure 2.6, denoted by arrows). This undoubtedly confirms that the electrochemical reduction of surface oxide layer on the catalyst occurs first, followed by the CO oxidation process at I_b .

Secondly, we recorded the CV with Pt/C in the presence and absence of methanol at different anodic potential limits. In the absence of methanol, CVs exhibited a negative shift in peak potential as well as an increase in current for the oxide reduction peak. This is due to an increase in the extent of oxide formation, which necessitates a higher potential for its electrochemical reduction.

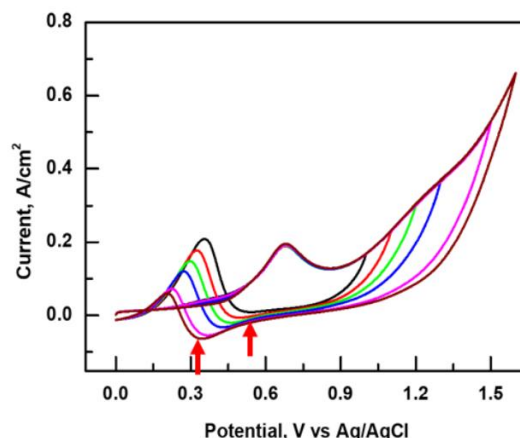


Figure 2.6: CVs recorded for Pt/C in 0.5 M H₂SO₄ and 1 M methanol at different anodic potential limits with 300 mV/s scan rate. Onset potentials for oxide reduction peak and I_b peak are denoted by arrows.

The potential necessary for the formation of an oxide monolayer was determined using the charge variation associated with the oxide reduction peak with respect to the anodic potential limit which is found to be 1.4 V. The peak I_b was evidently visible regardless of the level of oxide coverage on the electrode surface (even beyond the 1.4 V anodic potential limit). This is only feasible if all of the CO in the system is not entirely adsorbed, which supports our observation of CO's diffusion control nature at I_b.

Figure 2.7 (a, c) depicts the variation of I_f and I_b values with increasing anodic limit. Based on this graph, we can conclude that I_f nearly remains constant as the anodic limit increases, whereas I_b declines. The shift of the oxide reduction peak with increasing anodic limit is illustrated in Figure 2.7(b). With rising anodic limit, the oxide reduction peak exhibits the same behaviour as I_b, demonstrating the dependence or correlation of these peaks. Figure 2.7 (d) depicts the equivalent percent change in I_f/I_b ratio with anodic limit calculated from MOR CVs. It is obvious that there is a noticeable change in the I_f/I_b ratio from (about 70-100%) as the anodic limit is increased. So, all of the findings imply that comparing I_f/I_b ratio directly to CO poisoning could lead to erroneous interpretation since its value changes with anodic limit and I_b is not entirely due to adsorbed CO. There is also some contribution from the solution phase CO.

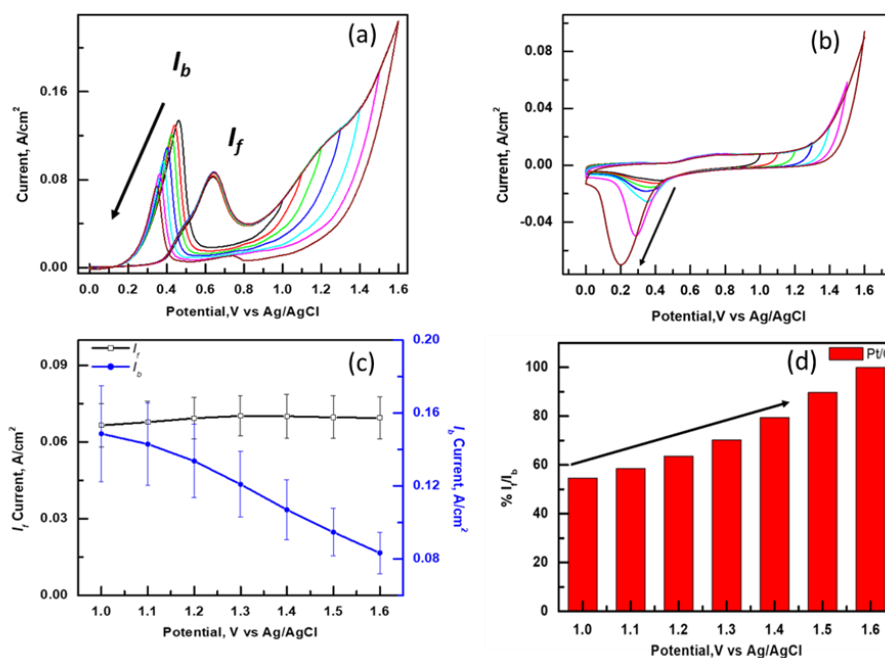


Figure 2.7: CVs recorded for Pt/C at different anodic potential limits with 50 mV/s scan rate (a) in 0.5 M H₂SO₄ and 1 M methanol (b) in 0.5M H₂SO₄ (c)Variation of I_f and I_b with increasing anodic limit (d) percent change in I_f/I_b ratio with anodic limit calculated from MOR CVs.

Based on all of the preceding systematic studies, we conclude that the following is the most plausible MOR mechanism.

As we begin the CV at 0 V, methanol oxidizes to CO at I_f during the first anodic scan, a portion of which is oxidized to CO₂ at higher potential the majority of the remaining un-oxidised CO remains in solution, with only a small portion adsorbed on the electrode surface. On scan reversal, this adsorbed CO, along with the CO in the solution, oxidizes at I_b (cathodic scan). However, at higher scan rates, the slower kinetics of catalyst surface oxide reduction impedes the extent of CO oxidation at I_b and thus limits complete CO oxidation.

2.4 Conclusion:

Utilizing systematic and detailed CV investigations, the precise mechanism of electrochemical methanol oxidation reaction in acidic media using Pt/C were re-investigated in this chapter. By selecting an acceptable starting potential and scan direction, the origins of the reverse peak in the cathodic direction (denoted as I_b in this report) were discovered, which conclusively ascribed it to be related to CO oxidation. Furthermore, it was demonstrated that the CO generated during the methanol oxidation process exhibited diffusion-controlled behaviour, implying that not all CO generated during the anodic scan is adsorbed on the catalyst surface.

Changes in the I_f/I_b ratio with anodic limits also indicate that the I_f/I_b concept is not suited for evaluating electro-catalyst performance in MOR, but it can be utilized to determine the Faradic efficiency of the MOR process.

2.5 References:

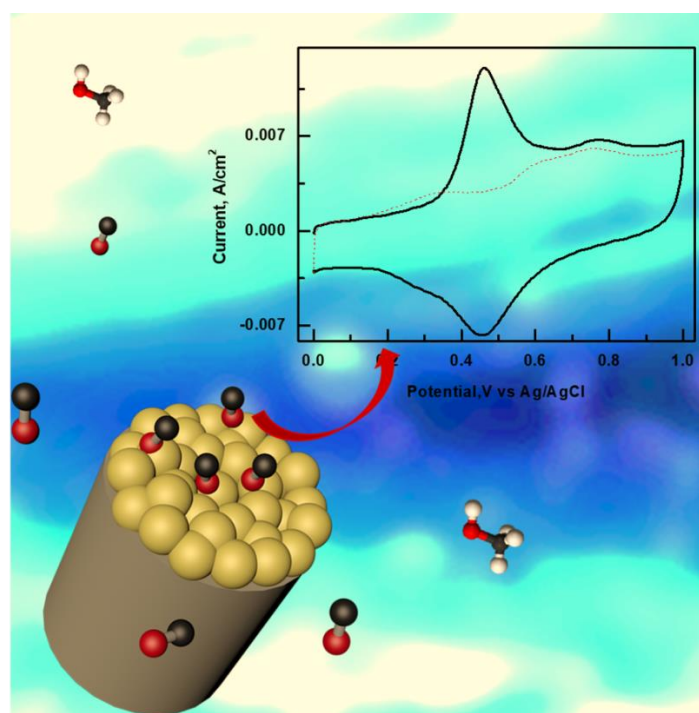
1. Mansor M, Timmiati SN, Lim KL, Wong WY, Kamarudin SK, Kamarudin NH. Recent progress of anode catalysts and their support materials for methanol electrooxidation reaction. *International Journal of Hydrogen Energy*. 2019 Jun 7;44(29):14744-69.
2. Kin Y, Saito K, Oda H, Ando T, Nakagawa K. Development of Direct Methanol Fuel Cell Catalyst Using Marimo Nano Carbon. *Catalysis Letters*. 2019 Jan;149(1):1-6.
3. Sridhar P, Bhat SD, Sahu AK. Newer polymer electrolytes and electrocatalysts for direct alcohol fuel cells. In *Electrochemistry 2017* Mar 3 (pp. 102-193).
4. Kakati N, Maiti J, Lee SH, Jee SH, Viswanathan B, Yoon YS. Anode catalysts for direct methanol fuel cells in acidic media: do we have any alternative for Pt or Pt–Ru?. *Chemical reviews*. 2014 Dec 24;114(24):12397-429.
5. Sankar S, Anilkumar GM, Tamaki T, Yamaguchi T. Cobalt-modified palladium bimetallic catalyst: a multifunctional electrocatalyst with enhanced efficiency and stability toward the oxidation of ethanol and formate in alkaline medium. *ACS Applied Energy Materials*. 2018 Aug 1;1(8):4140-9.
6. Beden B, Lamy C, Bewick A, Kunimatsu K. Electrosorption of methanol on a platinum electrode. IR spectroscopic evidence for adsorbed CO species. *Journal of Electroanalytical Chemistry and Interfacial Electrochemistry*. 1981 Apr 10;121:343-7.
7. Kunimatsu K. Potential dependence of infrared reflection absorption spectrum of the adsorbed carbon monoxide produced by chemisorption of methanol on a smooth platinum: A new in-situ IR spectroscopic method for the determination of the spectrum at a fixed potential. *Journal of Electroanalytical Chemistry and Interfacial Electrochemistry*. 1982 Nov 9;140(1):205-10.
8. Kunimatsu K. The infrared spectrum of linearly adsorbed CO species produced by chemisorption of methanol on a smooth platinum electrode at high anodic potentials. *Journal of Electroanalytical Chemistry and Interfacial Electrochemistry*. 1983 Mar 10;145(1):219-24.
9. Kunimatsu K. Study of adsorption at the electrode/solution interphase by in-situ infrared reflectance spectroscopy—adsorption of methanol on a platinum electrode—. In *Studies in Surface Science and Catalysis* 1983 Jan 1 (Vol. 14, pp. 215-220). Elsevier.
10. Buschmann HW, Wilhelm S, Vielstich W. On the study of methanol oxidation by electrochemical simulations. *Electrochimica Acta*. 1986 Aug 1;31(8):939-42.

11. Willsau J, Wolter O, Heitbaum J. On the nature of the adsorbate during methanol oxidation at platinum: A DEMS study. *Journal of electroanalytical chemistry and interfacial electrochemistry*. 1985 Apr 10;185(1):163-70.
12. Mancharan R, Goodenough JB. Methanol oxidation in acid on ordered NiTi. *Journal of Materials Chemistry*. 1992 Jan 1;2(8):875-87.
13. Chen YX, Miki A, Ye S, Sakai H, Osawa M. Formate, an active intermediate for direct oxidation of methanol on Pt electrode. *Journal of the American Chemical Society*. 2003 Apr 2;125(13):3680-1.
14. Hofstead-Duffy AM, Chen DJ, Sun SG, Tong YJ. Origin of the current peak of negative scan in the cyclic voltammetry of methanol electro-oxidation on Pt-based electrocatalysts: a revisit to the current ratio criterion. *Journal of Materials Chemistry*. 2012 Jan 26;22(11):5205-8.
15. Zhao Y, Li X, Schechter JM, Yang Y. Revisiting the oxidation peak in the cathodic scan of the cyclic voltammogram of alcohol oxidation on noble metal electrodes. *RSC advances*. 2016 Jan 7;6(7):5384-90.
16. Chung DY, Lee KJ, Sung YE. Methanol electro-oxidation on the Pt surface: revisiting the cyclic voltammetry interpretation. *The Journal of Physical Chemistry C*. 2016 May 5;120(17):9028-35.
17. Hogarth MP, Hards GA. Direct methanol fuel cells. Technological advances and further requirements. *Platinum Met. Rev.* 1996 Oct 1;40(4):150-9.
18. Ochal P, de la Fuente JL, Tsytkin M, Seland F, Sunde S, Muthuswamy N, Rønning M, Chen D, Garcia S, Alayoglu S, Eichhorn B. CO stripping as an electrochemical tool for characterization of Ru@ Pt core-shell catalysts. *Journal of electroanalytical chemistry*. 2011 Jun 1;655(2):140-6.
19. Pozio AD, De Francesco M, Cemmi A, Cardellini F, Giorgi L. Comparison of high surface Pt/C catalysts by cyclic voltammetry. *Journal of power sources*. 2002 Mar 5;105(1):13-9.
20. Jeon MK, Daimon H, Lee KR, Nakahara A, Woo SI. CO tolerant Pt/WC methanol electro-oxidation catalyst. *Electrochemistry Communications*. 2007 Nov 1;9(11):2692-5.
21. Bard Allen J, Faulkner Larry R. *Electrochemical methods: fundamentals and applications*.

22. Gowda JI, Nandibewoor ST. Electrochemical behavior of paclitaxel and its determination at glassy carbon electrode. *Asian Journal of Pharmaceutical Sciences*. 2014 Feb 1;9(1):42-9.
23. Gosser DK. *Cyclic voltammetry: simulation and analysis of reaction mechanisms*. New York: VCH; 1993

Chapter-3

Establishing a new efficiency descriptor for MOR and its validation with commercially available catalysts



The thorough CV analysis described in the previous chapter clearly shows that the peak during the cathodic scan in CV for MOR is not fully attributable to adsorbed CO, therefore we cannot directly relate it to poisoning. Furthermore, the existing criteria I_f/I_b have some lacunae, emphasising the necessity to develop new criterion. In this chapter, we attempt to define a new criterion based on the real amount of adsorbed species that causes catalyst poisoning. We evaluate this newly proposed criterion with commercial Pt/C (comm. Pt/C) and further validate it with other commercially available catalysts.

3.1 Introduction:

In earlier chapters, we focused on the mechanism of MOR and successfully explained the species responsible for the origin of I_b as well as the factors that govern it. According to the preceding chapter's findings, I_b is generated by the oxidation of CO; however, I_b cannot be completely attributed to CO adsorbed on the electrode surface as its current variation with square root of scan rate appears to be diffusion-controlled. The species that really gets adsorbed on the electrode surface and blocks it for the subsequent reaction is to be referred to as a catalyst poison. However, in the case of I_b , the current observed is due to oxidation of both solution and surface phase CO, therefore the amount of CO oxidised resulting in the current observed (I_b) cannot be linked to poisoning. Another important aspect of the previous chapter was its emphasis on the inadequacies in existing I_f/I_b criteria.

Year	Technique used	Assumption	Reference
1992	CV	<ul style="list-style-type: none"> ▪ I_f and I_b have different chemical origin. ▪ I_b represent the residual carbonaceous species on the electrode. ▪ I_f/I_b could be used to define a catalyst's tolerance to the accumulation of carbonaceous species. 	Ref-15
2012	In-situ surface enhance IR study	<ul style="list-style-type: none"> ▪ I_f and I_b share common chemical origin i.e. both are due to oxidation of freshly adsorbed methanol. ▪ As a result, I_f/I_b could not be used as a descriptor for poisoning. 	Ref-16
2016	Electrochemical impedance spectroscopy (EIS)	<ul style="list-style-type: none"> ▪ I_b is not affected by I_f i.e. I_f and I_b have different chemical origin. ▪ I_f/I_b is associated with oxophilicity rather than CO tolerance. 	Ref-13
2021	In-situ differential electrochemical mass spectroscopy (DEMS)	<ul style="list-style-type: none"> ▪ Both I_f and I_b peak current ascribed to the consumption of methanol at electrode surface. ▪ The peak area ratio should be the new criteria which links to the overlapping region between the potential of methanol oxidation and the potential of oxide reduction formed during forward scan ▪ I_f/I_b can be a new descriptor to describe the reducibility of oxidised Pt surface. 	Ref-14

Table 3.1: Controversy related to the I_f/I_b criteria.

Furthermore, we noticed that when we recorded CV at different potential windows, the value of the I_f/I_b ratio changed dramatically. Since MOR peaks for certain catalysts do not emerge within the typical range of 0-1 V in the literature, researchers resort to comparing catalyst's performance at different potential ranges.[1-6] Now, since the I_f/I_b ratio varies with the potential window, how can we compare catalysts performance at different potential windows? Another limitation of this criterion is that it cannot be applied to catalysts that lack a reversal peak in MOR CV.[7-12] Moreover to some reports, the I_f/I_b criteria are related to the degree of oxophilicity, which is used to define the reducibility of the oxidised Pt surface.[13-14] The controversy related to the I_f/I_b criteria is given in table 3.1.

Therefore, the above discussion, clearly indicates the need for new criteria that do not have the gaps indicated above.

This chapter focused on the species that poisoned the catalyst surface and how to determine it quantitatively. Our final aim of this study, is to fill gaps in existing criteria I_f/I_b by proposing new criteria based on an experiment performed on commercially available 20% Pt/C catalyst and attempting to validate this criterion using commercially available 20% RuPt/C, 20% FePt/C, and 20% Co₃Pt/C catalyst.

3.2 Experimental:

For experimental purpose, we have used commercially available 20% Pt/C, 20% RuPt/C, 20% FePt/C, and 20% Co₃Pt/C purchased from fuel cell store. Methanol and sulfuric acid were purchased from local agencies. All reagents were of analytical grade and used without further purification or processing.

3.3 Electrochemical measurements:

For the electrochemical measurements, a CH Instruments 660B electrochemical workstation with a three-electrode configuration at RT was used. A glassy carbon electrode drop casted with electrocatalyst ink was used as a working electrode. electrocatalyst ink was prepared by dispersing 2 mg of sample in 200 μ L of 1:1 ethanol:water mixture containing 5% nafion solution. Pt mesh and Ag/AgCl electrode were used as counter electrode and the reference electrode, respectively.

3.4 Result and Discussion:

As we established in the previous chapter when we record the CV in the range 0-1 V, the CO which is adsorbed on the electrode surface along with solution phase CO that gets oxidized contributes to I_b . Thus, surveying I_b we cannot determine the real amount of adsorbed CO that is responsible for the poisoning. In the preceding chapter, we ran a simple experiment to detect the intermediate. We simply recorded the LSV from 0 to 1 V in a 1 M methanol. Then instead of continuing the scan in the reverse direction in the same cell, we moved the electrode from a cell containing 1 M methanol and 0.5 M H_2SO_4 to a one that only has 0.5 M H_2SO_4 . We then recorded the CV again from 0-1 V. The goal of this experiment is to identify adsorbed species. This experiment made it very evident that the CO that is adsorbed on the electrode surface, gets stripped around 0.5 V when the CV is performed only in the presence of 0.5 M H_2SO_4 . As a result, we believe that this experiment provides us with the actual amount of CO that has been adsorbed on the electrode surface and we can relate it to poisoning. The schematic, figure 3.1 explains the aforementioned experiment in detail. It is evident from CV in 0.5 M H_2SO_4 that, any CO adsorbed on the electrode surface is entirely stripped away, hence there is no peak for CO from the second cycle.

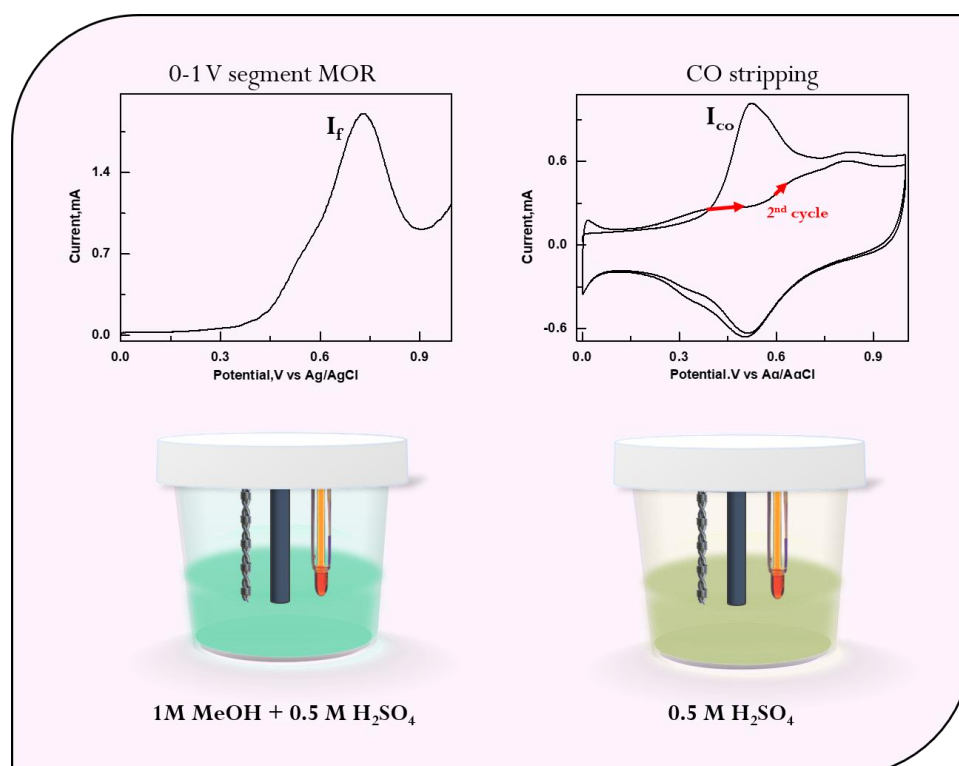


Figure 3.1: Schematic for in-situ CO stripping experiment.

According to our hypothesis, we can get the account of how much methanol gets oxidized from the I_f value by performing an LSV experiment in the range 0-1 V in 1 M methanol and 0.5 M H_2SO_4 . We can then shift the electrode by recording the CV in a solution containing 0.5 M H_2SO_4 and note the current generated during CO (I_{CO}) stripping. We can then look at I_f/I_{CO} and we surmised that this ration could provide a better account of CO poisoning. Based on our postulated mechanism and experimental findings, we feel that I_f/I_{CO} could be a new criterion for refereeing poisoning. As previously discussed, the existing criteria I_f/I_b changes with the anodic limit, therefore we cannot compare two catalysts with CV recorded at different anodic limits. Therefore, to see how the I_{CO} vary when the forward scan of the MOR is extended to different anodic limits, we performed the following experiment with comm. Pt/C

First, CV from 0-1 V was measured in 1 M methanol and 0.5 M H_2SO_4 solutions with different anodic limits using comm. Pt/C as a catalyst. The I_f/I_b variation with anodic limit was determined using this CV. The LSV is then measured at various anodic limits in 1 M methanol and 0.5 M H_2SO_4 . Following each LSV, we transplanted the electrode to another cell containing 0.5 M H_2SO_4 , and the LSV in the range 0 - 1 V was performed again to determine the quantity of CO adsorbed on the electrode in each scan.

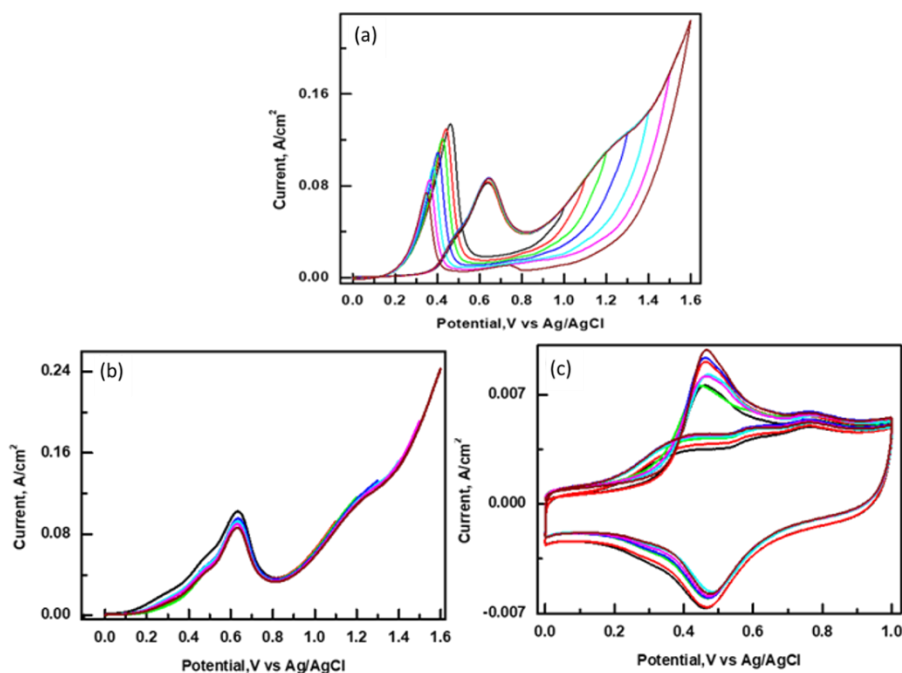


Figure 3.2: (a) CV recorded in 0.5 M H_2SO_4 and 1 M methanol solution at scan rate 50 mV/s (b) LSV recorded using 20% Pt/C in 0.5 M H_2SO_4 and 1 M methanol solution at different anodic limit. Scan rate: 50 mV/s (c) Cyclic voltammogram recorded in 0.5 M H_2SO_4 solution at different anodic limit Scan rate: 50 mV/s (CO stripping current).

As can be seen in Figure 3.2(c) there is not much variation in the I_{co} value even though the anodic limits were vastly different. Figure 3.3 (a,b) represent the percent variation of I_f/I_b , and I_f/I_{co} at different anodic limit. In fact, when we plot I_f/I_{co} ratio the variation in this value with respect to the anodic limit, the difference is insignificant when compared to the difference seen in case of I_f/I_b . (figure 3.3(c))

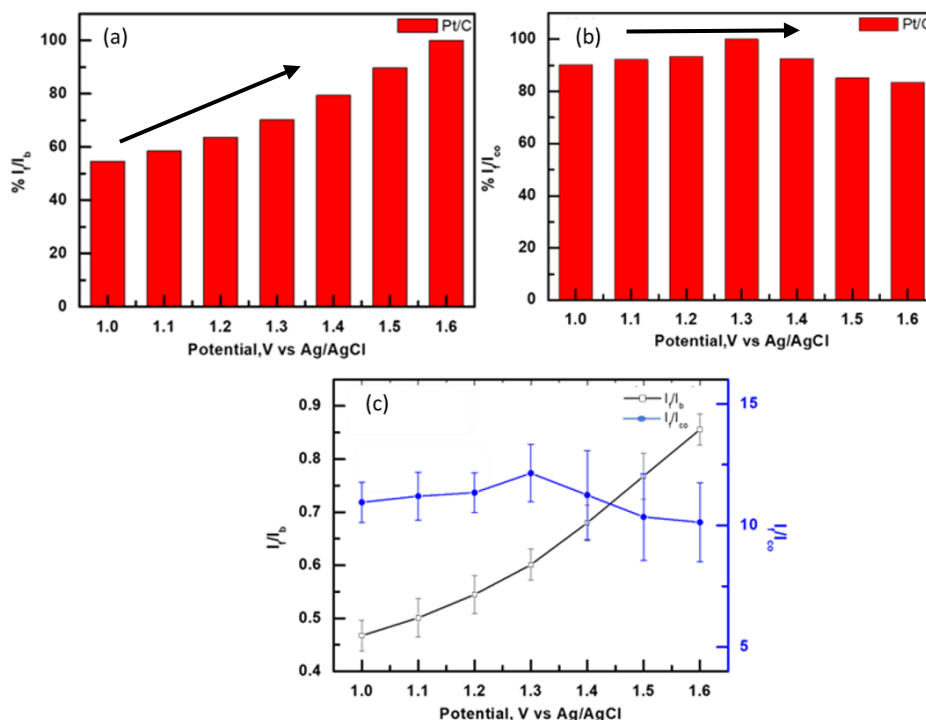


Figure 3.3: (a) Percent variation of I_f/I_b , (b) I_f/I_{co} at different anodic limit, (c) Comparison of I_f/I_b and I_f/I_{co} value with change in anodic limit.

As the new criteria did not alter much with the anodic limit for comm. Pt/C we intended to verify it with other commercially available catalysts. For this, we used commercially available RuPt/C, FePt/C, and Co_3Pt/C . As was done in the case of comm. Pt/C, we first carried out an LSV with the other commercial catalysts as well and extended the LSV to various anodic limits in 1M methanol and 0.5 M H_2SO_4 . Following the procedure done with comm. Pt/C after each LSV, these electrodes were then shifted to another cell containing 0.5 M H_2SO_4 and the CV in the range 0 – 1 V was again performed on them. Figure 3.4 (a,d,g) depict the CV for RuPt/C, FePt/C, and Co_3Pt/C in 1 M methanol and 0.5 M H_2SO_4 solutions with varying anodic limits. This CV was used to determine I_f/I_b variation with anodic limit. Figures 3.4 (b,e,h) show the LSV recorded in 1 M methanol and 0.5 M H_2SO_4 solutions. Figures 3.4 (c,f,i) depict the CVs performed on the electrodes which were shifted to cells containing 0.5 M H_2SO_4 solution only.

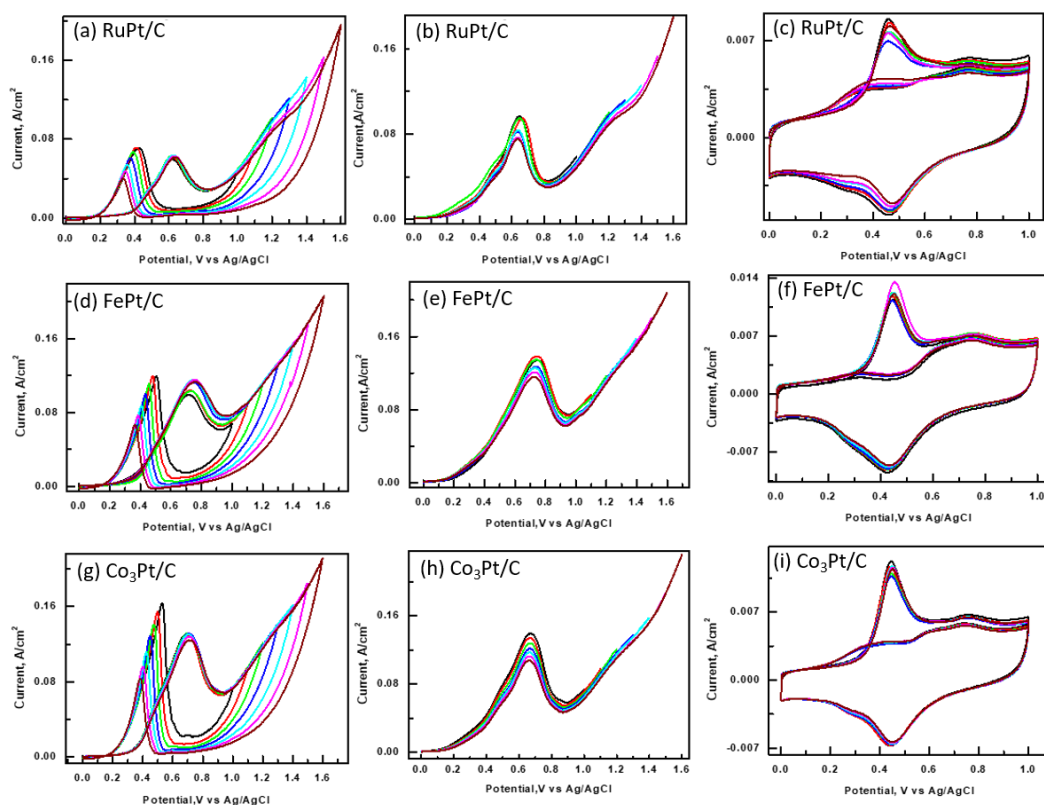


Figure 3.4: (a,d,g) CV recorded in 0.5 M H₂SO₄ and 1 M methanol solution , (b,e,h) LSV recorded in 0.5 M H₂SO₄ and 1 M methanol solution (c,f,i) Corresponding CO stripping current CV in 0.5 M H₂SO₄ solution at different anodic limit with scan rate of 50 mV/s for RuPt/C, FePt/C and Co₃Pt/C respectively.

The data obtained from above experiment was collectively plotted in figure 3.5. It can be clearly seen from this figure that, while the previous criterion I_f/I_b varies significantly with the change in anodic limit, the newly proposed criterion I_f/I_{CO} remains virtually constant. Thus, it is clear that our newly proposed criterion could be validated with other catalysts as well.

Catalyst	I_f/I_b	I_f/I_{CO}	CO stripping peak potential
Pt/C	0.47	10.9	0.46
RuPt/C	0.6	14.4	0.45
FePt/C	0.56	12.7	0.45
Co ₃ Pt/C	0.53	11.6	0.44

Table 3.2: Comparison of I_f/I_b and I_f/I_{CO} value for Pt/C, RuPt/C, FePt/C and Co₃Pt/C along with CO stripping peak potential.

Table 3.2 compares the average I_f/I_b and I_f/I_{co} values for all the catalyst. The table shows that the I_f/I_b and I_f/I_{co} values for all catalysts follow the same trend. This could indicate that with the help of the new criterion the catalyst evaluation can be performed in a more precise manner.

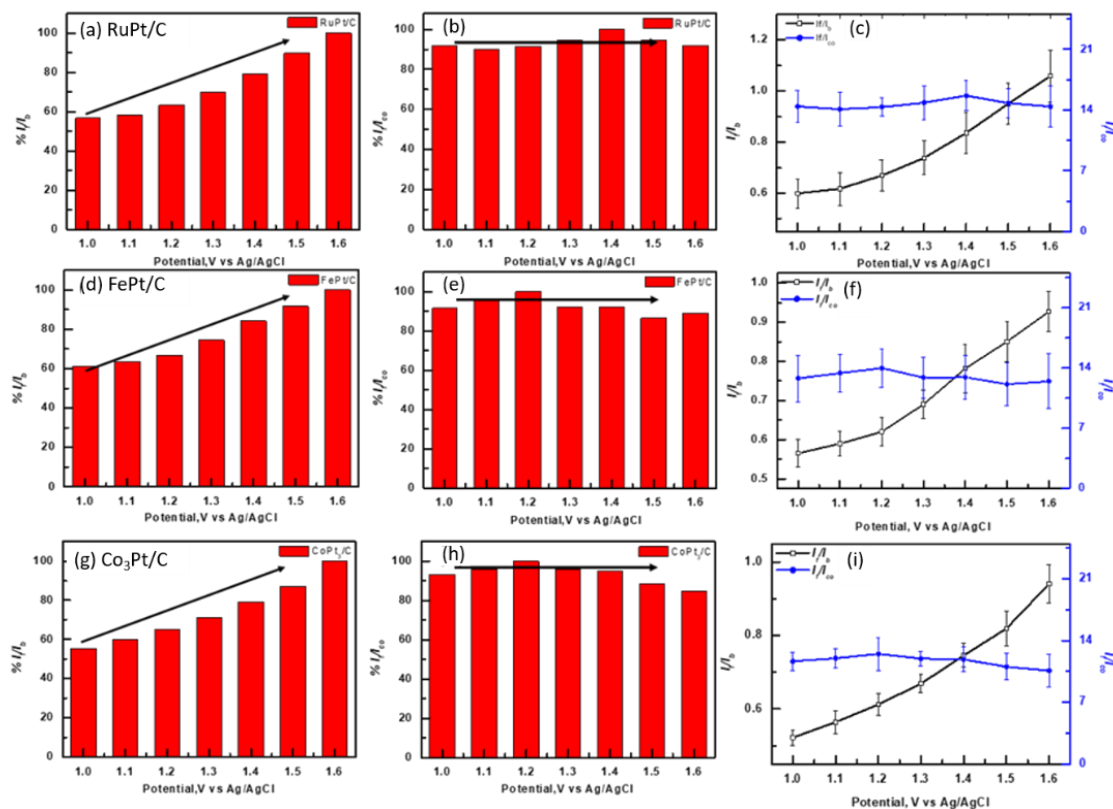


Figure 3.5: Percent variation of (a,d,g) I_f/I_b , (b,e,h) I_f/I_{co} at different anodic limit for RuPt/C, FePt/C and Co₃Pt/C respectively (c,f,i) Comparison of I_f/I_b and I_f/I_{co} value with change in anodic limit.

3.5 Conclusion:

In this chapter we established a new criterion to study the CO poisoning in MOR. We mainly focused on the lacunae faced by existing I_f/I_b criteria when the CV is carried out at different anodic limits. We then proposed a new criteria I_f/I_{co} which does not change with change in anodic limit. We validated this newly designed criterion with comm. Pt/C as well as with other commercially available catalysts. The findings presented in this chapter provide a new approach or guideline for studying materials for MOR. This motivates us to synthesise a new catalyst and put it to the test using new criteria.

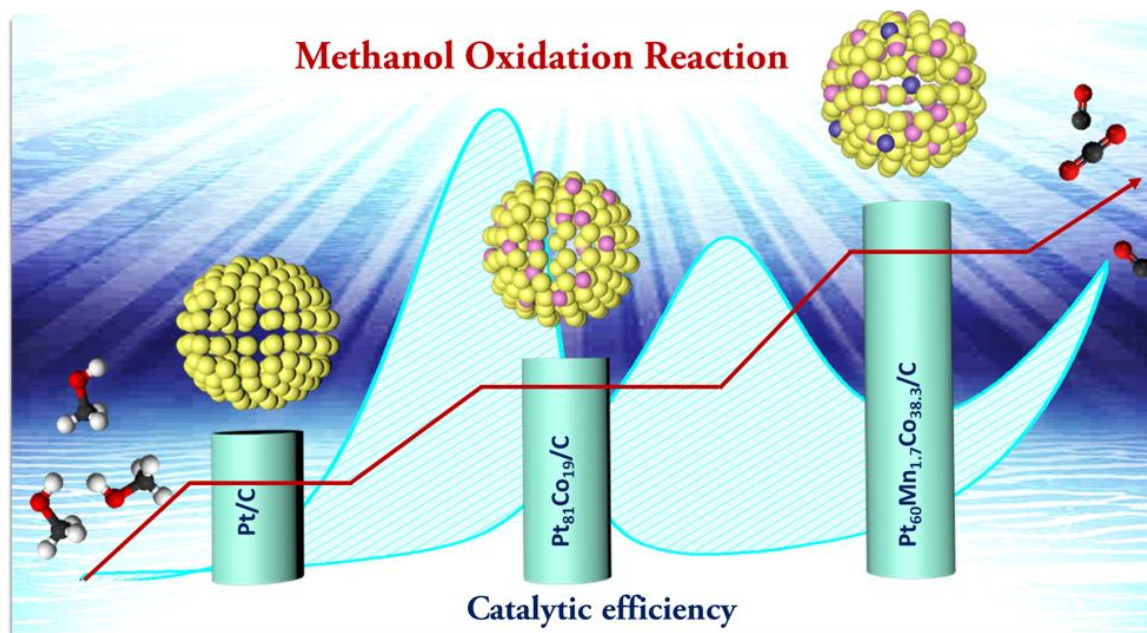
3.6 Reference:

1. Dang LQ, Nguyen MT, Truong NV, Le PH, Long N. Investigation of carbon supported Ru–Pt nanoparticles for high–performance electrocatalytic oxidation of methanol. *Int. J. Electrochem. Sci.* 2017 Nov 1;12:10187-98.
2. Khan IA, Sofian M, Badshah A, Khan MA, Imran M, Nadeem MA. Stable and efficient PtRu electrocatalysts supported on Zn-BTC MOF derived microporous carbon for formic acid fuel cells application. *Frontiers in chemistry.* 2020 May 13;8:367.
3. Mahapatra SS, Datta J. Characterization of Pt-Pd/C electrocatalyst for methanol oxidation in alkaline medium. *International Journal of Electrochemistry.* 2011 Jan 1;2011.
4. Justin P, Rao GR. Enhanced activity of methanol electro-oxidation on Pt–V₂O₅/C catalysts. *Catalysis Today.* 2009 Mar 15;141(1-2):138-43.
5. Khan IA, Sofian M, Badshah A, Khan MA, Imran M, Nadeem MA. Stable and efficient PtRu electrocatalysts supported on Zn-BTC MOF derived microporous carbon for formic acid fuel cells application. *Frontiers in chemistry.* 2020 May 13;8:367.
6. Mansor M, Timmiati SN, Wong WY, Mohd Zainoodin A, Lim KL, Kamarudin SK. NiPd Supported on Mesostructured Silica Nanoparticle as Efficient Anode Electrocatalyst for Methanol Electrooxidation in Alkaline Media. *Catalysts.* 2020 Oct 25;10(11):1235.
7. Barakat NA, El-Newehy M, Al-Deyab SS, Kim HY. Cobalt/copper-decorated carbon nanofibers as novel non-precious electrocatalyst for methanol electrooxidation. *Nanoscale research letters.* 2014 Dec;9(1):1-0.
8. Ghouri ZK, Barakat NA, Kim HY. Influence of copper content on the electrocatalytic activity toward methanol oxidation of Co_xCu_y alloy nanoparticles-decorated CNFs. *Scientific reports.* 2015 Nov 16;5(1):1-2.
9. Wu F, Zhang Z, Zhang F, Duan D, Li Y, Wei G, Liu S, Yuan Q, Wang E, Hao X. New insights into the electrocatalytic mechanism of methanol oxidation on amorphous Ni-B-Co nanoparticles in alkaline media. *Catalysts.* 2019 Sep 5;9(9):749.
10. Li L, Xing Y. Methanol electro-oxidation on Pt-Ru alloy nanoparticles supported on carbon nanotubes. *Energies.* 2009 Sep 16;2(3):789-804.
11. LubnaYaqoob TN, Iqbal N, Nasir H, Mumtaz A. Electrocatalytic performance of NiNH₂BDC MOF based composites with rGO for methanol oxidation reaction. *imprint.*;16:17.

12. Li J, Zuo Y, Liu J, Wang X, Yu X, Du R, Zhang T, Infante-Carrió MF, Tang P, Arbiol J, Llorca J. Superior methanol electrooxidation performance of (110)-faceted nickel polyhedral nanocrystals. *Journal of Materials Chemistry A*. 2019;7(38):22036-43.
13. Chung DY, Lee KJ, Sung YE. Methanol electro-oxidation on the Pt surface: revisiting the cyclic voltammetry interpretation. *The Journal of Physical Chemistry C*. 2016 May 5;120(17):9028-35.
14. Lai L, Yang G, Zhang Q, Yu H, Peng F. Essential analysis of cyclic voltammetry of methanol electrooxidation using the differential electrochemical mass spectrometry. *Journal of Power Sources*. 2021 Oct 15;509:230397.
15. Mancharan R, Goodenough JB. Methanol oxidation in acid on ordered NiTi. *Journal of Materials Chemistry*. 1992 Jan 1;2(8):875-87.
16. Hofstead-Duffy AM, Chen DJ, Sun SG, Tong YJ. Origin of the current peak of negative scan in the cyclic voltammetry of methanol electro-oxidation on Pt-based electrocatalysts: a revisit to the current ratio criterion. *Journal of Materials Chemistry*. 2012;22(11):5205-8.

Chapter-4

Improved performance of Co-Pt Alloy with a trace amount of Mn



The last chapter focuses on flaws in existing criteria (I_f/I_b) for judging CO poisoning and how to overcome them by presenting new criteria. We eventually arrived at the stage where we synthesized a new catalyst by conquering all of the obstacles in our path. This chapter focuses on the synthesis of novel catalysts using a simple hydrothermal approach. In this chapter, we thoroughly characterized the catalyst and used it to validate new criteria. Interestingly, we selected Mn in small amounts in our catalyst, although it shows variable oxidation state it has received less attention for electrochemical alcohol oxidation. We investigated the effect of trace amounts of Mn on PtCo alloy and the rationale for increased catalytic activity toward MOR.

4.1 Introduction:

In previous chapters, we carried out an in-depth investigation of CV analysis of MOR and presented a new mechanism for the same. We also highlighted several ambiguities not just concerning the MOR mechanism, but also about the criteria for judging poisoning. We were successful in developing a novel criterion to assess CO poisoning of the catalyst during MOR using a simple two stage CV analysis. Moving further, in this chapter we attempt to synthesise a novel catalyst that exhibits superior electrocatalytic activity than commercially available Pt/C (comm. Pt/C). We employed a simple hydrothermal approach to prepare this catalyst. As previously stated, Pt is the most widely utilised catalyst for MOR. However, major obstacles such as slow kinetics, high manufacturing costs (due mostly to the costly Pt-based catalyst), and CO poisoning of the Pt catalyst make commercialization of DMFCs difficult.[1-5] The search for an alternative Pt-based catalyst that avoids the aforementioned concerns is one of the most major scientific challenges. Pt alloys with other transition metals such as (Ru, Co, Ni, and Fe) have been shown to improve electrocatalyst activity and durability.[6] As a result, Pt-based alloys such as PtRu[7], PtNi[8], PtAu[9], PtPd[10], and PtCo[11] have attracted a great deal of attention in recent years. Among the different Pt-based alloys, PtCo bimetallic alloys have proven to be the most promising MOR catalyst.[12] Despite tremendous progress in the use of bimetallic alloys as MOR catalysts, a material with greater activity and endurance than commercial Pt-based catalysts remains elusive. According to few studies, introducing a trace of another metal into the bimetallic system can significantly boost the durability of the Pt-based bimetallic catalyst, making it more resistant to CO poisoning.[13-20] Furthermore, ternary Pt-based alloys are expected to have higher activity than single or bimetallic alloys due to changes in the electrical and structural properties of Pt.[21] As a result, trimetallic alloys of the type PtMCo (M can be any transition metal) are projected to improve both durability and electrocatalytic performance. Mn is a common and relatively inexpensive transition metal with different oxidation states that could be used as an electrocatalyst.[22-24] Surprisingly, while a few researches indicate that Mn improves the electrocatalytic activity of Pt[25-28], no investigations on Mn doping in PtCo catalysts and their efficiency for MOR exist. Despite the fact that Mn doping in PtCo alloy has been widely studied for (oxygen reduction reaction) ORR, the influence of trace quantities of Mn on the catalytic activity of PtCo alloy towards MOR has not been substantially investigated to our knowledge.[29-33]

As PtCo catalysts are known to perform better as MOR catalysts, we were inspired to conduct a thorough analysis of the feasibility of doping Mn into PtCo catalysts and analysing their

catalytic efficiency for MOR. Accordingly, in this chapter, we present the synthesis of PtCo alloys containing a trace of Mn ($\text{Pt}_{100-x}(\text{MnCo})_x$) ($16 < x < 41$) as well as the efficacy of trimetallic PtMnCo alloys as a MOR catalyst. The new PtMnCo catalysts' performance is compared to that of the bimetallic PtCo alloy and commercially available Pt/C (comm. Pt/C). The newly established criteria were also used to validate the synthesized PtMnCo catalyst.

4.2. Experimental:

Metal chloride salts such as platinum (II) chloride, manganese (II) chloride tetrahydrate, and cobalt (II) chloride hexahydrate were employed as metal precursors in the synthesis. All of the metal salts were purchased from Sigma Aldrich, while other chemicals such as methanol, ethanol, sodium bicarbonate, and NaOH were obtained from local agencies. Alfa Aesar supplied commercial Pt/C (Comm. Pt/C) with 20% Pt. All of the compounds employed were of analytical quality and did not require further purification.

(a) Synthesis of nanoparticles:

$\text{Pt}_{100-x}(\text{MnCo})_x$ ($16 < x < 41$) alloys were made by borohydride reduction followed by 3 hours of hydrothermal treatment at 150 °C.[34] The metal precursors were added to a Teflon container with a mixture of water and ethanol (20 mL water and 10 mL ethanol). For 10 minutes, the liquid was agitated to ensure that the metal precursor was completely dissolved. After the metal precursor was completely dissolved, a 10 mL solution of 5 M NaOH was gently added to the aforesaid mixture. When 5 M NaOH solution was added to the mixture, the colour changed from pale yellow to black, indicating the development of metal oxide/hydroxide. As a reducing agent, 0.01 g of sodium borohydride in 30 mL of water was added slowly, drop by drop, with a syringe to the above black-coloured liquid. For another 10 minutes, the mixture was vigorously stirred. The teflon bottle was then sealed firmly in a stainless steel autoclave. The autoclave was hydrothermally treated by placing it in a 150 °C oven for 3 hours. After 3 hours, the autoclave was allowed to cool to room temperature (RT), and the resulting mixture was treated with 1 M HCl solution until the pH became acidic. The resulting combination was magnetic, and it was separated using a magnet. The separated sample was rinsed with an excess of water and ethanol before drying at room temperature.

(b) Characterizations of $\text{Pt}_x(\text{MnCo})_{1-x}$ nanoparticles:

PtMnCo alloys were characterized using several techniques such as X-ray diffraction (XRD), high-resolution transmission electron microscopy (HR-TEM), and ICP-AES. The PXRD

analysis was performed with Cu K α (1.5418) as a radiation source to conclude the alloy formation and delineate other structural properties. The PXRD study was carried out on a Philips PAN analytical instruments X'pert Pro model PAN analytical diffractometer. The voltage and current for the XRD apparatus were kept at 40 kV and 30 mA, respectively. Ground powder was used to prepare the sample for XRD on a glass slide. The samples were scanned at a rate of 0.3° per minute in a 2 θ range from 10° to 80°. Using the full width half maxima (FWHM) and angular position of the Pt (111) peak, the average crystal size and lattice parameter were estimated. An inductively coupled Microwave Plasma Atomic Emission Spectrometer was used to determine the elemental composition (ICP-AES; Model: Agilent, 4200). For this measurement, the sample was produced by dissolving fixed mg of alloy in a small amount of aqua regia and diluting it to 100 mL. The sample's size, shape, and chemical composition were investigated using high resolution Transmission Electron Microscopy (HR-TEM, JEMF200, JEOL, operated at 300 kV). HR-TEM samples were made by drop casting an ultrasonically dispersed catalyst solution in ethanol onto a copper TEM grid (200 mesh), then evaporating the ethanol at room temperature.

(c) Electrochemical measurements:

Electrochemical analysis was carried out on a CH Instruments 660B electrochemical workstation with three electrodes. As counter and reference electrodes, Pt wire and Ag/AgCl electrodes were used. The electrochemical activity of the catalyst toward MOR was determined by dropping electrocatalyst material ink onto a glassy carbon electrode that served as a working electrode. For the creation of catalyst ink, the prepared (Pt_{100-x}(MnCo)_x) (16 < x < 41) alloy samples were first loaded on Vulcan XC-72 carbon at a loading of 20% wt. In the remainder of the work, these samples will be referred to as Pt_{100-x}(MnCo)_x/C (16 < x < 41). We used 20% loaded samples in all electrochemical measurements. In a typical loading process, catalyst (such as 4 mg (Pt_{100-x}(MnCo)_x) NPs (16 < x < 41)) and Vulcan XC-72 carbon (16 mg) were dispersed separately in 10 mL ethanol followed by ultrasonication for 30 minutes, following that, the sample dispersion was added to the carbon dispersion and agitated for about 15 hours. After stirring, it was centrifuged, washed with acetone, and dried at room temperature. TGA analysis was done on two samples to confirm catalyst loading on carbon support (Figure 4.1). Finally, electrocatalyst ink was made for the working electrode by dispersing 2 mg of Pt_{100-x}(MnCo)_x in 200 μ L of a 1:1 ethanol:water combination containing 5% Nafion solution. 4 μ L of this dispersion was cast on a glassy carbon electrode and dried at room temperature. A similar method was used to prepare the comm. Pt/C (20 wt% Pt) working electrode. To explore

the electrochemical behaviour of several catalysts, cyclic voltammetry (CV) measurements were performed. The electrochemical active surface area (ECSA) of a Pt-based alloy was calculated by measuring CV in $N_2(g)$ saturated aqueous 0.5 M H_2SO_4 at a scan rate of 50 mV/s in the potential region 1.4 to -0.23 V vs Ag/AgCl. The first potential area, from -0.23 to 0.1 V, represents the hydrogen adsorption/desorption region on the Pt surface. The electrochemical surface area (m^2/g) was determined by taking the monolayer charge on platinum ($210 \mu C/cm^2$), the platinum loading, and the integrated charge in the hydrogen adsorption and desorption region. Experiments were carried out in a $N_2(g)$ saturated 0.5 M H_2SO_4 and 1 M CH_3OH aqueous solution to determine the activity of the catalyst towards MOR, and CVs were recorded at a scan rate of 50 mV/s in a potential range of 0.0 to 1.0 V vs Ag/AgCl. Chronoamperometry curves were acquired for 8000 seconds to test the stability of electrodes at 0.65 V vs Ag/AgCl. CO stripping was performed in a CO-saturated 0.5 M H_2SO_4 solution. CO gas (99% purity) was bubbled for approximately 20 minutes to saturate the 0.5 M H_2SO_4 solution. Hold the electrode voltage at -0.2 V for 10 minutes to adsorb CO on the electrode surface. Stripping was performed at a rate of 50 mV/s.

4.3. Result and Discussion:

(a) Crystal structure and microstructural analysis:

Figure 4.2 shows the PXRD patterns of $(Pt_{100-x}(MnCo)_x)$ ($16 < x < 41$) alloys. It should be emphasised that the alloy compositions shown in Figure 4.2 were determined using ICP-AES analysis (Table 4.1).

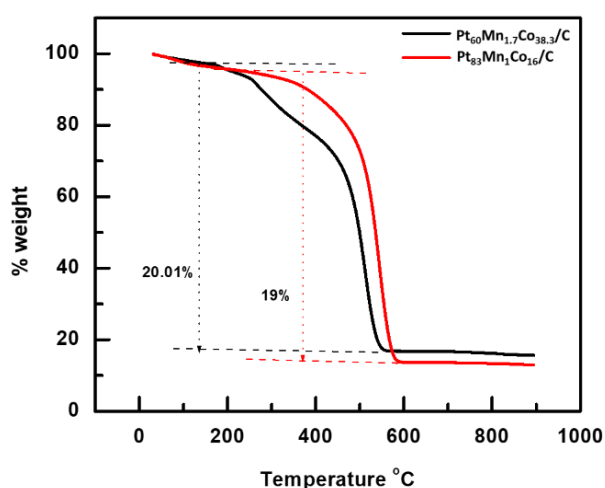


Figure 4.1: TGA analysis for $Pt_{60}Mn_{1.7}Co_{38.3}/C$ and $Pt_{83}Mn_1Co_{16}/C$ samples.

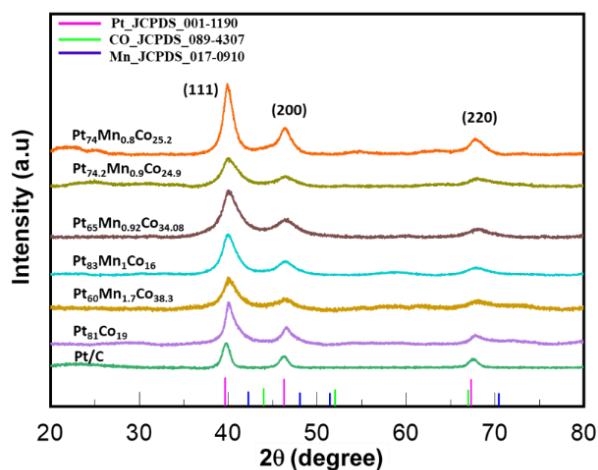


Figure 4.2: XRD patterns for $\text{Pt}_{100-x}(\text{MnCo})_x$ ($16 < x < 41$) alloys.

The diffraction peaks at 39.8° , 46.4° , and 67.8° for Pt/C in the PXRD patterns are attributed to the Pt (111), (200), and (220) facets, respectively. The position of all peaks in PtMnCo alloys was found to be somewhat displaced to higher 2θ values when compared to the normal diffraction peaks of Pt (JCPDS 001 1190). (Figure 4.2). The lattice parameters a for $\text{Pt}_{81}\text{Co}_{19}$, $\text{Pt}_{60}\text{Mn}_{1.7}\text{Co}_{38.3}$, $\text{Pt}_{83}\text{Mn}_1\text{Co}_{16}$, $\text{Pt}_{65}\text{Mn}_{0.92}\text{Co}_{34.08}$, $\text{Pt}_{74.2}\text{Mn}_{0.9}\text{Co}_{24.9}$, and $\text{Pt}_{74}\text{Mn}_{0.8}\text{Co}_{25.2}$ were determined to be 3.91, 3.88, 3.90, 3.89, 3.90, and 3.91, indicating a discernible drop in the lattice parameter with respect to the values for comm. Pt/C ($a = 3.93\text{\AA}$).

Sample	Manganese chloride tetrahydrate Mn(mmol)	Cobalt chloride hexahydrate Co(mmol)	Platinum Chloride Pt(mmol)	Total mmol	Composition from ICP
1	-	0.3	0.3	0.6	$\text{Pt}_{81}\text{Co}_{19}$
2	0.3	0.3	0.3	0.9	$\text{Pt}_{60}\text{Mn}_{1.7}\text{Co}_{38.3}$
3	0.6	0.3	0.3	1.2	$\text{Pt}_{83}\text{Mn}_1\text{Co}_{16}$
4	0.9	0.3	0.3	1.5	$\text{Pt}_{65}\text{Mn}_{0.92}\text{Co}_{34.08}$
5	1.2	0.3	0.3	1.8	$\text{Pt}_{74.2}\text{Mn}_{0.9}\text{Co}_{24.9}$
6	1.5	0.3	0.3	2.1	$\text{Pt}_{74}\text{Mn}_{0.8}\text{Co}_{25.2}$

Table 4.1: Details of stoichiometric amount of metal precursors used for the synthesis of Pt_{100-x}(MnCo)_x alloys NPs.

The average crystallite sizes were found to be in the range of 3.5 nm to 5.0 nm using the Scherrer formula and the complete width at half maximum of the (111) plane (Table 4.2).

Sample	Lattice constant (<i>a</i>) Å	Crystal size (nm)	% strain
Pt ₈₁ Co ₁₉	3.91	4.92 ± 0.50	-0.517
Pt ₆₀ Mn _{1.7} Co _{38.3}	3.88	3.73 ± 0.16	-1.218
Pt ₈₃ Mn ₁ Co ₁₆	3.90	4.3 ± 0.02	-0.679
Pt ₆₅ Mn _{0.92} Co _{34.08}	3.89	3.67 ± 0.24	-0.786
P _{74.2} Mn _{0.9} Co _{24.9}	3.90	4.07 ± 0.19	-0.549
Pt ₇₄ Mn _{0.8} Co _{25.2}	3.91	4.76 ± 0.90	-0.296

Table 4.2: The lattice constant, crystal size and % strain for Pt_{100-x}(MnCo)_x (16 < x < 41) alloys calculated from corresponding XRD patterns.

TEM images (Figure 4.3) indicate that all generated materials have roughly spherical morphology with individual particle sizes ranging from 5 to 8 nm, confirming that the synthesized materials are nanoparticles (NPs). The average TEM particle sizes for Pt₆₀Mn_{1.7}Co_{38.3}, Pt₈₃Mn₁Co₁₆, Pt₆₅Mn_{0.92}Co_{34.08}, P_{74.2}Mn_{0.9}Co_{24.9}, and Pt₇₄Mn_{0.8}Co_{25.2} NPs were 5.0 ± 1.1 nm, 8.2 ± 2.1 nm, 5.5 ± 1.3 nm, 6.7 ± 1.7 nm, and 7.3 ± 1.62 nm, respectively (Figure 4.3 (d-f,i,j)). In comparison, the average TEM particle size of the Pt₈₁Co₁₉ sample was 8.3 ± 2.57 nm. Please see Figure 4.4 the TEM and HAADF STEM images of Pt₈₁Co₁₉ sample.

To determine the distribution of Pt, Mn, and Co in Pt₆₀Mn_{1.7}Co_{38.3}, Pt₈₃Mn₁Co₁₆, Pt₆₅Mn_{0.92}Co_{34.08}, P_{74.2}Mn_{0.9}Co_{24.9}, and Pt₇₄Mn_{0.8}Co_{25.2} samples, we used elemental mapping (Figure 4.5) and EDS line scanning (Figure 4.6). These findings unequivocally confirm the simultaneous presence of Pt, Mn, and Co in all of the samples tested. It is worth noting that the poor Mn signal was presumably caused by the low amount of Mn present in the Pt_{100-x}(MnCo)_x (16 < x < 41) NPs.

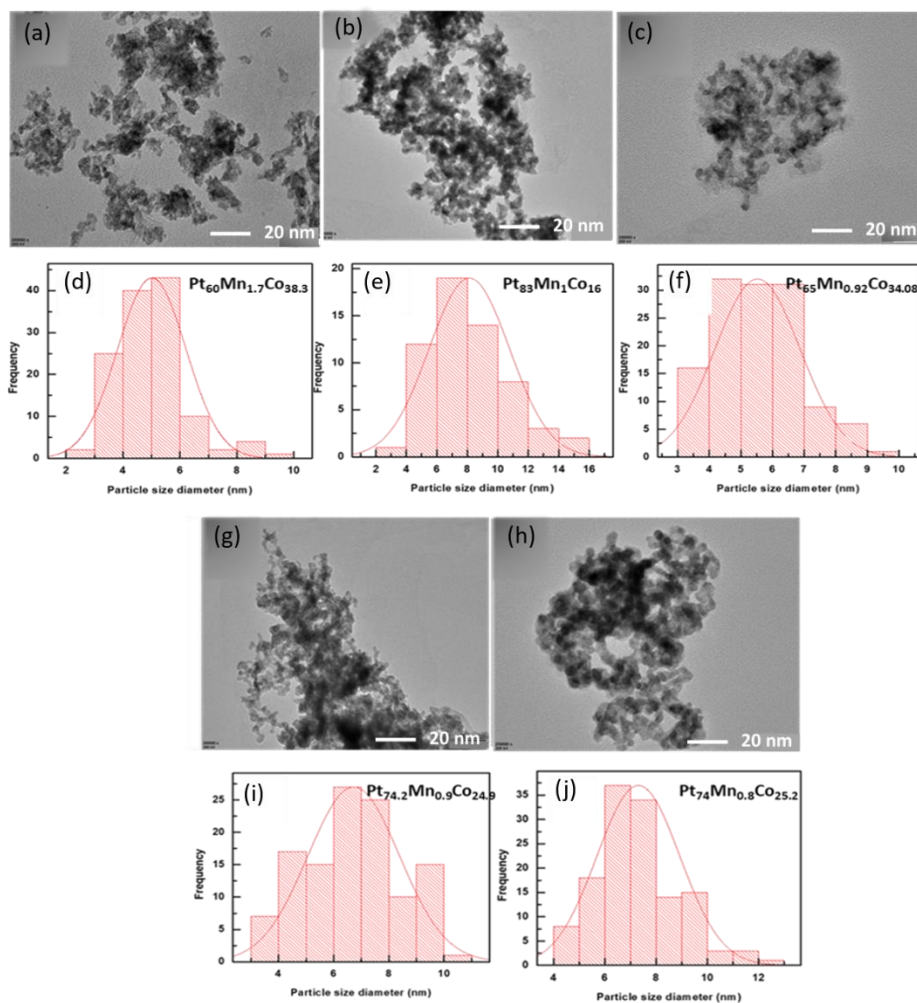


Figure 4.3: TEM micrographs (a-c and g-h) and corresponding particle size distribution plots (d-f and i-j) of $\text{Pt}_{100-x}(\text{MnCo})_x$ ($16 < x < 41$) alloys.

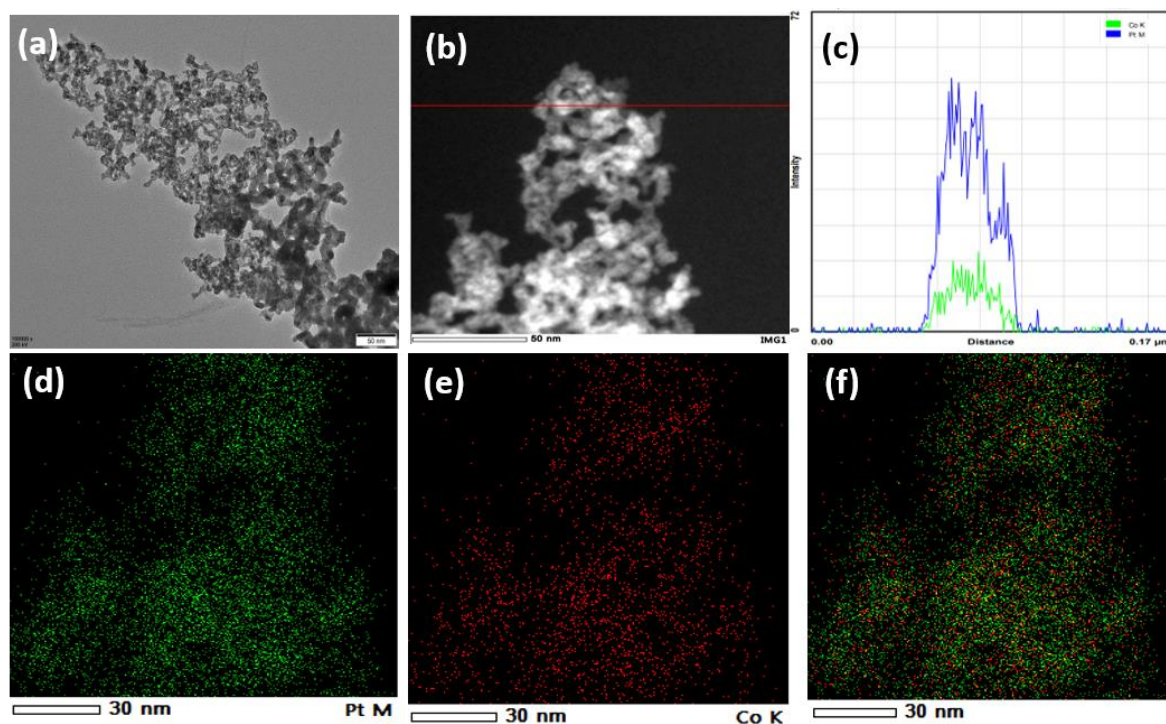


Figure 4.4: (a) TEM image, (b) HAADF-STEM image, (c) EDS line scan profile and elemental mapping for Pt₈₁Co₁₉ (d-f).

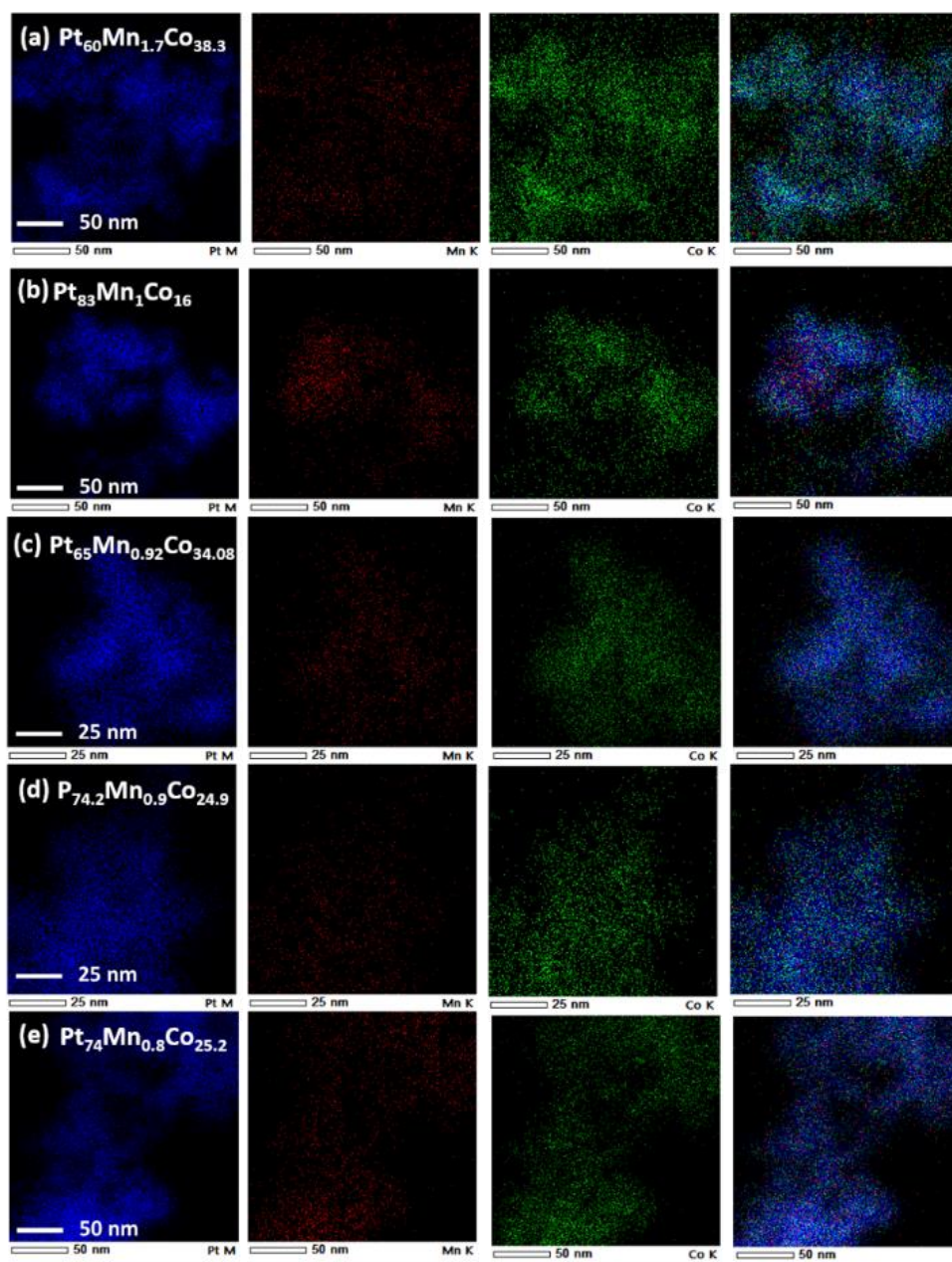


Figure 4.5: Elemental mapping for (a) $\text{Pt}_{60}\text{Mn}_{1.7}\text{Co}_{38.3}$, (b) $\text{Pt}_{83}\text{Mn}_1\text{Co}_{16}$, (c) $\text{Pt}_{65}\text{Mn}_{0.92}\text{Co}_{34.08}$, (d) $\text{Pt}_{74.2}\text{Mn}_{0.9}\text{Co}_{24.9}$, (e) $\text{Pt}_{74}\text{Mn}_{0.8}\text{Co}_{25.2}$ respectively.

XPS analysis was also performed on the $\text{Pt}_{100-x}(\text{MnCo})_x$ ($16 < x < 41$) alloys. Figures 4.7 and 4.8 offer in-depth details of XPS analysis. The Pt spectra following deconvolution in $\text{Pt}_{60}\text{Mn}_{1.7}\text{Co}_{38.3}$ catalyst shows four peaks at 71.20, 72.44, 74.48, and 75.46 eV, with the peaks at 71.20 and 74.48 eV corresponding to Pt^0 , and the peaks at 72.44 and 75.46 eV corresponding to Pt^{+2} .^[35] Metallic Pt^0 may be seen in the XPS spectra of the $\text{Pt}_{60}\text{Mn}_{1.7}\text{Co}_{38.3}$ catalyst (Figure 4.7(a)).

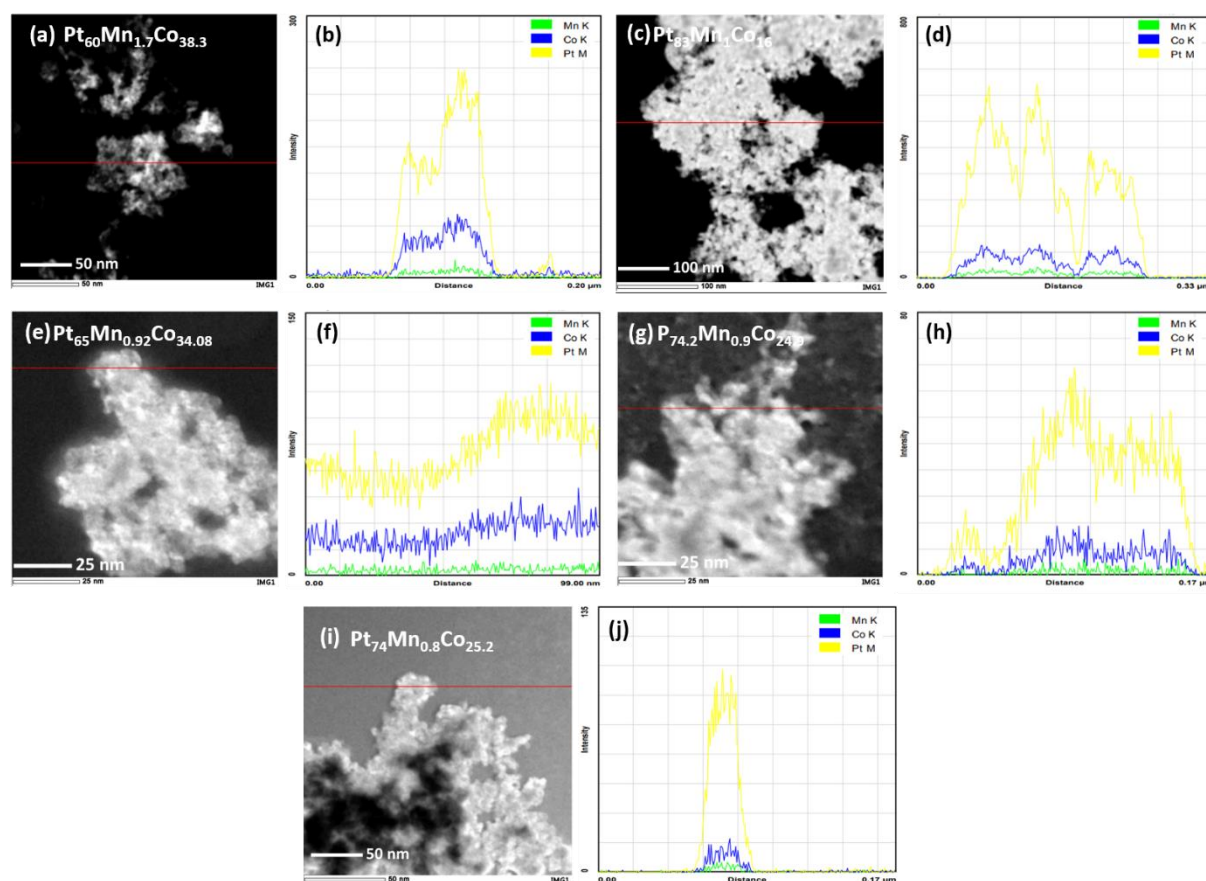


Figure 4.6: HAADF-STEM image, EDS line scan profile along red line for (a,b) $\text{Pt}_{60}\text{Mn}_{1.7}\text{Co}_{38.3}$, (c,d) $\text{Pt}_{83}\text{Mn}_1\text{Co}_{16}$, (e,f) $\text{Pt}_{65}\text{Mn}_{0.92}\text{Co}_{34.08}$, (g,h) $\text{Pt}_{74.2}\text{Mn}_{0.9}\text{Co}_{24.9}$, (i,j) $\text{Pt}_{74}\text{Mn}_{0.8}\text{Co}_{25.2}$ respectively.

The less noble metals Co and Mn, on the other hand, exist primarily in oxidised form (Figures 4.7 (b) and 4.7 (c)). Despite the presence of Co and Mn in the oxidised state, XRD examination does not show any distinguishable peak for metal oxide, confirming the development of metal alloy as the primary material and the oxides being likely present on the surface as discovered by XPS. The reduced binding energies observed for the Pt 4f peaks in all XPS spectra of the $\text{Pt}_{100-x}(\text{MnCo})_x$ ($16 < x < 41$) alloys (Figure 4.7 (d)) corroborate this contention. This evidently indicates that an electron transfer mechanism occurs from Co and Mn to Pt, resulting in it being electron rich.[36-37] In Figure 4.8, deconvoluted XPS spectra for remaining $\text{Pt}_{100-x}(\text{MnCo})_x$ ($16 < x < 41$) alloys were displayed, together with comm. Pt/C and the fraction of Pt^0 and Pt^{+2} content in each catalyst (4.8 (f)).

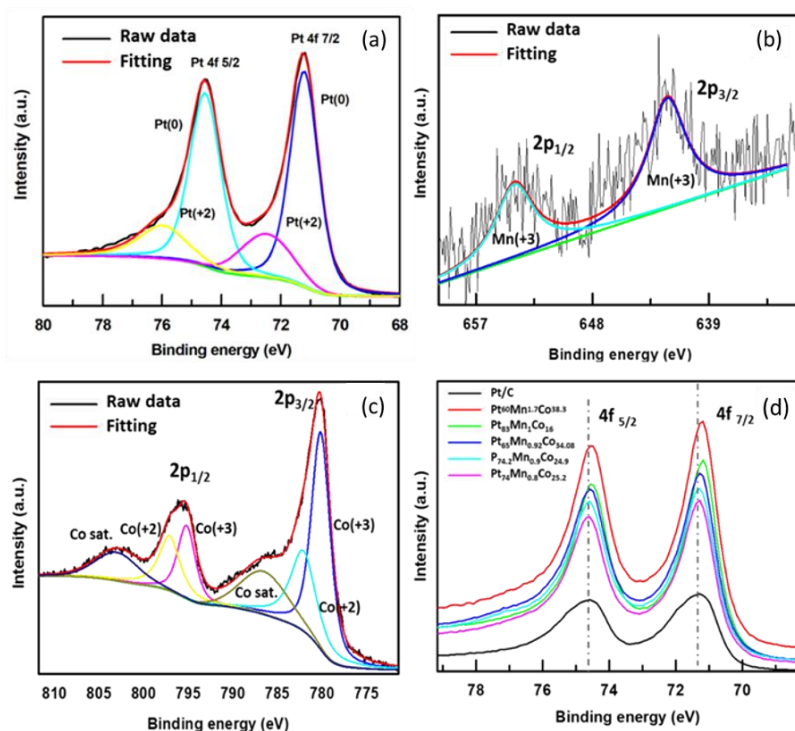


Figure 4.7: High resolution XPS peak for $Pt_{60}Mn_{1.7}Co_{38.3}$ catalyst (a) 4f Pt, (b) 2p Mn, (c) 2p Co and, (d) 4f Pt peaks of various catalyst.

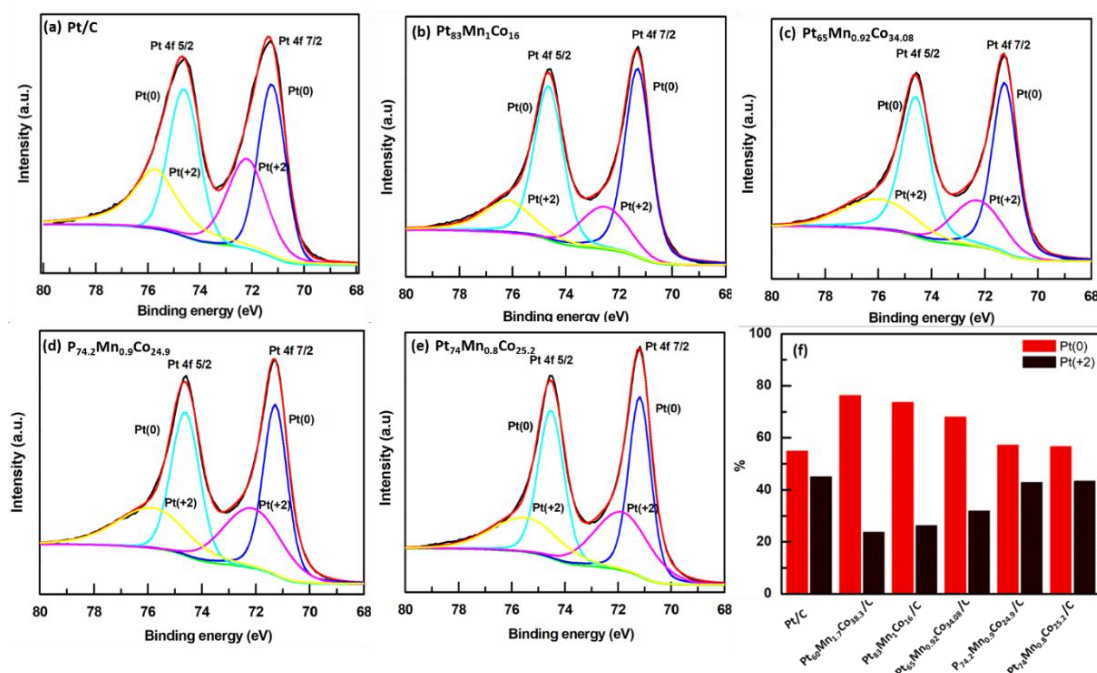


Figure 4.8: Deconvoluted XPS spectra for comm.Pt/C along with remaining $Pt_{100-x}(MnCo)_x$ ($16 < x < 41$) alloys (a-e), the fraction of Pt^0 and Pt^{+2} -content in each catalyst (f). (b) Electro-catalytic properties of $Pt_{100-x}(MnCo)_x$ alloys:

The electrochemically active surface area (ECSA) of all carbon loaded $\text{Pt}_{100-x}(\text{MnCo})_x/\text{C}$ ($16 < x < 41$) alloys, as well as comm. Pt/C and $\text{Pt}_{81}\text{Co}_{19}\text{-NPs/C}$, was determined using cyclic voltammetry (CV) in N_2 saturated 0.5 M H_2SO_4 solution at 50 mV/s, and the CVs obtained (after stabilisation over several cycles) are shown in Figure 4.9. The electrochemical surface area (m^2/g) was estimated using a monolayer charge on platinum ($210 \mu\text{C}/\text{cm}^2$), platinum loading, and the integrated charge in hydrogen adsorption and desorption. The ECSA for comm. 20% Pt/C and $\text{Pt}_{81}\text{Co}_{19}$, $\text{Pt}_{60}\text{Mn}_{1.7}\text{Co}_{38.3}$, $\text{Pt}_{83}\text{Mn}_1\text{Co}_{16}$, $\text{Pt}_{65}\text{Mn}_{0.92}\text{Co}_{34.08}$, $\text{Pt}_{74.2}\text{Mn}_{0.9}\text{Co}_{24.9}$, and $\text{Pt}_{74}\text{Mn}_{0.8}\text{Co}_{25.2}$ was found to be $46.25 \text{ m}^2/\text{g}$, $17 \text{ m}^2/\text{g}$, $8 \text{ m}^2/\text{g}$, $18 \text{ m}^2/\text{g}$, $12 \text{ m}^2/\text{g}$, $12 \text{ m}^2/\text{g}$, and $17 \text{ m}^2/\text{g}$ respectively. The decrease in ECSA values for $\text{Pt}_{100-x}(\text{MnCo})_x/\text{C}$ alloys compared to comm. Pt/C alloys, even after normalisation with only Pt mass, suggests that Mn and Co atoms are present on the surface of the catalyst together with Pt. In 1 M methanol and 0.5 M H_2SO_4 solutions, the catalytic activity of MOR for the $\text{Pt}_{100-x}(\text{MnCo})_x/\text{C}$ ($16 < x < 41$) was examined, and the relevant CV profiles are presented in Figure 4.10 (a).

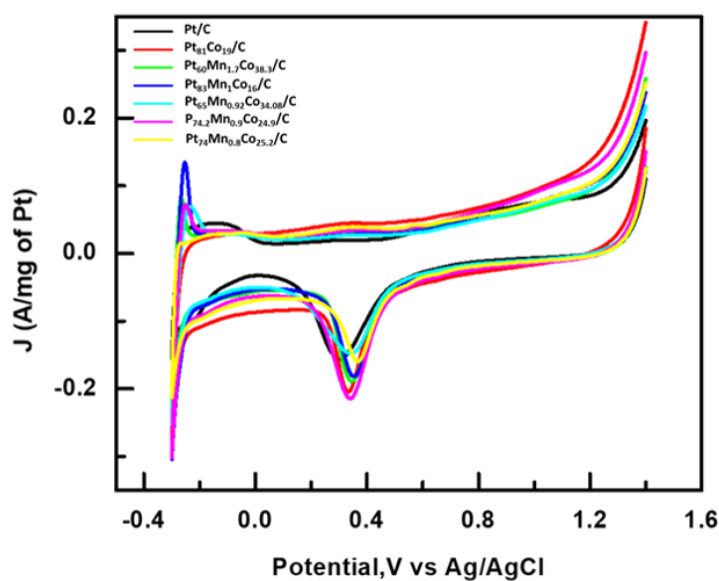


Figure 4.9: Representative CV profiles of comm. Pt/C and $\text{Pt}_{100-x}(\text{MnCo})_x/\text{C}$ ($16 < x < 41$) measured in 0.5 M H_2SO_4 .

The CV traces demonstrate that all of the catalysts have two well-defined distinctive oxidation peaks, one in the forward direction (anodic scan- I_f) and the other in the reverse direction (cathodic scan- I_b). Figure 4.10 (b) depicts the processing of current densities in terms of mass and specific activity. $\text{Pt}_{60}\text{Mn}_{1.7}\text{Co}_{38.3}/\text{C}$ has a mass activity of $0.67 \text{ A}/\text{mg}$, which is 1.3 and 1.9 times greater than $\text{Pt}_{81}\text{Co}_{19}/\text{C}$ ($0.53 \text{ A}/\text{mg}$) and comm. Pt/C ($0.35 \text{ A}/\text{mg}$), respectively. The

electrocatalytic performance of $\text{Pt}_{100-x}(\text{MnCo})_x/\text{C}$ ($16 < x < 41$) catalysts and comm. 20% Pt/C is summarised in Table 4.3.

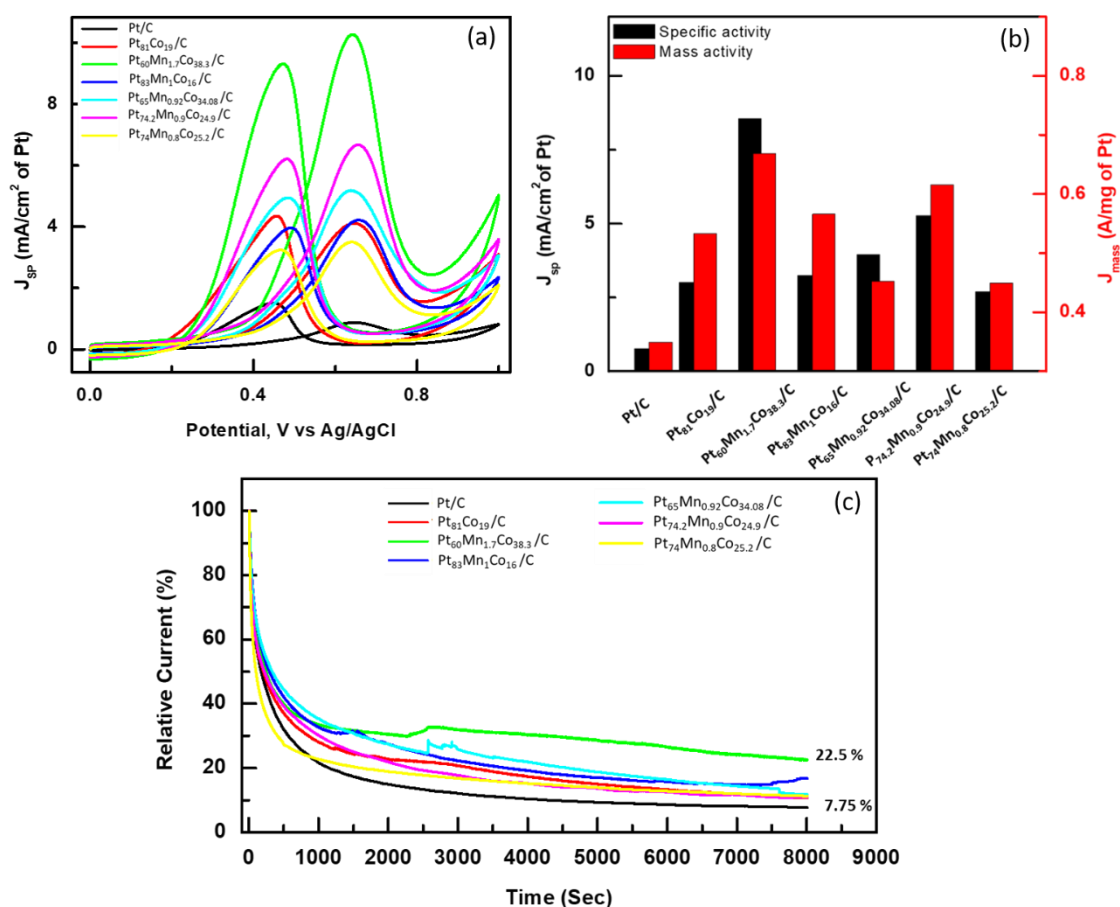


Figure 4.10: (a) The CV profiles for MOR measured using comm. Pt/C and $\text{Pt}_{100-x}(\text{MnCo})_x/\text{C}$ ($16 < x < 41$) as a catalyst in 0.5 M H_2SO_4 and 1 M methanol. (b) Corresponding J_{sp} and J_{mass} for comm. Pt/C and $\text{Pt}_{100-x}(\text{MnCo})_x/\text{C}$ ($16 < x < 41$). (c) Chronoamperometry curves for comm. Pt/C and $\text{Co}_x\text{Pt}_{100-x-400}/\text{C}$ measured at peak potential.

Apart from mass and specific activities, electrochemical endurance is a significant criterion to consider when determining the efficiency of a catalyst. A chronoamperometry (CA) test can be performed to investigate the rate of CO-poisoning during MOR and the stability of the catalyst at a fixed voltage. The CA profiles for all catalysts were recorded at peak potential for 8000 sec in a combination of 1 M methanol and 0.5 M H_2SO_4 solution, as shown in Figure 4.10 (c). All of the samples showed a dramatic decline in current at initially, followed by a slower decay. According to the literature, the drop in current with time is caused by the accumulation

and adsorption of intermediates such as CO, CHO, and COOH [38-41] species on the catalyst surface, which results in a reduction in activity and impairs the catalyst's durability.

Sample	Onset	ECSA (m ² /g)	I _f /I _b	Mass activity (A/mg)
Pt/C comm.	0.47	46.25	0.5	0.35
Pt ₈₁ Co ₁₉	0.41	17	0.74	0.54
Pt ₆₀ Mn _{1.7} Co _{38.3}	0.38	8	0.94	0.67
Pt ₈₃ Mn ₁ Co ₁₆	0.41	18	0.86	0.45
Pt ₆₅ Mn _{0.92} Co _{34.08}	0.40	12	0.85	0.45
Pt _{74.2} Mn _{0.9} Co _{24.9}	0.42	12	0.89	0.62
Pt ₇₄ Mn _{0.8} Co _{25.2}	0.42	17	0.87	0.57

Table 4.3: Summarises the electrocatalytic performance of Pt_{100-x}(MnCo)_x/C (16 < x < 41) catalysts and compares them to comm. 20% Pt/C.

Figure 4.10 (c) clearly illustrates that among all Pt_{100-x}(MnCo)_x/C (16 < x < 41) catalysts, Pt₆₀Mn_{1.7}Co_{38.3}/C displays the highest retention of initial activity after 8000 second. Furthermore, 1000 cycle accelerated durability tests were carried out, with the electrochemical results given in Figures 4.11 and 4.12. After 1000 cycles, Pt₆₀Mn_{1.7}Co_{38.3}/C has a maximum activity retention of about 55%, which is higher than the average Pt/C. Trimetallic catalysts degrade less than typical Pt/C catalysts, according to study on catalytic stability in accelerated durability testing.

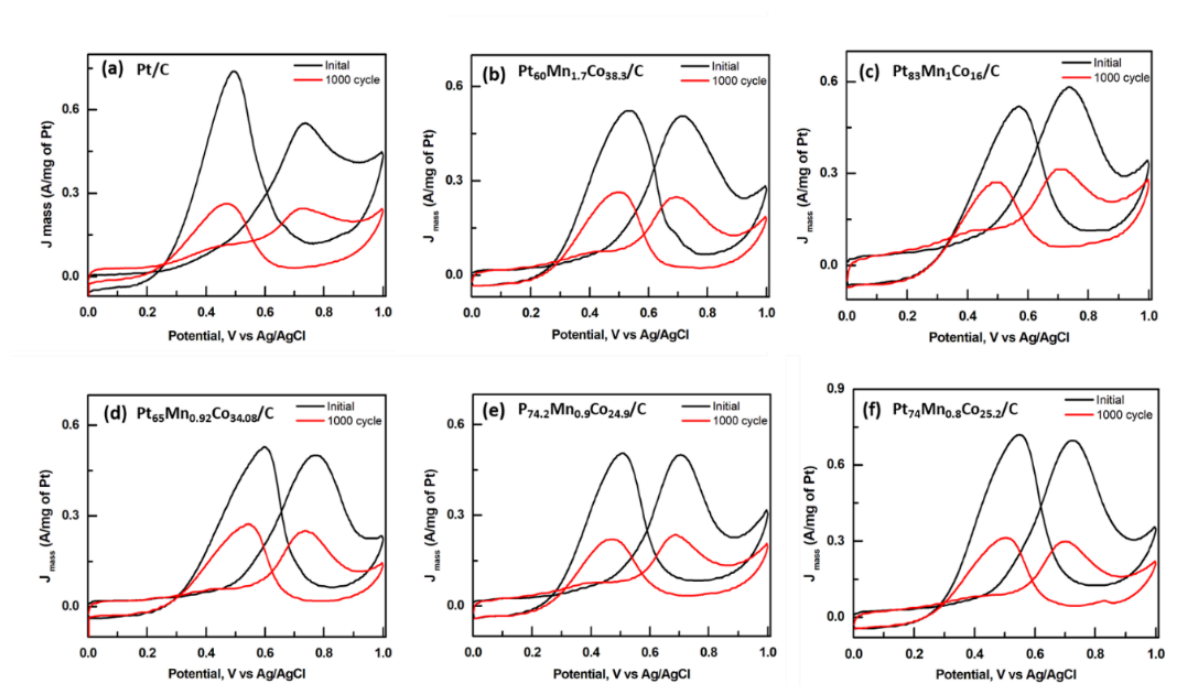


Figure 4.11: 1,000 cycle accelerated durability tests for Pt/C and $Pt_{100-x}(MnCo)_x/C$ ($16 < x < 41$) catalyst recorded in a mixture of 1M methanol and 0.5 M H_2SO_4 solution at scan rate of 100 mV/sec.

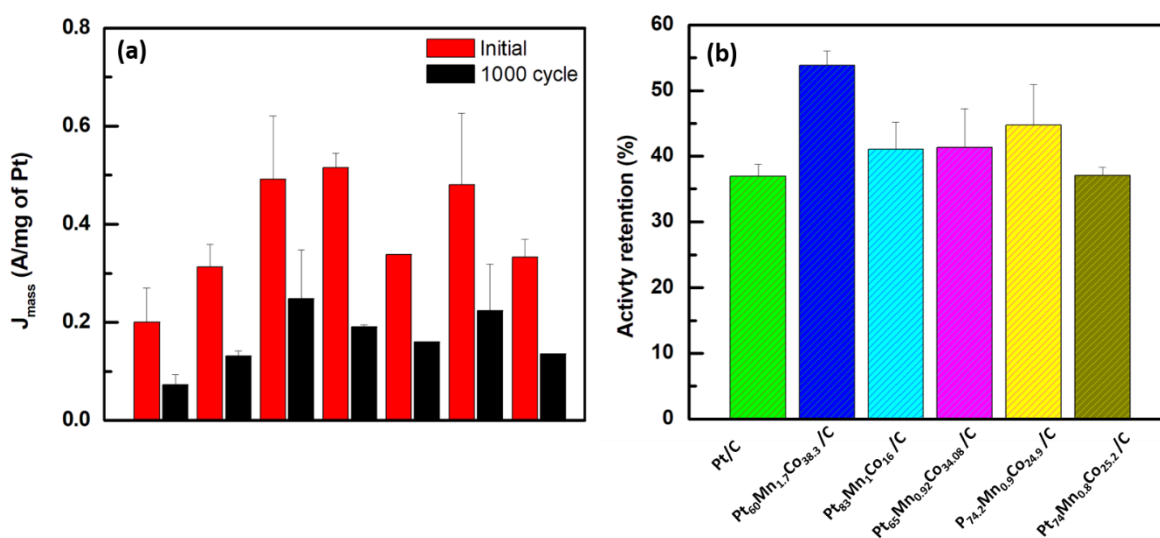


Figure 4.12: (a) Mass activity before and after accelerated durability test (b) Percent activity retention after accelerated durability test (1000 cycles).

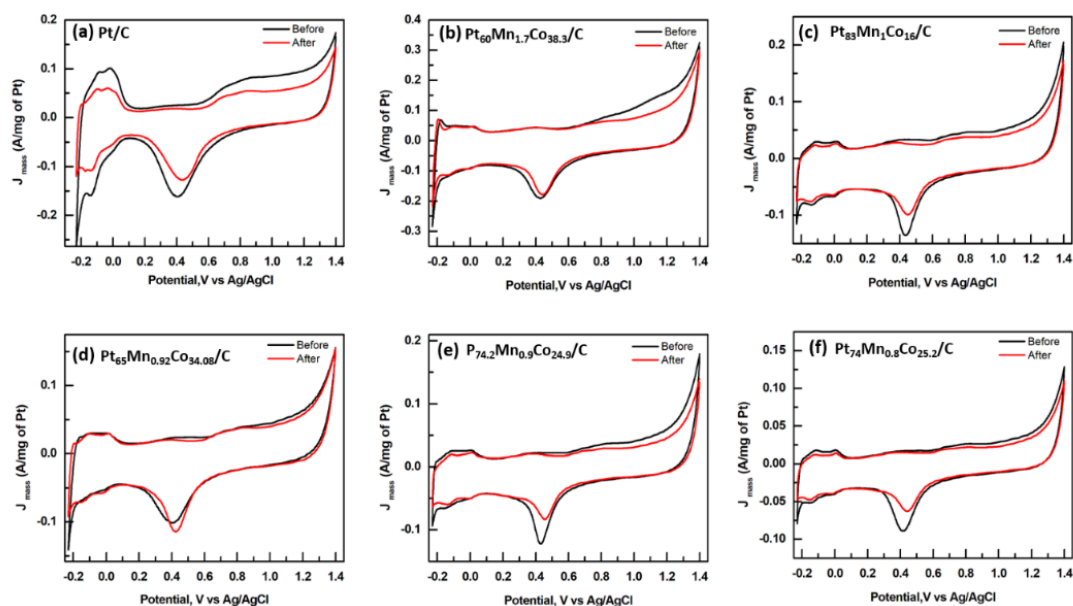


Figure 4.13: CV recorded in 0.5 M H₂SO₄ solution at 50 mV/sec before and after accelerated durability test.

Figure 4.13 shows the CV in 0.5 M H₂SO₄ solution before and after the accelerated stability test. This clearly demonstrated the ECSA of comm. Pt/C has decreased, while it has remained nearly constant for the Pt_{100-x}(MnCo)_x/C (16 < x < 41) catalyst.

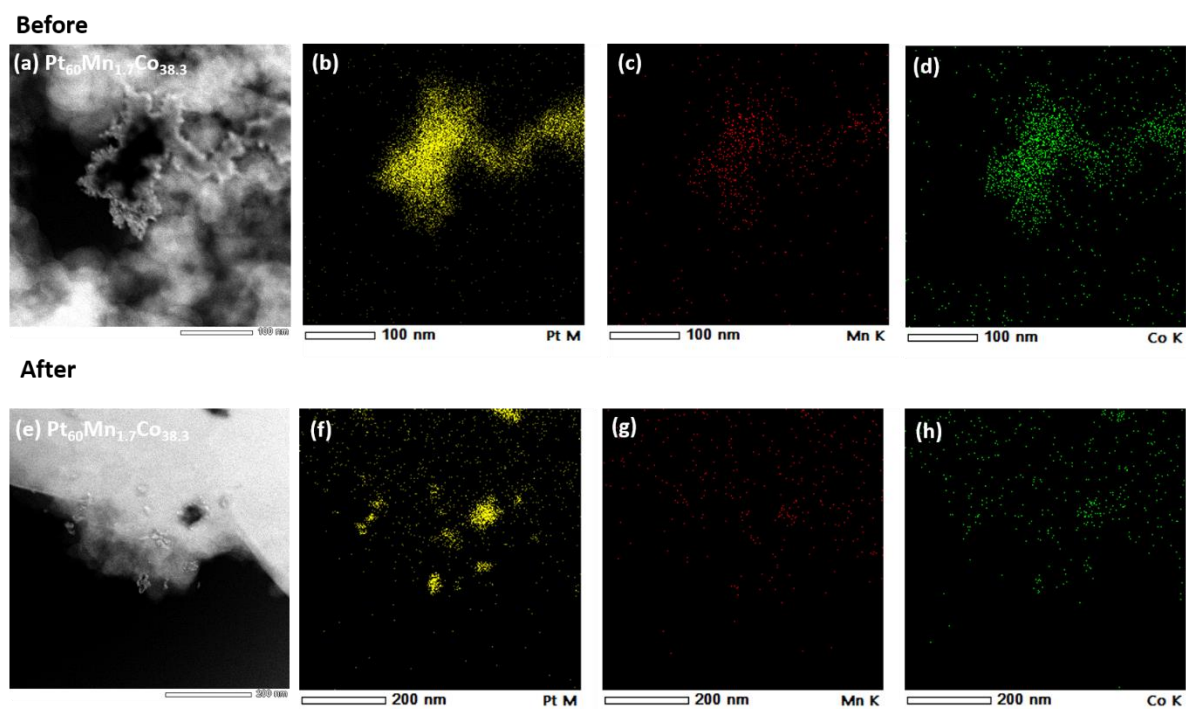


Figure 4.14: The elemental mapping for Pt₆₀Mn_{1.7}Co_{38.3}/C prior (a-d) to and following (e-h) the accelerated durability test.

Following the long-term stability test, $\text{Pt}_{60}\text{Mn}_{1.7}\text{Co}_{38.3}/\text{C}$ was analysed by TEM and ICP to further study the electrochemical changes in the surface structure and composition.

Figure 4.14 displays the elemental mapping for $\text{Pt}_{60}\text{Mn}_{1.7}\text{Co}_{38.3}/\text{C}$ before and after the stability test. All three elements are readily visible in the figure. Before and after the durability research, $\text{Pt}_{60}\text{Mn}_{1.7}\text{Co}_{38.3}/\text{C}$ exhibited the same (111) facets lattice fringes (0.2 nm) (Figure 4.15). The ICP results suggest that some Mn metal was leached during the durability test.

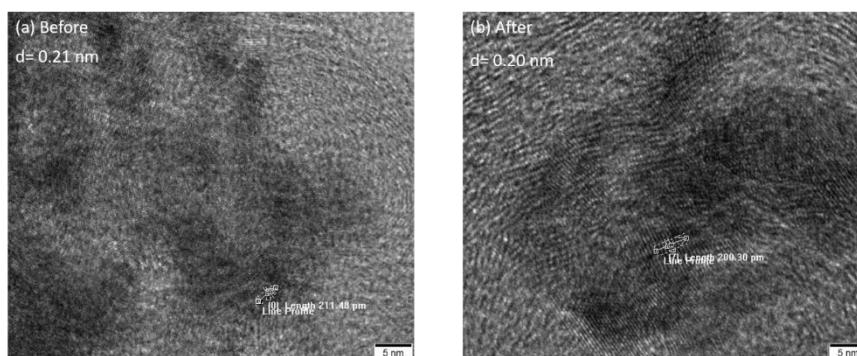


Figure 4.15: TEM image (5 nm) of $\text{Pt}_{60}\text{Mn}_{1.7}\text{Co}_{38.3}/\text{C}$ before (a) and after (b) accelerated durability test.

In addition to the aforementioned experiment, CO oxidation was carried out to investigate the tolerance of the $\text{Pt}_{100-x}(\text{MnCo})_x/\text{C}$ ($16 < x < 41$) catalyst following methanol electrooxidation. CO stripping was performed in 0.5 M H_2SO_4 solution for 10 minutes at a CO adsorption potential of -0.2 V against Ag/AgCl and a sweep rate of 50 mV/s. Figure 4.16 indicates a minor peak in comm. Pt/C around 0.53 V. The CO stripping peak for $\text{Pt}_{81}\text{Co}_{19}/\text{C}$ was marginally changed to a lower potential of 0.45 V, while the CO stripping peak for $\text{Pt}_{60}\text{Mn}_{1.7}\text{Co}_{38.3}/\text{C}$, $\text{Pt}_{83}\text{Mn}_1\text{Co}_{16}/\text{C}$, $\text{Pt}_{65}\text{Mn}_{0.92}\text{Co}_{34.08}/\text{C}$, $\text{Pt}_{74.2}\text{Mn}_{0.9}\text{Co}_{24.9}/\text{C}$, and $\text{Pt}_{74}\text{Mn}_{0.8}\text{Co}_{25.2}/\text{C}$ was further shifted to lower potentials of 0.41 V, 0.43 V, 0.43 V, 0.44 V, and 0.43 V respectively.

When compared to all other alloys, the low CO-stripping peak potential of $\text{Pt}_{60}\text{Mn}_{1.7}\text{Co}_{38.3}/\text{C}$ confirmed that CO is probably weakly adsorbed on its surface, resulting in its better catalytic activity for MOR. All of the foregoing results suggest that all $\text{Pt}_{100-x}(\text{MnCo})_x/\text{C}$ ($16 < x < 41$) catalysts have greater long-term stability and CO tolerance than conventional Pt/C catalysts.

4.4 Validation of new criterion (I_f/I_{CO}):

Based on the preceding chapter's discussion, all the catalysts were subjected to the new I_f/I_{CO} test in the 0-1 V potential window to evaluate their efficiency. As previously indicated, we initially performed an LSV with the $\text{Pt}_{100-x}(\text{MnCo})_x/\text{C}$ catalysts in 1 M methanol and 0.5 M

H₂SO₄, then swapped the electrodes to another cell containing 0.5 M H₂SO₄ and repeated the LSV in the 0 - 1 V range. Figures 4.17(a) represent the LSVs recorded in 1 M methanol and 0.5 M H₂SO₄ solutions, and Figures 4.17(b) depict the LSVs performed on electrodes relocated to cells containing just 0.5 M H₂SO₄ solution. Table 4.4 compares the average I_f/I_b and I_f/I_{CO} values for all the catalyst along with CO stripping peak potential for this experiment.

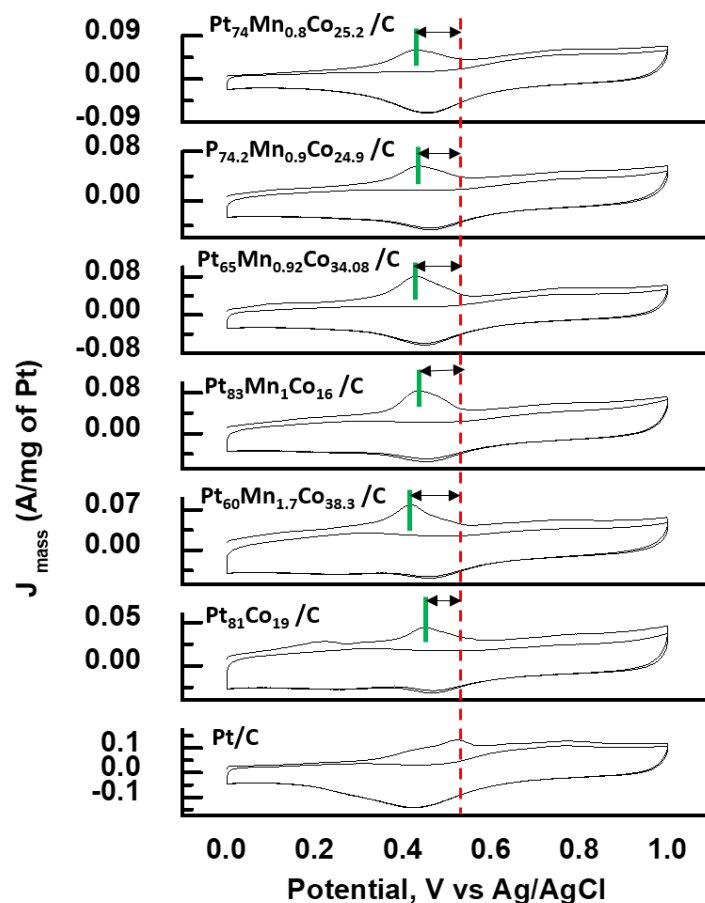


Figure 4.16: CO-stripping CV curves in N₂-saturated 0.5 M H₂SO₄ solution for Pt_{100-x}(MnCo)_x/C (16 < x < 41) catalysts.

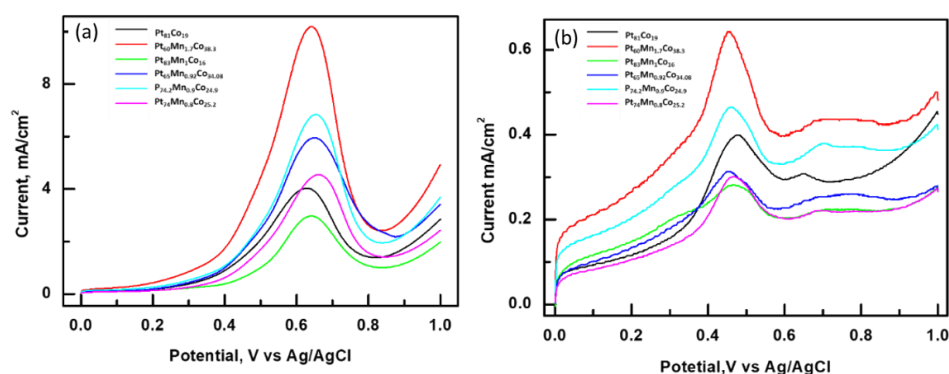


Figure 4.17: (a) LSV recorded using Pt_{100-x}(MnCo)_x/C catalysts in 0.5 M H₂SO₄ and 1 M methanol solution at different anodic limit. Scan rate: 50 mV/s (b) Cyclic voltammogram recorded in 0.5 M H₂SO₄ solution at different anodic limit Scan rate: 50 mV/s (CO stripping current).

Sample	I _f /I _b	I _f /I _{co}	Peak potential of CO stripping
Pt ₈₁ Co ₁₉	0.74	20.3	0.48
Pt ₆₀ Mn _{1.7} Co _{38.3}	0.94	30.1	0.45
Pt ₈₃ Mn ₁ Co ₁₆	0.86	28.0	0.46
Pt ₆₅ Mn _{0.92} Co _{34.08}	0.85	27.3	0.45
Pt _{74.2} Mn _{0.9} Co _{24.9}	0.89	28.1	0.46
Pt ₇₄ Mn _{0.8} Co _{25.2}	0.87	28	0.47

Table 4.4: Comparison of I_f/I_b and I_f/I_{co} value for Pt_{100-x}(MnCo)_x/C catalysts along with co stripping peak potential.

4.5. Plausible explanations for elevated MOR activity of Pt_{100-x}(MnCo)_x/C catalysts:

Based on the results of cyclic voltammetry and chronoamperometry evaluations of catalytic activity, stability, and CO tolerance, trimetallic catalysts were found to have the best activity and stability for MOR, although having lower ECSA values than conventional Pt/C.

The following factors, in our opinion, are primarily responsible for the increased activity and stability of the Pt_{100-x}(MnCo)_x/C (16 < x < 41) catalyst. Because Co and Mn have smaller atomic radii than Pt, the resulting Pt_{100-x}(MnCo)_x/C (16 < x < 41) catalyst will compress the

surface Pt layer. As previously stated, the calculated lattice constant for all $\text{Pt}_{100-x}(\text{MnCo})_x/\text{C}$ ($16 < x < 41$) catalysts is less than that of commercial Pt/C. This confirms the presence of compressive strain to some extent. According to Norskov et al., the strain effect causes changes in the metal d-band by changing the geometry of the electron population. The metal-adsorbate bond strength has been observed to alter as a result of d-band centre shifts caused by strain variation in the metal structure. Such modifications eventually result in variations in the adsorption/desorption capacities of activating reactants or intermediates[42-44], which is one of the key factors regulating catalyst electrocatalytic activity. This result agrees with the previous XPS research of the Pt 4f XPS spectra and CO stripping experiment.

The greater the amount of metallic state on the catalyst surface, the greater the number of active sites for MOR electrocatalysis. As previously discussed in XPS spectra, the comm. $\text{Pt}_{100-x}(\text{MnCo})_x/\text{C}$ ($16 < x < 41$) catalyst exhibits a negative shift in binding energy due to the difference in electronegativity. The negative shift in the catalyst $\text{Pt}_{100-x}(\text{MnCo})_x/\text{C}$ ($16 < x < 41$) is owing to the roles of Co and Mn as electronic donors and Pt as electronic acceptors. The incorporation of extra transition metals such as Mn and Co into Pt in a $\text{Pt}_{100-x}(\text{MnCo})_x/\text{C}$ ($16 < x < 41$) catalyst modifies the electronic structure of the Pt surface, which may promote reaction kinetics, facilitate electron transfer, and accelerate the removal of CO molecules to improve MOR catalytic activity, as confirmed in numerous reports.[15-19,45] These findings, as presented in Figure 4.18, serve to explain why the trimetallic $\text{Pt}_{100-x}(\text{MnCo})_x/\text{C}$ ($16 < x < 41$) catalyst is more active than Pt. This is in accordance to a previous DFT study on PtCo binary alloy catalysts with various compositions which were tested as MOR catalysts.[12] According to the findings of that study, increasing the electron density on Pt greatly increases the electrochemical performance of Pt-based catalysts.[12, 36-37]. Our findings incorporated in the present chapter support this hypothesis.

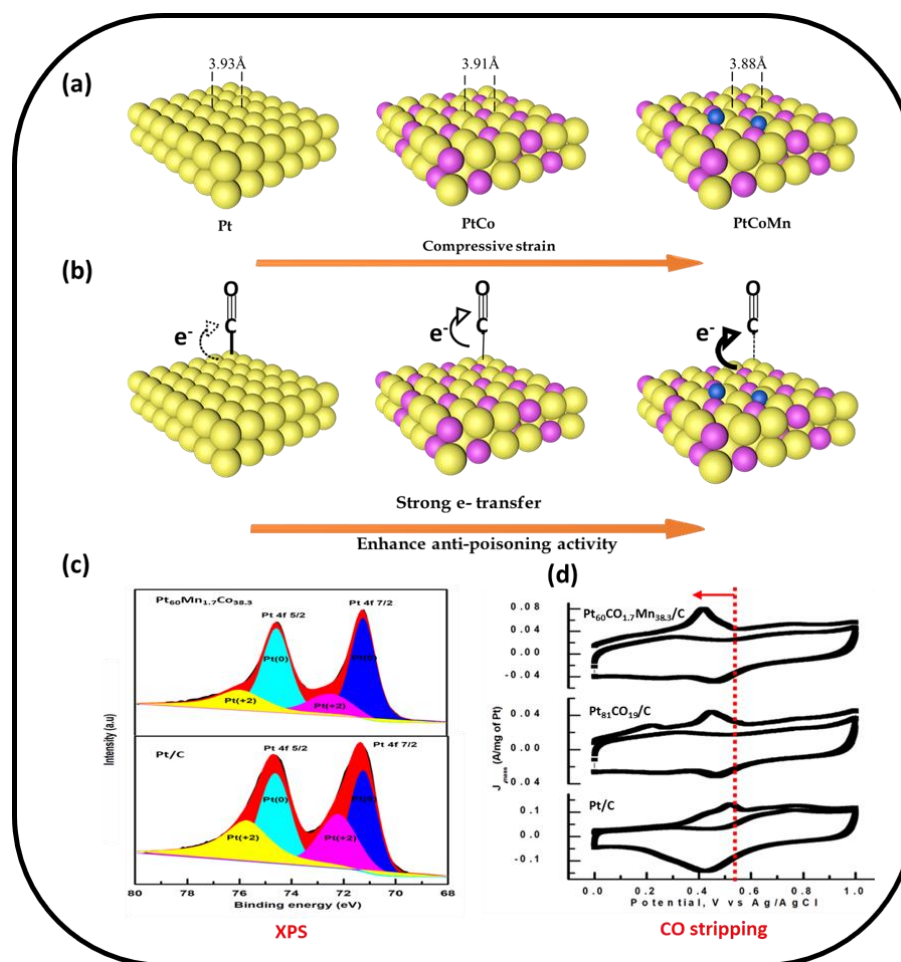


Figure 4.18: Schematic representation to explain reason for enhance activity of trimetallic alloy as compare to Pt/C (a) compression strain (b) charge transfer illustration (c) the XPS Pt 4f scan (d) and the Co stripping curve for Pt/C, Pt₈₁Co₁₉/C and Pt₆₀Mn_{1.7}Co_{38.3}/C respectively.

4.6. Conclusion:

In summary, this chapter deals with the synthesis of Pt_{100-x}(MnCo)_x (16 < x < 41) catalysts with different elemental compositions via borohydride reduction followed by hydrothermal treatment. TEM and XRD analysis clearly demonstrate the formation of alloy with particle size less than 10 nm. Among all the compositions prepared the Pt₆₀Mn_{1.7}Co_{38.3} catalyst exhibited superior mass activity toward MOR, which was 1.3 and 1.9 times higher than that of Pt₈₁Co₁₉/C and comm. Pt/C respectively. Furthermore, the chronoamperometry test for durability and the CO oxidation process for CO tolerance show that all synthesized Pt_{100-x}(MnCo)_x/C (16 < x < 41) catalysts have better current retention than conventional Pt/C.

Again, the sample with $\text{Pt}_{60}\text{Mn}_{1.7}\text{Co}_{38.3}/\text{C}$ was the best of the compositions studied, as demonstrated by both old I_f/I_b and new I_f/I_{Co} criterion. The synergistic action of Co and Mn on the Pt lattice can be attributed to the increased performance of the $\text{Pt}_{100-x}(\text{MnCo})_x/\text{C}$ ($16 < x < 41$) catalyst. The improved performance of trimetallic alloys over bimetallic alloys led us to investigate multi-metallic catalysts, as electronic structure could undergo further changes with the number and nature of added metals.

4.7. Reference:

1. Huang H, Wang X. Recent progress on carbon-based support materials for electrocatalysts of direct methanol fuel cells. *Journal of Materials Chemistry A*. 2014 Jan 6;2(18):6266-91.
2. Wang AJ, Ju KJ, Zhang QL, Song P, Wei J, Feng JJ. Folic acid bio-inspired route for facile synthesis of AuPt nanodendrites as enhanced electrocatalysts for methanol and ethanol oxidation reactions. *Journal of Power Sources*. 2016 Sep 15;326:227-34.
3. Zhang JJ, Sui XL, Huang GS, Gu DM, Wang ZB. Hierarchical carbon coated molybdenum dioxide nanotubes as a highly active and durable electrocatalytic support for methanol oxidation. *Journal of Materials Chemistry A*. 2017;5(8):4067-74.
4. Sun X, Zhu X, Zhang N, Guo J, Guo S, Huang X. Controlling and self assembling of monodisperse platinum nanocubes as efficient methanol oxidation electrocatalysts. *Chemical Communications*. 2015;51(17):3529-32.
5. Feng L, Li K, Chang J, Liu C, Xing W. Nanostructured PtRu/C catalyst promoted by CoP as an efficient and robust anode catalyst in direct methanol fuel cells. *Nano Energy*. 2015 Jul 1;15:462-9.
6. Yin Y, Liu J, Jiang G. Sunlight-induced reduction of ionic Ag and Au to metallic nanoparticles by dissolved organic matter. *ACS nano*. 2012 Sep 25;6(9):7910-9.
7. Jiang K, Zhao D, Guo S, Zhang X, Zhu X, Guo J, Lu G, Huang X. Efficient oxygen reduction catalysis by subnanometer Pt alloy nanowires. *Science Advances*. 2017 Feb 24;3(2):e1601705.
8. Maiyalagan T. Silicotungstic acid stabilized Pt–Ru nanoparticles supported on carbon nanofibers electrodes for methanol oxidation. *international journal of hydrogen energy*. 2009 Apr 1;34(7):2874-9.
9. Nagashree KL, Raviraj NH, Ahmed MF. Carbon paste electrodes modified by Pt and Pt–Ni microparticles dispersed in polyindole film for electrocatalytic oxidation of methanol. *Electrochimica acta*. 2010 Mar 1;55(8):2629-35.
10. Guo X, Guo DJ, Qiu XP, Chen LQ, Zhu WT. A simple one-step preparation of high utilization AuPt nanoparticles supported on MWCNTs for methanol oxidation in alkaline medium. *Electrochemistry communications*. 2008 Nov 1;10(11):1748-51.
11. Lei Y, Zhao G, Tong X, Liu M, Li D, Geng R. High electrocatalytic activity of Pt–Pd binary spherocrystals chemically assembled in vertically aligned TiO₂ nanotubes. *ChemPhysChem*. 2010 Jan 18;11(1):276-84.

12. Dalavi SB, Agarwal S, Deshpande P, Joshi K, Prasad BL. Disordered but efficient: Understanding the role of structure and composition of the Co–Pt alloy on the electrocatalytic methanol oxidation reaction. *The Journal of Physical Chemistry C.* 2021 Apr 5;125(14):7611-24.
13. Huang L, Jiang Z, Gong W, Shen PK. Facile fabrication of radial PtCo nanodendrites for enhanced methanol oxidation electrocatalysis. *ACS Applied Nano Materials.* 2018 Sep 4;1(9):5019-26.
14. Huang X, Zhao Z, Cao L, Chen Y, Zhu E, Lin Z, Li M, Yan A, Zettl A, Wang YM, Duan X. High-performance transition metal–doped Pt₃Ni octahedra for oxygen reduction reaction. *Science.* 2015 Jun 12;348(6240):1230-4.
15. Li K, Li X, Huang H, Luo L, Li X, Yan X, Ma C, Si R, Yang J, Zeng J. One-nanometer-thick PtNiRh trimetallic nanowires with enhanced oxygen reduction electrocatalysis in acid media: Integrating multiple advantages into one catalyst. *Journal of the American Chemical Society.* 2018 Nov 2;140(47):16159-67.
16. Huang L, Wei M, Hu N, Tsiakaras P, Shen PK. Molybdenum-modified and vertex-reinforced quaternary hexapod nano-skeletons as efficient electrocatalysts for methanol oxidation and oxygen reduction reaction. *Applied Catalysis B: Environmental.* 2019 Dec 5;258:117974.
17. Liao W, Zhou S, Wang Z, Liu F, Cao J, Wang Q. Composition-controlled effects of Pb content in PtPbRu trimetallic nanoparticles on the electrocatalytic oxidation performance of methanol. *Fuel.* 2022 Jan 15;308:122073.
18. Feng H, Luo Y, Yan B, Guo H, He L, Tian ZQ, Tsiakaras P, Shen PK. Highly stable cathodes for proton exchange membrane fuel cells: Novel carbon supported Au@PtNiAu concave octahedral core-shell nanocatalyst. *Journal of Colloid and Interface Science.* 2022 Nov 15;626:1040-50.
19. Ren Y, Li B, Lv C, Gao F, Yang X, Li L, Lu Z, Yu X, Zhang X. Defect-rich PtPdCu flower-like nanoframes with enhanced electrocatalytic activity for methanol oxidation. *Applied Surface Science.* 2022 Aug 15;593:153404.
20. Menshikov VS, Belenov SV, Nikulin AY. Effect of the morphology and composition of trimetallic PtCuAu/C catalysts on the activity and stability of the methanol oxidation reaction. *Condensed Matter and Interphases.* 2022 Mar 15;24(1):76-87.
21. Stamenkovic V, Mun BS, Mayrhofer KJ, Ross PN, Markovic NM, Rossmeisl J, Greeley J, Nørskov JK. Changing the activity of electrocatalysts for oxygen reduction by tuning

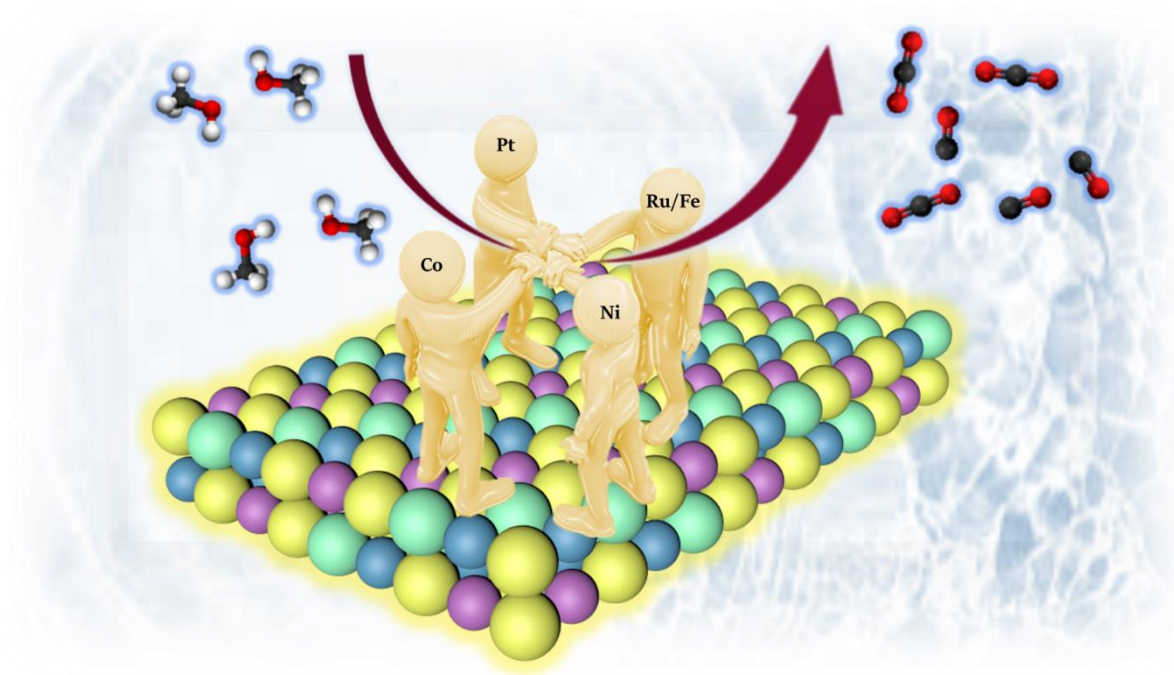
- the surface electronic structure. *Angewandte Chemie International Edition*. 2006 Apr 28;45(18):2897-901.
22. Najafpour MM, Moghaddam AN, Yang YN, Aro EM, Carpentier R, Eaton-Rye JJ, Lee CH, Allakhverdiev SI. Biological water-oxidizing complex: a nano-sized manganese–calcium oxide in a protein environment. *Photosynthesis research*. 2012 Oct;114:1-3.
 23. Najafpour MM, Allakhverdiev SI. Manganese compounds as water oxidizing catalysts for hydrogen production via water splitting: from manganese complexes to nano-sized manganese oxides. *International journal of hydrogen energy*. 2012 May 1;37(10):8753-64.
 24. Stamenkovic VR, Mun BS, Arenz M, Mayrhofer KJ, Lucas CA, Wang G, Ross PN, Markovic NM. Trends in electrocatalysis on extended and nanoscale Pt-bimetallic alloy surfaces. *Nature materials*. 2007 Mar;6(3):241-7.
 25. Shan A, Huang S, Zhao H, Jiang W, Teng X, Huang Y, Chen C, Wang R, Lau WM. Atomic-scaled surface engineering Ni-Pt nanoalloys towards enhanced catalytic efficiency for methanol oxidation reaction. *Nano Research*. 2020 Nov;13:3088-97.
 26. Kang Y, Murray CB. Synthesis and electrocatalytic properties of cubic Mn–Pt nanocrystals (nanocubes). *Journal of the American Chemical Society*. 2010 Jun 9;132(22):7568-9.
 27. Gao F, Zhang Y, Ren F, Song T, Du Y. Tiny Ir doping of sub-one-nanometer PtMn nanowires: Highly active and stable catalysts for alcohol electrooxidation. *Nanoscale*. 2020;12(22):12098-105.
 28. Peng K, Bhuvanendran N, Ravichandran S, Zhang W, Ma Q, Xu Q, Xing L, Khotseng L, Su H. Bimetallic Pt₃Mn nanowire network structures with enhanced electrocatalytic performance for methanol oxidation. *international journal of hydrogen energy*. 2020 Nov 6;45(55):30455-62.
 29. Mohanraju K, Cindrella L. One-pot surfactant-free synthesis of high surface area ternary alloys, PtMCo/C (M= Cr, Mn, Fe, Ni, Cu) with enhanced electrocatalytic activity and durability for PEM fuel cell application. *International Journal of Hydrogen Energy*. 2016 Jun 15;41(22):9320-31.
 30. Ammam M, Easton EB. Oxygen reduction activity of binary PtMn/C, ternary PtMnX/C (X= Fe, Co, Ni, Cu, Mo and, Sn) and quaternary PtMnCuX/C (X= Fe, Co, Ni, and Sn) and PtMnMoX/C (X= Fe, Co, Ni, Cu and Sn) alloy catalysts. *Journal of power sources*. 2013 Aug 15;236:311-20.

31. Bonakdarpour A, Stevens K, Vernstrom GD, Atanasoski R, Schmoeckel AK, Debe MK, Dahn JR. Oxygen reduction activity of Pt and Pt–Mn–Co electrocatalysts sputtered on nano-structured thin film support. *Electrochimica Acta*. 2007 Dec 1;53(2):688-94.
32. Ammam M, Easton EB. Ternary PtMnX/C (X= Fe, Co, Ni, Cu, Mo and, Sn) Alloy Catalysts for Ethanol Electrooxidation. *Journal of The Electrochemical Society*. 2012 Mar 21;159(5):B635.
33. Lim DH, Choi DH, Lee WD, Lee HI. A new synthesis of a highly dispersed and CO tolerant PtSn/C electrocatalyst for low-temperature fuel cell; its electrocatalytic activity and long-term durability. *Applied Catalysis B: Environmental*. 2009 Jul 15;89(3-4):484-93.
34. Ravichandran S, Bhuvanendran N, Xu Q, Maiyalagan T, Su H. Improved methanol electrooxidation catalyzed by ordered mesoporous Pt-Ru-Ir alloy nanostructures with trace Ir content. *Electrochimica Acta*. 2021 Oct 20;394:139148.
35. Shen CT, Wang KW, Tseng CJ, Lee KR, Hsueh YJ. The oxygen reduction reaction of ordered porous carbon-supported PtSn catalysts. *RSC advances*. 2016;6(50):44205-11.
36. Fan J, Qi K, Zhang L, Zhang H, Yu S, Cui X. Engineering Pt/Pd interfacial electronic structures for highly efficient hydrogen evolution and alcohol oxidation. *ACS applied materials & interfaces*. 2017 May 31;9(21):18008-14.
37. Wang Z, Yao X, Kang Y, Xia D, Gan L. Rational development of structurally ordered platinum ternary intermetallic electrocatalysts for oxygen reduction reaction. *Catalysts*. 2019 Jun 26;9(7):569.
38. Deshpande PS, Chaudhari VR, Prasad BL. Mechanistic aspects of methanol electro-oxidation reaction through cyclic voltammetry: is it correct to blame carbon monoxide for catalyst poisoning?. *Energy Technology*. 2020 May;8(5):1900955.
39. Cuesta A, Escudero M, Lanova B, Baltruschat H. Cyclic voltammetry, FTIRS, and DEMS study of the electrooxidation of carbon monoxide, formic acid, and methanol on cyanide-modified Pt (111) electrodes. *Langmuir*. 2009 Jun 2;25(11):6500-7.
40. Chen YX, Miki A, Ye S, Sakai H, Osawa M. Formate, an active intermediate for direct oxidation of methanol on Pt electrode. *Journal of the American Chemical Society*. 2003 Apr 2;125(13):3680-1.
41. Housmans TH, Wonders AH, Koper MT. Structure sensitivity of methanol electrooxidation pathways on platinum: an on-line electrochemical mass spectrometry study. *The Journal of Physical Chemistry B*. 2006 May 25;110(20):10021-31.

42. Strasser P, Koh S, Anniyev T, Greeley J, More K, Yu C, Liu Z, Kaya S, Nordlund D, Ogasawara H, Toney MF. Lattice-strain control of the activity in dealloyed core–shell fuel cell catalysts. *Nature chemistry*. 2010 Jun;2(6):454-60.
43. Nilsson A, Pettersson LG, Hammer B, Bligaard T, Christensen CH, Nørskov JK. The electronic structure effect in heterogeneous catalysis. *Catalysis Letters*. 2005 Apr;100:111-4.
44. Abild-Pedersen F, Greeley J, Nørskov JK. Understanding the effect of steps, strain, poisons, and alloying: methane activation on Ni surfaces. *Catalysis letters*. 2005 Nov;105:9-13.
45. Wang D, Chen Z, Huang YC, Li W, Wang J, Lu Z, Gu K, Wang T, Wu Y, Chen C, Zhang Y. Tailoring lattice strain in ultra-fine high-entropy alloys for active and stable methanol oxidation. *Science China Materials*. 2021 Oct;64(10):2454-66.

Chapter-5

Highly efficient $\text{Pt}_x(\text{CoNiM})_{100-x}$ quaternary anode catalysts for methanol electrooxidation



The previous chapter concentrated on the synthesis of trimetallic alloy for improved methanol oxidation reaction (MOR) activity through the incorporation of a small amount of Mn in bimetallic alloy. The superior performance of trimetallic alloys over bimetallic alloys drove us to look into multi-metallic catalysts, as electronic structure varies with the number and characteristics of added metals. Therefore, we decided to try quaternary alloys. Accordingly, we synthesized quaternary alloys of Pt, Co, Ni, and Fe/Ru metals in various compositions and analysed them for MOR. The extra metal is chosen based on its bifunctional and electronic properties, which could result in increased activity of the multi-metallic alloy.

5.1 Introduction:

As it is well discussed in previous chapters, CO is the prime poisoning species responsible for catalyst deactivation during MOR. Thus, numerous attempts have been made to design and synthesize Pt-based alloy catalysts by alloying platinum with other elements. There are two ways to accomplish this: by using a bifunctional effect and by modifying the electrical structure. The CO-poisoned platinum can be recovered by oxidizing CO into CO₂ via the interaction of surface CO with oxygen species (like -OH) adsorbed on a water-activating element such as Ru.[1,2] In addition, we can change the electronic structure of Pt by introducing elements with lower electronegativity than Pt, such as M (M=Ni, Co, Fe, and so on).[3,6] The electron donation of M to Pt would affect the electrical characteristics of the Pt 4f peaks. Our previous chapter suggests that such changed electronic characteristics of Pt boost the electrocatalytic activity of Pt-based alloys. The shift in d-electron density from M to Pt reduces the density of state (DOS) on the Fermi level and thus the energy of the Pt-CO bond.[7] As a result, the optimum candidate for methanol oxidation in DMFCs could be constructed by taking into account appropriate materials that affect methanol electrooxidation based on either the bifunctional or electronic effect.[8] Aside from CO poisoning, the excessive usage of the precious metal Pt in electrodes has stymied the commercialization of DMFCs. Using a multi-metallic alloy is one method for reducing the amount of Pt added and increasing its use efficiency.[9-17]

In the last chapter, we described the synthesis of trimetallic alloys and how they can be used as electrocatalysts for MOR with improved activity and stability. As the electronic structure of trimetallic alloys changes with the number and characteristics of add metals, we decided to examine multi-metallic catalysts in detail. In this chapter, we choose to design quaternary metal alloys based on the bifunctional and electronic effect of added metal. In this study, we synthesized quaternary metal alloys by microwave assisted method.

The use of microwave heating to synthesize quaternary metal alloys is a novel and unique approach. Microwave synthesis has various advantages over traditional synthesis methods, including shorter reaction times, enhanced reaction kinetics, and lower energy use. Microwave heating also provides accurate temperature control, which is important when preparing high-quality quaternary metal alloys.

According to research conducted in our group previously, Pt and Co metal are known to form stable alloys with different compositions such as Pt₇₅Co₂₅, Pt₅₀Co₅₀ and Pt₂₅Co₇₅. [7] Taking

this fact into consideration, in this chapter we have synthesized $\text{Pt}_{75}(\text{CoNiM})_{25}$, $\text{Pt}_{50}(\text{CoNiM})_{50}$ and $\text{Pt}_{25}(\text{CoNiM})_{75}$ alloy where M is Ru or Fe.

5.2. Experimental:

We used cobalt (II) acetylacetonate, platinum (II) acetylacetonate, nickel (II) acetylacetonate, ruthenium (III) acetylacetonate, iron (III) acetylacetonate, commercial Pt/C (comm. Pt/C) with 20% Pt, oleylamine, and benzyl alcohol from Sigma Aldrich for this study. Local authorities provided the methanol, ethanol, and sulfuric acid. All reagents were of analytical quality and were not purified or processed further.

(a) Synthesis of nanoparticles:

As discussed in the introduction we used the thermal breakdown procedure under microwave conditions to create $\text{Pt}_x(\text{CoNiM})_{100-x}$ ($x=25-75$ and $M=\text{Ru}$ or Fe) alloy samples. A stoichiometric amount of all metal salt at specific ratios were taken in a round-bottom flask conventionally held under an inert environment. 30 mL of benzyl alcohol and 2 mL of oleylamine were added to these precursor combinations. This reaction mixture was sonicated for 15 minutes before being warmed to 80 °C to ensure complete precursor dissolution. Finally, this reaction flask was placed in a microwave oven set to 700 W, which caused the temperature of the mixture in the flask to rise to 205 °C (measured by an infrared noncontact thermometer). The colour of the combination was seen to change from yellow to black practically instantly. The microwave irradiation was extended for 5 minutes to ensure that the reaction was completed. Following that, the products were centrifuged, washed with ethanol several times, and then dried at room temperature. The products generated were determined to be $\text{Pt}_x(\text{CoNiM})_{100-x}$ ($x=25-75$ and $M=\text{Ru}$ or Fe) alloys of varied composition based on the PXRD examination (vide infra).

(b) Characterizations of $\text{Pt}_x(\text{CoNiM})_{100-x}$ alloy:

Various experimental approaches were used to characterize these synthesized $\text{Pt}_x(\text{CoNiM})_{100-x}$ alloys. Based on PXRD analysis, the $\text{Pt}_x(\text{CoNiM})_{100-x}$ formation and preliminary confirmation of alloy formation were concluded. The samples for XRD were prepared on a glass slide using ground powder. X-ray diffraction (XRD) investigation was carried out on an X'pert Pro model PANalytical diffractometer from Philips PANalytical instruments, which was set to 40 kV and 30 mA with $\text{Cu K}\alpha$ (1.5418) radiation. The samples were scanned at a rate of 0.3° per minute in a 2θ range from 20° to 80°. An inductively coupled Microwave Plasma Atomic Emission

Spectrometer was used to determine the final elemental composition of $\text{Pt}_x(\text{CoNiM})_{100-x}$ alloys (MP-AES; Model: Agilent, 4200). Transmission Electron Microscopy (TEM) was performed using a TECHNAI G220 STWIN (T-20) apparatus set to 200 keV and a LaB6 filament as an electron source. The electron source is a 200 keV LaB6 filament. The particle size distributions were established by personally measuring the size of at least 200 particles from different photos. JEOL's JEMF200 instrument was used to capture high resolution TEM (HRTEM) images, high angle annular dark field scanning TEM (HAADF-STEM) images, and energy dispersive X-ray spectroscopy (EDS) mapping of Co and Pt (Olympus camera, model-XAROSA).

(c) Electrochemical Measurements:

At room temperature, a CH Instruments 660B electrochemical workstation with a three-electrode setup was employed for the electrochemical measurements. As a working electrode, a glassy carbon electrode drop casted with electrocatalyst material was employed. As counter and reference electrodes, Pt wire and Ag/AgCl electrode were used. The prepared $\text{Pt}_x(\text{CoNiM})_{100-x}$ alloy samples were initially loaded on Vulcan XC-72 carbon, ensuring a 20 wt % loading of the corresponding alloy, and these will be referred to as $\text{Pt}_x(\text{CoNiM})_{100-x}/\text{C}$. We used these samples with a carbon loading of 20 % for all electrochemical studies. In a typical loading technique, 5 mg of $\text{Pt}_x(\text{CoNiM})_{100-x}$ NPs and 20 mg of Vulcan XC-72 carbon were disseminated separately in 10 mL of ethanol for 30 minutes using ultrasonication. The sample dispersion was then added to this carbon dispersion and agitated for 12 hours before centrifugation, acetone wash, and ambient condition drying. Following that, electrocatalyst ink was made by dispersing 2 mg of comm. Pt/C (20 wt% Pt) in 200 μL of a 1:1 ethanol:water combination containing 5 % nafion solution. 2 μL of this dispersion was drop casted on a glassy carbon electrode and dried at room temperature. Similar techniques were used to prepare the $\text{Pt}_x(\text{CoNiM})_{100-x}/\text{C}$ electrodes. To estimate the electrochemically active surface area (ECSA) of Pt, cyclic voltammograms (CVs) were first recorded in N_2 (g) saturated aqueous 0.5 M H_2SO_4 at a scan rate of 50 mV/s in a potential range of 1.4 to 0.3 V vs Ag/AgCl. The MOR studies were carried out in a N_2 (g) saturated 0.5 M H_2SO_4 and 1 M CH_3OH aqueous solution, and CVs were collected at a scan rate of 50 mV/s in a potential range of 0.0 to 1.0 V vs Ag/AgCl.

5.3. Result and Discussion:

(a) Crystal Structure and Microstructural Analysis:

Figure 5.1 shows the XRD patterns for as-synthesized $\text{Pt}_x(\text{CoNiM})_{100-x}$ alloys. XRD peak shifting in alloys is a result many factors like lattice distortion, solid solution formation, and grain size effects. By analysing these peak shifts, we can gain insights into the structural changes that occur within alloys as a result of their composition and processing conditions. It should be noted that the alloy compositions mentioned in Figure 5.1 were determined using ICP-AES analysis. The diffraction peaks at 39.8° , 46.4° , and 67.8° for Pt/C in the PXRD patterns are attributed to the Pt (111), (200), and (220) facets, respectively. The position of all peaks in $\text{Pt}_x(\text{CoNiM})_{100-x}$ alloys was found to be somewhat displaced to higher 2θ values when compared to the XRD of Pt/C. (Figure 5.1). This confirm the formation of alloy.

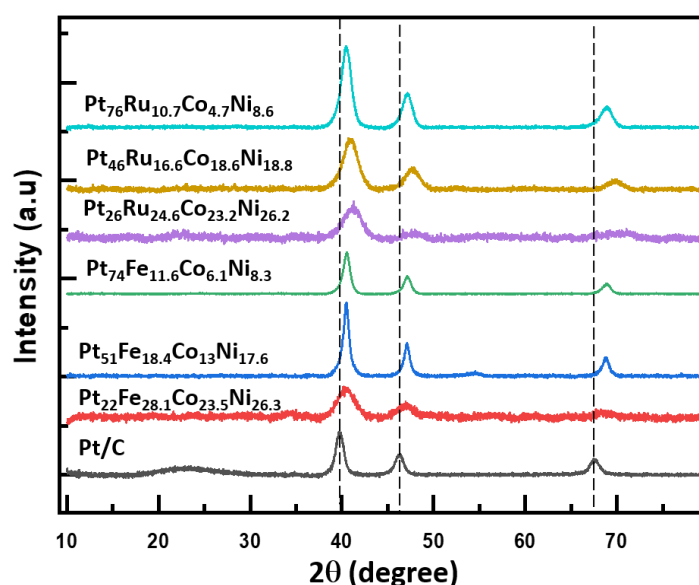


Figure 5.1: XRD patterns for $\text{Pt}_x(\text{CoNiM})_{100-x}$ alloy.

TEM images for $\text{Pt}_x(\text{CoNiFe})_{100-x}$ and $\text{Pt}_x(\text{CoNiRu})_{100-x}$ are shown in figure 5.2. TEM images indicate that all generated materials have roughly spherical morphology with individual particle sizes ranging from 4.3 to 7.5 nm, confirming that the synthesized materials are nanoparticles (NPs). The average TEM particle sizes for $\text{Pt}_{22}\text{Fe}_{28.1}\text{Co}_{23.5}\text{Ni}_{26.3}$, $\text{Pt}_{51}\text{Fe}_{18.4}\text{Co}_{13}\text{Ni}_{17.6}$, $\text{Pt}_{74}\text{Fe}_{11.6}\text{Co}_{6.1}\text{Ni}_{8.3}$, $\text{Pt}_{26}\text{Ru}_{24.6}\text{Co}_{23.2}\text{Ni}_{26.2}$, $\text{Pt}_{46}\text{Ru}_{16.6}\text{Co}_{18.6}\text{Ni}_{18.8}$ and $\text{Pt}_{76}\text{Ru}_{10.7}\text{Co}_{4.7}\text{Ni}_{8.6}$ NPs were 4.7 ± 1.1 nm, 4.8 ± 1.1 nm, 6.6 ± 1.6 nm, 5.8 ± 1.4 nm, 4.3 ± 0.7 nm, and 7.5 ± 1.3 nm, respectively.

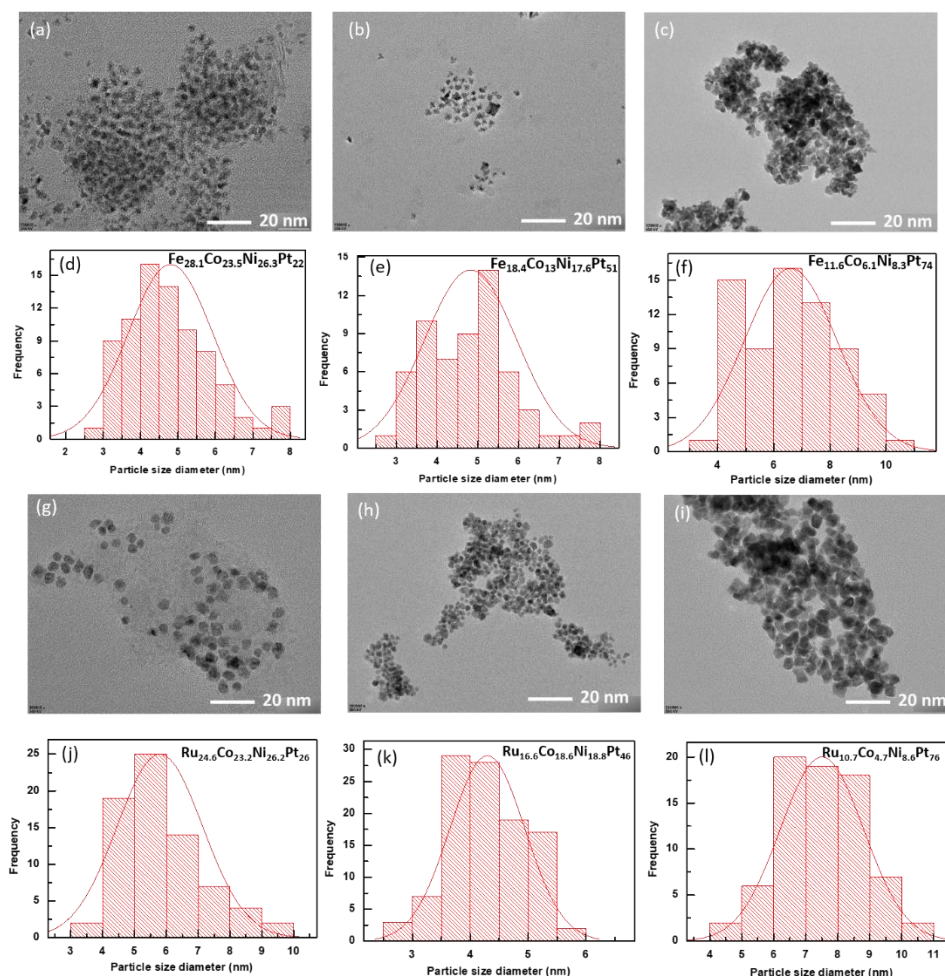


Figure 5.2: TEM images and corresponding particle size distribution plots of $Pt_x(CoNiM)_{100-x}$ alloys.

We employed elemental mapping to determine the distribution of Pt, Ni, Co and Ru/Fe in $Pt_{22}Fe_{28.1}Co_{23.5}Ni_{26.3}$, $Pt_{51}Fe_{18.4}Co_{13}Ni_{17.6}$, $Pt_{74}Fe_{11.6}Co_{6.1}Ni_{8.3}$, $Pt_{26}Ru_{24.6}Co_{23.2}Ni_{26.2}$, $Pt_{46}Ru_{16.6}Co_{18.6}Ni_{18.8}$ and $Pt_{76}Ru_{10.7}Co_{4.7}Ni_{8.6}$ sample (figure 5.3 and 5.4). These findings unambiguously indicate the presence of Pt, Ni, Co and Ru/Fe in all of the analysed samples.

(b) Electro-catalytic properties of $Pt_x(CoNiM)_{100-x}$ alloys:

The electrochemically active surface area (ECSA) of all carbon loaded $Pt_x(CoNiM)_{100-x} / C$ alloys was determined using cyclic voltammetry (CV) in N_2 saturated 0.5 M H_2SO_4 solution at 50 mV/s, and the CVs obtained (after stabilisation over several cycles) are shown in Figure 5.5. The electrochemical surface area (m^2/g) was estimated using a monolayer charge on platinum ($210 \mu C/cm^2$), platinum loading, and the integrated charge in hydrogen adsorption and desorption.

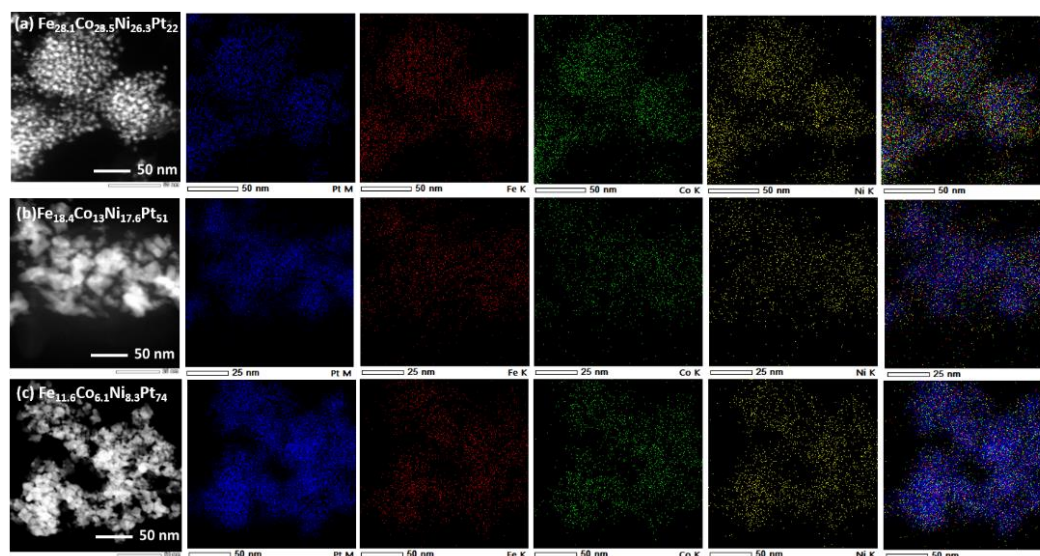


Figure 5.3: Elemental mapping for (a) $\text{Pt}_{22}\text{Fe}_{28.1}\text{Co}_{23.5}\text{Ni}_{26.3}$, (b) $\text{Pt}_{51}\text{Fe}_{18.4}\text{Co}_{13}\text{Ni}_{17.6}$, (c) $\text{Pt}_{74}\text{Fe}_{11.6}\text{Co}_{6.1}\text{Ni}_{8.3}$.

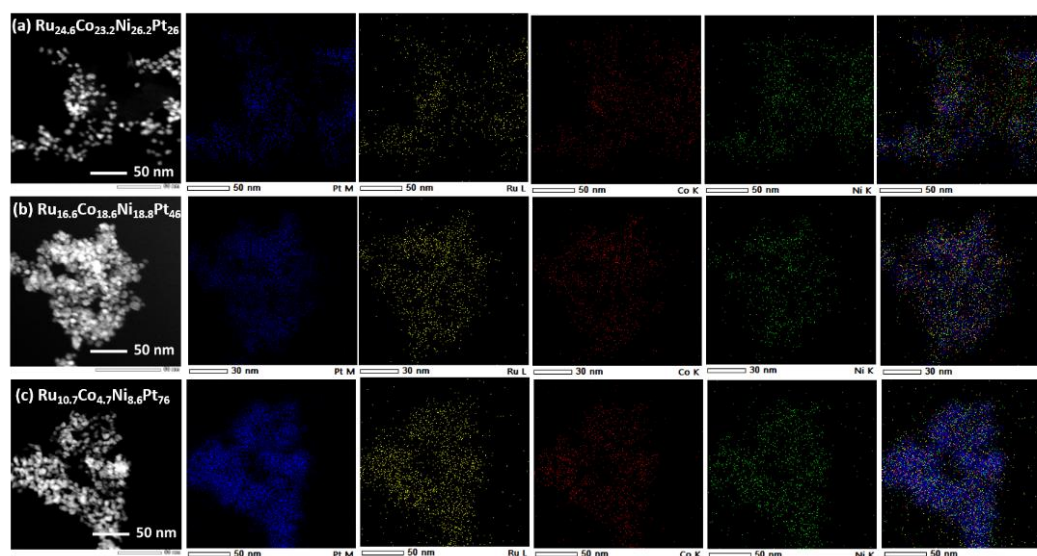


Figure 5.4: Elemental mapping for (a) $\text{Pt}_{26}\text{Ru}_{24.6}\text{Co}_{23.2}\text{Ni}_{26.2}$, (b) $\text{Pt}_{46}\text{Ru}_{16.6}\text{Co}_{18.6}\text{Ni}_{18.8}$, (c) $\text{Pt}_{76}\text{Ru}_{10.7}\text{Co}_{4.7}\text{Ni}_{8.6}$.

The ECSA for comm. 20% Pt/C and $\text{Pt}_{22}\text{Fe}_{28.1}\text{Co}_{23.5}\text{Ni}_{26.3}$, $\text{Pt}_{51}\text{Fe}_{18.4}\text{Co}_{13}\text{Ni}_{17.6}$, $\text{Pt}_{74}\text{Fe}_{11.6}\text{Co}_{6.1}\text{Ni}_{8.3}$, $\text{Pt}_{26}\text{Ru}_{24.6}\text{Co}_{23.2}\text{Ni}_{26.2}$, $\text{Pt}_{46}\text{Ru}_{16.6}\text{Co}_{18.6}\text{Ni}_{18.8}$ and $\text{Pt}_{76}\text{Ru}_{10.7}\text{Co}_{4.7}\text{Ni}_{8.6}$ sample was found to be 47.25 m²/g, 9 m²/g, 6.2 m²/g, 8.8 m²/g, 11.4 m²/g, 8.8 m²/g, and 4 m²/g respectively. The decrease in ECSA values for $\text{Pt}_x(\text{CoNiM})_{100-x}/\text{C}$ alloys compared to comm. Pt/C alloys, even after normalisation with only Pt mass, suggests that other metal like Co, Ni, Fe/Ru are also present on the surface of the catalyst together with Pt.

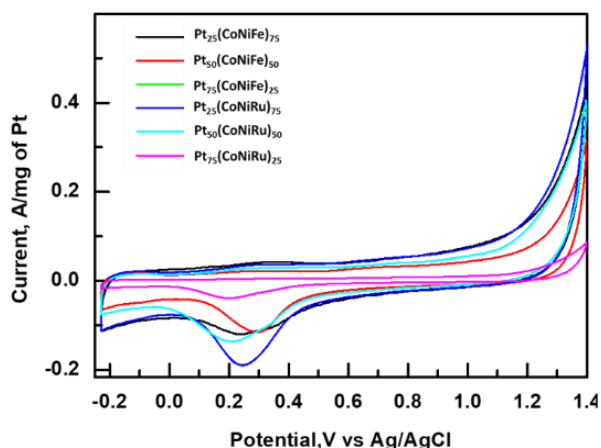


Figure 5.5: Representative CV profiles of $Pt_x(CoNiM)_{100-x}/C$ measured in 0.5 M H_2SO_4 .

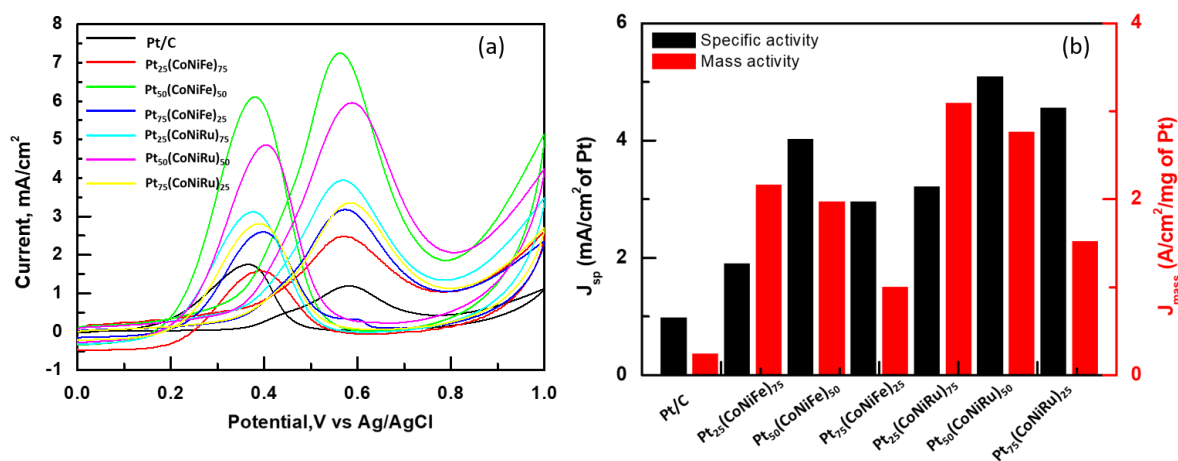


Figure 5.6: (a) The CV profiles for MOR measured using comm. Pt/C and $Pt_x(CoNiM)_{100-x}/C$ catalyst in 0.5 M H_2SO_4 and 1 M methanol. (b) Corresponding J_{sp} and J_{mass} for comm. Pt/C and $Pt_x(CoNiM)_{100-x}/C$.

The catalytic activity of MOR for the $Pt_x(CoNiM)_{100-x}/C$ was investigated in 1 M methanol and 0.5 M H_2SO_4 solutions, and the corresponding CV profiles are shown in Figure 5.6 (a). The CV traces show that each catalyst has two unique oxidation peaks, one in the forward direction (anodic scan- I_f) and one in the reverse direction (cathodic scan- I_b). Figure 5.6 (b) depicts the processing of current densities in terms of mass and specific activity. I_f/I_b value calculated for comm. 20% Pt/C and $Pt_{22}Fe_{28.1}Co_{23.5}Ni_{26.3}$, $Pt_{51}Fe_{18.4}Co_{13}Ni_{17.6}$, $Pt_{74}Fe_{11.6}Co_{6.1}Ni_{8.3}$, $Pt_{26}Ru_{24.6}Co_{23.2}Ni_{26.2}$, $Pt_{46}Ru_{16.6}Co_{18.6}Ni_{18.8}$ and $Pt_{76}Ru_{10.7}Co_{4.7}Ni_{8.6}$ found to be 0.5, 0.98, 0.99, 0.97, 0.93, 0.96, 0.95 respectively. In terms of activity, these alloy catalysts perform better than the catalyst studied in the previous chapter. Among all $Pt_x(CoNiM)_{100-x}/C$ alloy, Our findings show that a quaternary metal alloy containing 50% Pt and 50% of all other

metals outperforms alternative combinations, which is consistent with our group's studies and other literature[7,18-19]. Further studies like cycle stability, chronoamperometry, CO poisoning, I_f/I_{co} need to do to analyze this sample further.

5.4. Conclusion:

In conclusion, this chapter deals with the synthesis of multi-metallic alloy by simple microwave method. More specifically, we synthesized a quaternary alloy out of Pt, Co, Ni, and Fe/Ru metal. Metals are chosen based on their use as a bifunctional or electronic effect, which leads to increased catalytic activity. According to our findings, a quaternary metal alloy including containing 50% Pt and 50% of all other metals performs better than other combinations, which is consistent with our group's research and other literature. We would like to conduct a long-term stability and CO poisoning investigation for this catalyst, in addition to OER and ORR.

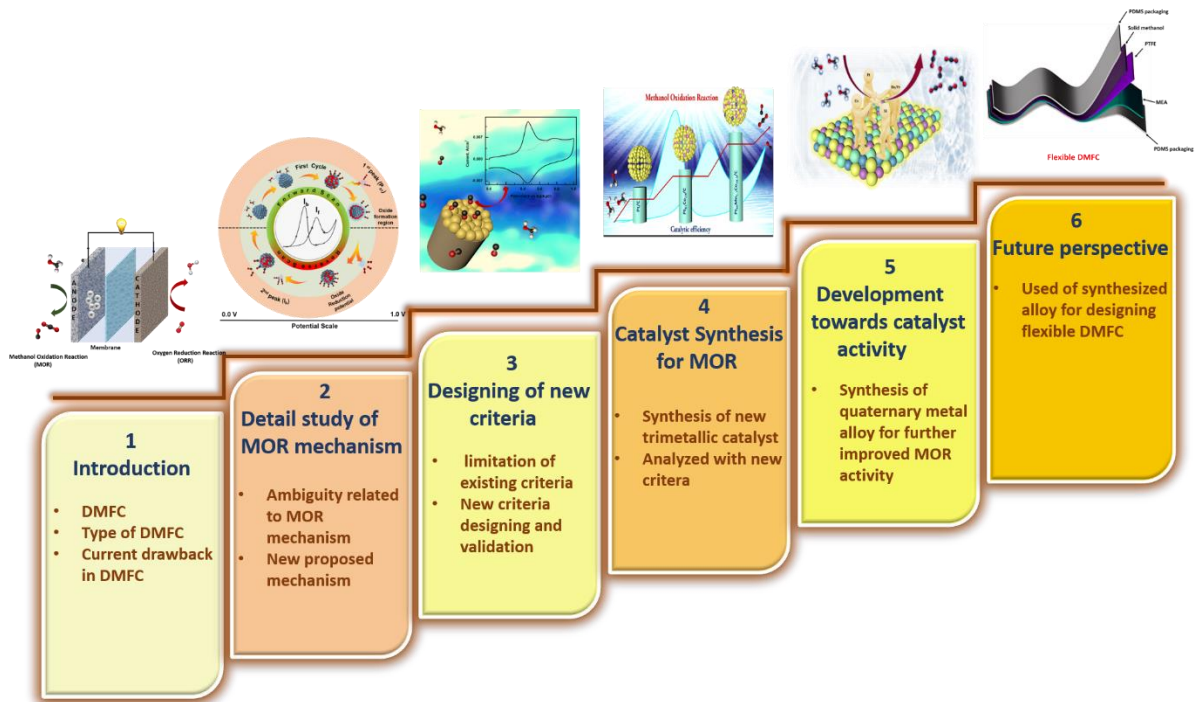
5.5. Reference:

1. Watanabe MA, Motoo S. Electrocatalysis by ad-atoms: Part III. Enhancement of the oxidation of carbon monoxide on platinum by ruthenium ad-atoms. *Journal of Electroanalytical Chemistry and Interfacial Electrochemistry*. 1975 Apr 25;60(3):275-83.
2. Liu R, Iddir H, Fan Q, Hou G, Bo A, Ley KL, Smotkin ES, Sung YE, Kim H, Thomas S, Wieckowski A. Potential-dependent infrared absorption spectroscopy of adsorbed CO and X-ray photoelectron spectroscopy of arc-melted single-phase Pt, PtRu, PtOs, PtRuOs, and Ru electrodes. *The Journal of Physical Chemistry B*. 2000 Apr 20;104(15):3518-31.
3. Goodenough JB, Manoharan R, Shukla AK, Ramesh KV. Intraalloy electron transfer and catalyst performance: a spectroscopic and electrochemical study. *Chemistry of Materials*. 1989 Jul 1;1(4):391-8.
4. Toda T, Igarashi H, Uchida H, Watanabe M. Enhancement of the electroreduction of oxygen on Pt alloys with Fe, Ni, and Co. *Journal of the Electrochemical Society*. 1999 Oct 1;146(10):3750.
5. Park KW, Choi JH, Kwon BK, Lee SA, Sung YE, Ha HY, Hong SA, Kim H, Wieckowski A. Chemical and electronic effects of Ni in Pt/Ni and Pt/Ru/Ni alloy nanoparticles in methanol electrooxidation. *The Journal of Physical Chemistry B*. 2002 Feb 28;106(8):1869-77.
6. Park KW, Choi JH, Sung YE. Structural, chemical, and electronic properties of Pt/Ni thin film electrodes for methanol electrooxidation. *The Journal of Physical Chemistry B*. 2003 Jun 19;107(24):5851-6.
7. Dalavi SB, Agarwal S, Deshpande P, Joshi K, Prasad BL. Disordered but efficient: Understanding the role of structure and composition of the Co–Pt alloy on the electrocatalytic methanol oxidation reaction. *The Journal of Physical Chemistry C*. 2021 Apr 5;125(14):7611-24.
8. Gurau B, Viswanathan R, Liu R, Lafrenz TJ, Ley KL, Smotkin ES, Reddington E, Sapienza A, Chan BC, Mallouk TE, Sarangapani S. Structural and electrochemical characterization of binary, ternary, and quaternary platinum alloy catalysts for methanol electro-oxidation. *The Journal of Physical Chemistry B*. 1998 Dec 3;102(49):9997-10003.

9. Park KW, Choi JH, Lee SA, Pak C, Chang H, Sung YE. PtRuRhNi nanoparticle electrocatalyst for methanol electrooxidation in direct methanol fuel cell. *Journal of Catalysis*. 2004 Jun 10;224(2):236-42.
10. Chen X, Jiang Y, Sun J, Jin C, Zhang Z. Highly active nanoporous Pt-based alloy as anode and cathode catalyst for direct methanol fuel cells. *Journal of Power Sources*. 2014 Dec 1;267:212-8.
11. Choi WC, Kim JD, Woo SI. Quaternary Pt-based electrocatalyst for methanol oxidation by combinatorial electrochemistry. *Catalysis Today*. 2002 Jun 5;74(3-4):235-40.
12. Salazar-Banda GR, Eguiluz KI, Pupo MM, Suffredini HB, Calegaro ML, Avaca LA. The influence of different co-catalysts in Pt-based ternary and quaternary electrocatalysts on the electro-oxidation of methanol and ethanol in acid media. *Journal of Electroanalytical Chemistry*. 2012 Mar 1;668:13-25.
13. Fu S, Zhu C, Du D, Lin Y. Enhanced electrocatalytic activities of PtCuCoNi three-dimensional nanoporous quaternary alloys for oxygen reduction and methanol oxidation reactions. *ACS applied materials & interfaces*. 2016 Mar 9;8(9):6110-6.
14. Chai GS, Yu JS. Highly efficient Pt–Ru–Co–W quaternary anode catalysts for methanol electrooxidation discovered by combinatorial analysis. *Journal of Materials Chemistry*. 2009 July 28;19(37):6842-8.
15. Yao C, Xu H, Li A, Li J, Pang F, Zhao P, He J, Yi W, Jiang Y, Huang L. Synthesis of PtCoNiRu/C nanoparticles by spray drying combined with reduction sintering for methanol electro-oxidation. *RSC advances*. 2020 Jan 22;10(6):3579-87.
16. Jiang J, Kucernak A. Electrodeposition of highly alloyed quaternary PtPdRuOs catalyst with highly ordered nanostructure. *Electrochemistry communications*. 2009 May 1;11(5):1005-8.
17. Jeon MK, Lee KR, Jeon HJ, McGinn PJ, Kang KH, Park GI. Quaternary Pt₂Ru₁Fe₁M₁/C (M= Ni, Mo, or W) catalysts for methanol electro-oxidation reaction. *Korean Journal of Chemical Engineering*. 2015 Feb;32:206-15.
18. Lin WF, Iwasita T, Vielstich W. Catalysis of CO electrooxidation at Pt, Ru, and PtRu alloy. An in situ FTIR study. *The Journal of Physical Chemistry B*. 1999 Apr 22;103(16):3250-7.
19. Lin WF, Iwasita T, Vielstich W. Catalysis of CO electrooxidation at Pt, Ru, and PtRu alloy. An in situ FTIR study. *The Journal of Physical Chemistry B*. 1999 Apr 22;103(16):3250-7.

Chapter-6

Final Thoughts and Future Prospects



This chapter includes a summary and concluding notes for the work detailed in this thesis, as well as the future scope of this study.

6.1 Summary of the Thesis:

Direct Methanol Fuel Cells (DMFCs) have received a lot of interest in recent years as promising technology for producing clean and efficient energy. DMFCs have a promising future since they cause significantly less harm to the environment. Methanol is utilized as a fuel in DMFC. The anode catalyst is an important component of DMFCs since it is involved in the oxidation of methanol, which produces electrons that can be used as an energy source.

In recent years, significant progress has been achieved in the development of anode catalysts for DMFCs. Pt is the most commonly utilized metal in DMFC due to its outstanding catalytic activity.[1] However, due to catalyst poisoning, commercialization of this catalyst is restricted. CO is an active intermediate formed in the methanol oxidation reaction, and the extremely stable Pt-CO complex adsorbs on the catalyst surface, lowering DMFC efficiency.[2,3] Many efforts have been made to improve the effectiveness of the catalyst. Despite this, identifying a commercially viable electro-catalyst material with consistent performance remains a significant issue, owing to our inadequate understanding of the specific MOR mechanism.

In this background, we chose to investigate the MOR in depth for the scope of the thesis. A standard cyclic voltammogram (CV) for MOR reveals two peaks, one in forward (I_f , anodic scan) and one in reverse scan (I_b , cathodic scan). It is also proposed that the peak current ratio (commonly referred to as I_f/I_b) is a good marker for evaluating electro-catalyst performance in MOR. It is generally perceived that the higher the I_f/I_b , the greater the CO tolerance and thus the better the electrode performance. However, this criterion has lot of ambiguities and there are different opinions about the origin of I_b and the species responsible for it.[4-11]

With this background, we investigated the MOR mechanism in depth using a simple cyclic voltammetry. The study included in this thesis is directed to determining the true poisoning species responsible for catalyst deactivation and proposing a mechanism based on it. Many previously unknown facts were discovered during the re-investigation of the cyclic voltammetric (CV) response of MOR in acidic medium utilizing Pt/C as electro-catalyst. Systematic CV study clearly indicated that the peak during the cathodic scan in CV for MOR is primarily due to CO electro-oxidation. According to the findings, the current response of this peak is not entirely responsible for adsorbed species.

After successfully investigating the MOR mechanism, we attempted to establish the criteria to measure the poisoning of the catalyst during MOR based on the understanding gained from this work and the previous knowledge accessible. We proposed a new criterion for addressing

CO surface adsorption by conducting a simple experiment based on the proposed mechanism. We also validated this criterion using readily available marketed catalysts. Finally, using experimental data and fundamental knowledge from CV analysis, we synthesized trimetallic catalysts with higher activity and stability for MOR when compared to comm. Pt/C. The synthesized catalysts were examined using UV, PXRD, and electron microscopy. After synthesizing a catalyst and analysing it using new criteria, we decided to take it a step further and shift our focus from trimetallic to quaternary alloys. Subsequently, we also synthesized and analysed quaternary alloys of Pt, Co, Ni, and Fe/Ru metals in various compositions for MOR. The extra metal was chosen for its bifunctional and electronic capabilities, which will boost the activity of the multi-metallic alloy. Further studies like long term stability, CO tolerance are still needed to be done on these samples.

6.2 Scope for future work:

Recently flexible devices catch lot of attention as an emerging field due to its used in wearable and portable devices.[12] Traditional energy sources, however, are stiff in shape and hefty in weight due to the materials and cell configuration currently used, making integration into flexible energy sources difficult. So, it is important to replace stiff material by conducting material to fit them in flexible devices. Significant advance has been made in this area which includes flexible lithium/sodium/zinc ion battery and flexible supercapacitors.[13-15] Among flexible batteries lithium ion battery is considered as an ideal storage device due to high energy density and long stability cycle. Despite of this advantage it suffers with many problems which hindered its commercialization. Because of its high energy density (4820 Wh /L, significantly more than LIBs), the DMFC is a typical and ideal model for these devices, and will serve as an exciting contender for the future flexible energy source. A flexible DMFC refers to a DMFC that is designed to be flexible or bendable, rather than rigid. This type of fuel cell could potentially have applications in wearable technology, portable devices, and other products where flexibility is important.

In general, flexible DMFCs are still a relatively new technology and research is ongoing to improve their performance and durability. The maximum power density of a flexible DMFC based on a quasi-solid potassium polyacrylate hydrogel electrolyte was recently reported to be 8.86 mW /cm². [16] However, the ability to make fuel cells that are flexible has the potential to open up new possibilities for their use in various applications. Several different materials have been explored as potential anode materials for flexible DMFCs.[17-20] We would like to use our catalyst to study flexible DMFC.

One of the challenges in developing flexible DMFCs is finding materials that are both electrically conductive and flexible. Researchers have been exploring various materials, including graphene, carbon nanotubes, and conducting polymers, as potential electrodes for flexible DMFCs.

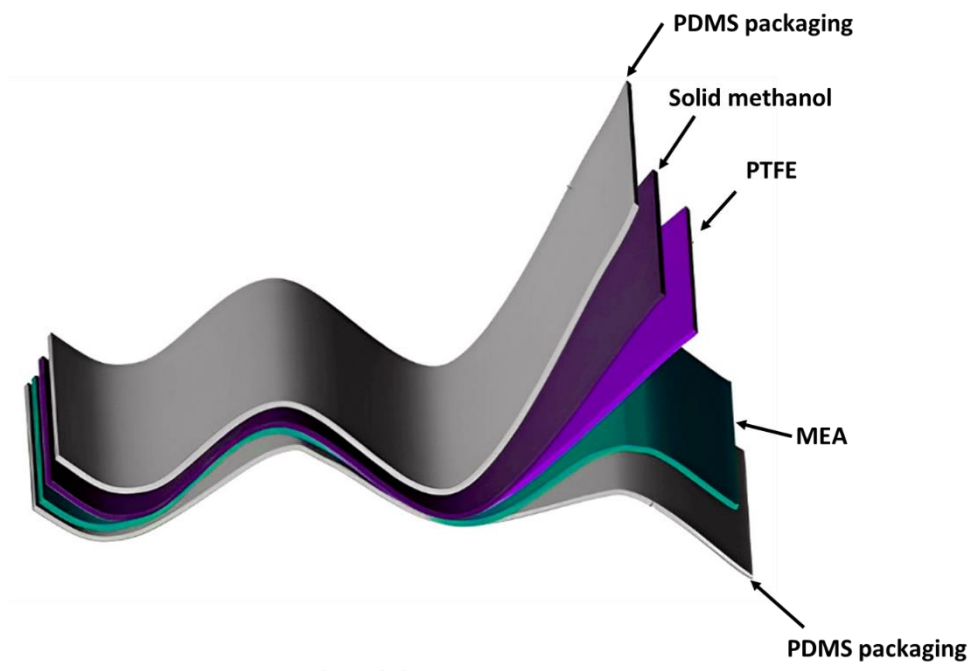
Another challenge is finding ways to make the membrane electrode assembly (MEA) flexible, which is the core component of a fuel cell. Researchers have been exploring various approaches to make the MEA flexible, including using polymer membranes, and developing new fabrication methods that allow for the creation of flexible MEAs. Flexible MEAs can be made with our prepared catalyst and they can be further utilized to fabricate flexible DMFC. We propose the following method, which has already been published, to create a flexible MEA. [19]

6.3. Methodology:

(a) Preparation of MEA:

The cathodic and anodic microporous layers (MPL) will be formed by coating carbon cloth with a well-dispersed slurry of Vulcan XC-72R and 20% wt poly(tetrafluoroethylene)(PTFE), with a total loading of Vulcan XC-72R of 2 mg/cm². The diffusion layer will be treated with heating in the air at 350 °C for 1 hour after being dried at 105 °C for 1 hour.

A specific amount of our Pt_x(CoNiM)_{100-x}/C sample need to be dissolved in 200 μL of a 1:1 ethanol:water mixture containing 10 % nafion solution to make the catalyst ink. The prepared catalyst ink can be drop casted on the previously mentioned MPL and vacuum treated for 1 hour at 105 °C. The alloy samples prepared as part of this thesis work could be used as an anode and a cathode. Finally, using the hot-pressing process, the nafion membrane can be sandwiched between these two layers for 3 minutes, resulting in the production of MEA. PDMS could be utilized as a packaging material in the development of a flexible fuel cell. Liquid methanol could pose challenges in the construction of flexible DMFCs. The problem of liquid methanol can be solved by solidifying it by reacting it with Polyacrylic acid and triethanolamine solution.[17] There are other factors to be considered before making DMFC flexible, and these need to be investigated in future.



Flexible DMFC

6.4. Reference:

1. Radhakrishnan T, Sandhyarani N. Three-dimensional assembly of electrocatalytic platinum nanostructures on reduced graphene oxide—an electrochemical approach for high performance catalyst for methanol oxidation. *International Journal of Hydrogen Energy*. 2017 Mar 9;42(10):7014-22.
2. Ahmadi R, Amini MK, Bennett JC. Pt–Co alloy nanoparticles synthesized on sulfur-modified carbon nanotubes as electrocatalysts for methanol electrooxidation reaction. *Journal of catalysis*. 2012 Aug 1;292:81-9.
3. Long NV, Yang Y, Thi CM, Van Minh N, Cao Y, Nogami M. The development of mixture, alloy, and core-shell nanocatalysts with nanomaterial supports for energy conversion in low-temperature fuel cells. *Nano Energy*. 2013 Sep 1;2(5):636-76.
4. Mancharan R, Goodenough JB. Methanol oxidation in acid on ordered NiTi. *Journal of Materials Chemistry*. 1992 Jan 1;2(8):875-87.
5. Perez-Martinez L, Machado De Los Toyos LM, Shibuya JJ, Cuesta A. Methanol dehydrogenation on Pt electrodes: active sites and role of adsorbed spectators revealed through time-resolved ATR-SEIRAS. *ACS Catalysis*. 2021 Oct 22;11(21):13483-95.
6. Chen YX, Miki A, Ye S, Sakai H, Osawa M. Formate, an active intermediate for direct oxidation of methanol on Pt electrode. *Journal of the American Chemical Society*. 2003 Apr 2;125(13):3680-1.
7. Chen DJ, Tong YJ. Irrelevance of carbon monoxide poisoning in the methanol oxidation reaction on a PtRu electrocatalyst. *Angewandte Chemie International Edition*. 2015 Aug 3;54(32):9394-8.
8. Ota KI, Nakagawa Y, Takahashi M. Reaction products of anodic oxidation of methanol in sulfuric acid solution. *Journal of electroanalytical chemistry and interfacial electrochemistry*. 1984 Nov 23;179(1-2):179-86.
9. Korzeniewski C, Childers CL. Formaldehyde yields from methanol electrochemical oxidation on platinum. *The Journal of Physical Chemistry B*. 1998 Jan 15;102(3):489-92.
10. Chung DY, Lee KJ, Sung YE. Methanol electro-oxidation on the Pt surface: revisiting the cyclic voltammetry interpretation. *The Journal of Physical Chemistry C*. 2016 May 5;120(17):9028-35.
11. Lai L, Yang G, Zhang Q, Yu H, Peng F. Essential analysis of cyclic voltammetry of methanol electrooxidation using the differential electrochemical mass spectrometry. *Journal of Power Sources*. 2021 Oct 15;509:230397.

12. Cai S, Han Z, Wang F, Zheng K, Cao Y, Ma Y, Feng X. Review on flexible photonics/electronics integrated devices and fabrication strategy. *Science China Information Sciences*. 2018 Jun; 61:1-27.
13. Kutbee AT, Ghoneim MT, Ahmad SM, Hussain MM. Free-form flexible lithium-ion microbattery. *IEEE Transactions on Nanotechnology*. 2016 Mar 2;15(3):402-8.
14. Kim YK, Shin KY. Dopamine-assisted chemical vapour deposition of polypyrrole on graphene for flexible supercapacitor. *Applied Surface Science*. 2021 May 1; 547:149141.
15. Li L, Liu W, Jiang K, Chen D, Qu F, Shen G. In-situ annealed Ti₃C₂T_x MXene based all-solid-state flexible Zn-Ion hybrid micro supercapacitor array with enhanced stability. *Nano-Micro Letters*. 2021 Dec; 13:1-1.
16. Li X, Chao T, Duan YE, Qu Y, Liu Y, Tan Q. High-performance, stable, and flexible direct methanol fuel cell based on a pre-swelling kalium polyacrylate gel electrolyte and single-atom cathode catalyst. *ACS Sustainable Chemistry & Engineering*. 2021 Oct 29;9(45):15138-46.
17. Ito T, Kimura K, Kunimatsu M. Characteristics of micro DMFCs array fabricated on flexible polymeric substrate. *Electrochemistry communications*. 2006 Jun 1;8(6):973-6.
18. Chen F, Sun Y, Li H, Li C. Review and development of anode electrocatalyst carriers for direct methanol fuel cell. *Energy Technology*. 2022 Jun;10(6):2101086.
19. Sun S, Zhao M, Wang Q, Xue S, Huang Q, Yu N, Wu Y. Flexible All-Solid-State Direct Methanol Fuel Cells with High Specific Power Density. *Small*. 2023 Jan 12:2205835.
20. Li X, Bu F, Zhang H, Zhao C. Facile synthesis of poly (arylene ether ketone) s containing flexible sulfoalkyl groups with enhanced oxidative stability for DMFCs. *International Journal of Hydrogen Energy*. 2020 Oct 16;45(51):27632-43.

ABSTRACT

Name of the Student: Pooja Shrikant Deshpande

Registration No.: 10CC17A26002

Faculty of Study: Chemical Sciences

Year of Submission: 2023

CSIR Lab: NCL, Pune

Name of the Supervisor: Dr. BLV Prasad

Title of the Thesis: "Development of electrocatalyst with better efficiency: Revisiting methanol oxidation process"

Direct Methanol Fuel Cells (DMFCs) have received a lot of interest in recent years as promising technology for producing clean and efficient energy. This thesis focused on the methanol oxidation reaction (MOR) that occurs at the anode of the DMFC. The anode catalyst is an important component of DMFCs. Generally, Pt is the most commonly used anode catalyst for DMFC, but due to catalyst poisoning, commercialization is restricted. The MOR process is characterized by two peaks, one in forward (I_f) and one in reverse (I_b). I_f/I_b is the most commonly used criteria to study catalyst poisoning. Significant progress has been made in terms of defining the MOR mechanism and clarifying the exact performance determining step, certain ambiguities still remain regarding the poisoning species and the criteria to judge poisoning, which we believe are impeding the systematic development of new catalysts. This evidently demonstrates the need to reconsider the MOR mechanism and criteria (I_f/I_b) that are regularly utilized for evaluating electrode performance in MOR. We investigated the MOR mechanism in depth using a simple yet sophisticated technique called cyclic voltammetry.

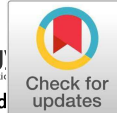
The research in this thesis aims to identify the real poisoning species responsible for catalyst deactivation and propose a mechanism based on it. Many previously unknown facts were discovered during the re-investigation of the cyclic voltammetric (CV) response of MOR. We attempted to design criteria to measure the poisoning of the catalyst during MOR based on the information acquired from this work and the previous knowledge available after successfully investigating the MOR process. We proposed a new criterion for addressing CO surface adsorption by conducting a simple experiment based on the proposed mechanism. We also validated this criterion using readily available market catalysts. Finally, using experimental data and fundamental knowledge from CV analysis, we synthesized catalysts with higher activity and stability for MOR when compared to comm. Pt/C. The synthesized catalysts were examined using UV, PXRD, and electron microscopy

List of publication (emanating from this thesis work)

1. Deshpande, P.S., Chaudhari, V.R. and Prasad, B.L., 2020. Mechanistic aspects of methanol electro-oxidation reaction through cyclic voltammetry: is it correct to blame carbon monoxide for catalyst poisoning? *Energy Technology*, 8(5), p.1900955.
2. Deshpande, P. and Prasad, B.L., 2023. Alloying with Mn Enhances the Activity and Durability of the CoPt Catalyst toward the Methanol Oxidation Reaction. *ACS Applied Materials & Interfaces*.
3. Deshpande, P.S. and Prasad, B. L. V., 2023. Establishing a new efficiency descriptor for MOR and its validation with commercially available catalysts. (Manuscript under preparation)

List of papers with abstract presented (oral or poster) at national or international conferences/seminars.

- 1) Science Day Conference, CSIR-National Chemical Laboratory, Pune, 2019, 2021. (Poster presented).
- 2) The Materials Research Society of India (MRSI) conference (oral presentation)
- 3) NCL-RF Annual Student's Conference, CSIR-National Chemical Laboratory, 2021 (delivered oral presentation)



Mechanistic Aspects of Methanol Electro-Oxidation Reaction through Cyclic Voltammetry: Is It Correct to Blame Carbon Monoxide for Catalyst Poisoning?

Pooja S. Deshpande, Vijay R. Chaudhari, and Bhagavatula L. V. Prasad*

Many previously unknown facts have been revealed by the reinvestigation of the cyclic voltammetric (CV) response of the methanol oxidation reaction (MOR) in acidic medium using Pt/C as the electrocatalyst. Systematic CV analysis clearly suggests that the peak during the cathodic scan in the CV of MOR belongs mainly to electro-oxidation of the carbon monoxide (CO) species, which is not truly adsorbed on the electrode surface and hence has less possibility to poison the electrode surface. Interestingly, an additional peak is observed in the anodic scan at higher scan rates and the results suggest that this peak is associated with surface-confined electrochemical processes related to the oxidative desorption of leftover CO. This clearly highlights the necessity to relook at the notion of correlating the ratio of the peak currents in the anodic versus cathodic directions to CO poisoning, which is routinely used for the evaluation of the electrode performance in MOR. Through simple but accurate CV experiments, this report clearly brings out the important criteria that should be looked into while evaluating the electrocatalyst performance in the MOR process.

1. Introduction

Improvement in direct methanol fuel cell (DMFC) efficiency is currently being pursued fervently due to the current energy concerns and the ensuing demand for enhanced electrocatalyst performance. This has led to massive efforts to find new electrocatalysts.^[1–5] Despite all this, the discovery of an electrocatalyst material which is commercially viable with consistent performance continues to be a great challenge, mainly due to our limited understanding of the exact methanol oxidation reaction (MOR) mechanism. We would like to add here that although noticeable advances have been made in terms of delineating the MOR mechanism and elucidating the exact performance determining step,^[6–17] certain ambiguities still remain and, we

believe, these are impeding the development of new catalysts in a systematic way.

Attempts to understand the MOR mechanism has been initiated a couple of decades ago. The first noticeable contributions came from Kunimatsu et al., who, through a combination of infrared (IR) spectroscopy and electrochemistry techniques demonstrated that CO is a major intermediate species during MOR.^[6–9] Later on, the research focus related to the MOR mechanism shifted to the determination of different intermediates through various combined electroanalytical and spectroscopic techniques. These investigations suggested that at initial MOR stages, formic acid, formaldehyde, acetic acid, methoxy, and CH_x species ($x = 0–3$) are formed as the intermediates in addition to CO₂.^[13,17–22] Nevertheless, over a period of time CO₂ gets liberated as the sole product of

MOR. Later on, Buschmann et al. using in situ secondary ion mass spectroscopy (SIMS)^[10] and simultaneously Willsau et al. using in situ differential electrochemical mass spectroscopy (DEMS)^[11] analyzed the MOR intermediates based on the number of electrons involved in the electrochemical conversion of intermediates to CO₂. Accordingly, Willsau et al. inferred that CO was not the intermediate and they deduced the actual intermediate to be CHO. However, it has been shown that CHO as an intermediate is quite active in nature and ultimately gets converted to CO with the aid of surface oxides present on the electrode surface.^[10,11] This conjecture is also supported by the detailed cyclic voltammetric (CV) investigations of Mancharan and Goodenough where they also concluded CO to be the intermediate.^[12] Apart from concluding the intermediate to be CO, Mancharan and Goodenough also proposed a criterion for evaluating the electrocatalyst performance in MOR as described later.^[12]

Figure 1 shows the standard CV routinely observed for MOR by all the researchers when platinum on carbon is used as a catalyst. Typically, it shows two peaks: one each in anodic (P_{a1}) and cathodic (P_{c1}) scans. Mancharan and Goodenough proposed that methanol is oxidized to CO during the anodic scan (P_{a1}) and part of this generated CO oxidizes to CO₂ at higher anodic potential (P_{a1}'). The remaining CO now gets adsorbed on the electrode surface which on scan reversal converts to CO₂ (P_{c1}). Based on this mechanism, they correlated the peak current at P_{c1} to the extent of adsorbed/unoxidized CO that is responsible for the decrease in performance of electrocatalyst, and termed it as “CO poisoning.”

P. S. Deshpande, Dr. V. R. Chaudhari, Dr. B. L. V. Prasad
Physical and Material Chemistry Division
National Chemical Laboratory (CSIR-NCL)
Dr. Homi Bhabha Road, Pune 411008, India
E-mail: pl.bhagavatula@ncl.res.in

P. S. Deshpande, Dr. B. L. V. Prasad
Academy of Science and Innovation Research (AcSIR)
Ghaziabad 201002, India

The ORCID identification number(s) for the author(s) of this article can be found under <https://doi.org/10.1002/ente.201900955>.

DOI: 10.1002/ente.201900955

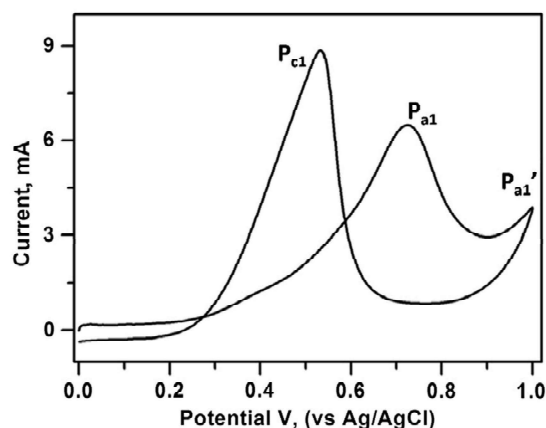


Figure 1. CV scan recorded using 20% Pt/C in 0.5 M H₂SO₄ and 1 M methanol solution. Scan rate: 50 mV s⁻¹.

Furthermore, they also proposed the peak current ratio $I_{[P_{a1}]} / I_{[P_{c1}]}$ routinely referred to as (I_f / I_b) as a marker for evaluating the performance of the electrocatalyst in MOR. They concluded that the higher the I_f / I_b , the greater would be the CO tolerance and, hence, the better the electrode performance.

Although the I_f / I_b ratio is the most generally accepted and majorly used marker test to date, attempts to re-evaluate the MOR mechanism gained momentum recently and new mechanisms and marker tests for MOR started appearing in the literature.^[13–16] Among them, the studies by Hofstead-Duffy et al., Zhao et al., and Chung et al. are the most important to consider for the current study.^[14–16] For example, Hofstead-Duffy et al. evaluated the MOR mechanism on Pt/C and PtRu/C using in situ surface-enhanced infrared absorption spectroscopy (SEIRAS) and proposed that electrochemical process associated with P_{a1} and P_{c1} are due to the same chemical species,^[14] i.e., both the peaks correspond to electro-oxidation of methanol and these are not related to any oxygenated carbon (formate, CO, CO₂, and so on) species. This proposal was further supported by Zhao et al. and Chung et al. through different experimental approaches. Zhao et al. started the CV measurements without methanol and then added methanol during the initial stages of the cathodic scan and as soon as they added methanol they observed the peak P_{c1} .^[15] Consequently, they surmised that as the potential scan direction is cathodic at the time of methanol addition, the possibility of methanol electro-oxidation to CO is negligible and hence the species contributing to the P_{c1} is not CO. They further claimed that P_{c1} is related to the oxidation of methanol and not to any oxygenated carbon species. At the same time, Chung et al., using combined CV and electrochemical impedance spectroscopy (EIS), also suggested that a similar process to be occurring at P_{c1} , that is, it resulted from the electro-oxidation of methanol alone.^[16]

However, these arguments have an issue. For example, Hofstead-Duffy et al. justified their claims by correlating the IR intensity changes for methanol between the potential region of P_{a1} , P_{c1} peaks in the MOR CV.^[14] But, it can be clearly seen from their results that the observed current for both the peaks in CV are comparable, whereas the corresponding IR intensities of the species claimed to be responsible for these two peaks are vastly different from each other. The claims by Zhao et al. and

Chung et al. that the process occurring at P_{c1} is the electro-oxidation of methanol and is not related to any oxygenated carbon species also have a similar problem. It may be noted that although they recorded the CV in the cathodic direction, they ignored the fact that the potential at which the scan was started would be sufficient enough to oxidize methanol.^[15,16]

Summarizing the aforementioned discussion, it can be easily observed that there is a great deal of ambiguity in the CV analysis for MOR and most of this is majorly associated with the process occurring at P_{c1} . Therefore, we believe that careful CV analysis and gaining of deeper insights about the electrochemical phenomenon associated with P_{c1} may help us to resolve the issue and would provide us a clear picture about the MOR interpretation. With this background, we aimed to understand 1) the electrochemical phenomenon associated with P_{c1} , 2) the nature and role of intermediates during MOR and their interaction with the electrocatalyst, and 3) the evaluation parameter for the MOR process. We chose commercial Pt on carbon (20% Pt/C) as an electrocatalyst material for these investigations, as it is the active and most studied material. Our investigations clearly demonstrate that CO is most electroactive intermediate being formed during MOR and is not completely in the adsorbed state. Rather most of it is in the solution phase. We believe that this better understanding of the MOR mechanism will help researchers to develop new catalyst materials with improved performance characteristics in a rational manner. We also wish to mention here that we use simple CV tools in our investigations, which highlights the fact that by designing and performing strategic CV experiments, deeper insights into the MOR mechanism could be attained.

2. Results and Discussion

Figure 1 shows the CV recorded using 20% Pt/C in 0.5 M H₂SO₄ and 1 M methanol, which matches well with most of the CVs reported for MOR in the literature.^[23]

As mentioned earlier, there is significant ambiguity in terms of the electrochemical processes occurring at P_{c1} . Therefore, we set out to gain deeper insights into this process and conducted a series of systematic CV experiments. First, we recorded the CV for the MOR using Pt/C at the extended anodic potential limit, as shown in Figure 2A.

In Figure 2A, the black curve corresponds to the CV profile where the potential was varied from 0 V to +1.0 V to 0 V. Similarly, the red curve corresponds to the CV profile where the potential was varied from 0 V to +1.6 V to 0 V. It can be seen from the inset of Figure 2A that with increase in the anodic potential limit, the position of the peak P_{c1} shifted toward the left, indicating that the separation between P_{a1} and P_{c1} peaks changed as the anodic potential limit is changed (inset of Figure 2A). Based on this, we precisely selected the potential value between P_{a1} and P_{c1} and used the same (0.5 V) as the starting potential to record the MOR CV in the cathodic scan direction (Figure 2B). The purpose behind this strategy is to completely avoid the electrochemical process associated with P_{a1} by starting the scan at a lower potential than the onset potential of P_{a1} , so that one can clearly emphasize whether P_{c1} is truly associated with P_{a1} or the processes occurring at these two potentials are independent of each other.

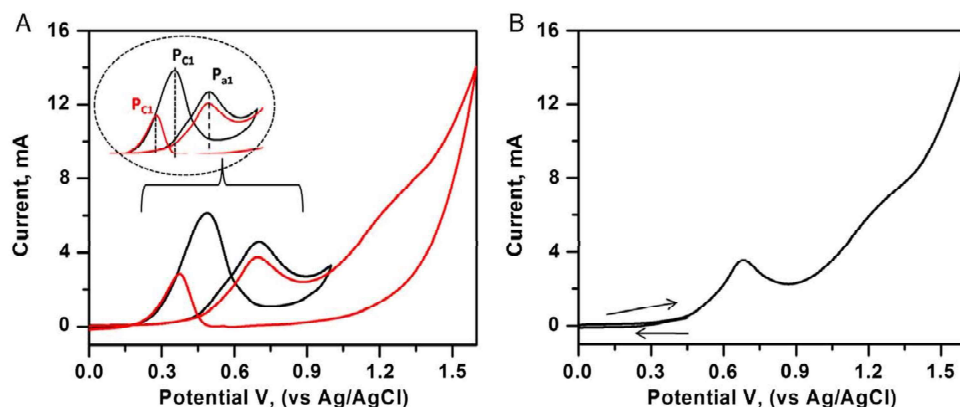


Figure 2. CV recorded using Pt/C in 0.5 M H₂SO₄ and 1 M methanol. A) Representative CVs recorded with end potential 1 V (black) and 1.6 V (red). The separation between the peaks increases as the anodic potential limit is changed (inset of part (A)). B) CV started in the negative scan direction with start potential 0.5 V. Scan rate: 50 mV s⁻¹.

From Figure 2B, it can be clearly seen that P_{c1} does not appear when the CV is recorded in the cathodic direction by starting the scan at ≈ 0.5 V. If P_{c1} belongs to methanol oxidation only, as suggested by Zhao et al., then it should have appeared irrespective of the potential at which this scan was started, as methanol was present in the system.^[14–16] Therefore, we believe that the appearance of P_{c1} in the experiments of Zhao et al. and Chung et al.^[15,16] during the first cathodic scan is due to the high potential at which they started the scan, where the oxidation of methanol was possible. This clearly proves that P_{a1} and P_{c1} are related to each other and that P_{c1} emerges only after methanol oxidation, forming the oxidized species. As expected in our experiment as well, P_{c1} does appear in successive cycles when the limiting potential is above the value where P_{a1} occurs (Figure S2B, the red curve, Supporting Information). To further support our hypothesis that the appearance of P_{c1} is due to the overpotential at which the scan was started, we recorded different sets of CVs for MOR in the cathodic direction by varying the starting potential in a systematic way. We started our experiments well below the onset potential of P_{a1} and slowly increased the starting potential to the potential range just above it (Figure 3).

From Figure 3, it can be clearly seen that P_{c1} is insignificant when the start potential is lower than the onset potential of P_{a1} . As expected, P_{c1} started appearing as the starting potential is closer to the value of P_{a1} and when we started the scan at a potential higher than P_{a1} , the intensity (current value) of P_{c1} gradually increased. One can also imagine another possibility that the Pt surface was already largely poisoned by methanol-generated CO. However, this possibility is discarded based on the in situ SEIRAS investigation, where no adsorbed CO was found within this potential region.^[14] Thus, our experiments clearly confirmed that P_{c1} does not belong to methanol oxidation. Rather, it is related to the new species formed when the starting potential is close to P_{a1} or higher.

As mentioned earlier, different intermediates of MOR have been traced out through different in situ techniques.^[10,11,13] However, it should be noted that most of these species would be either unstable or ultimately get converted to CO, or in few instances, their overall observed concentration in the system

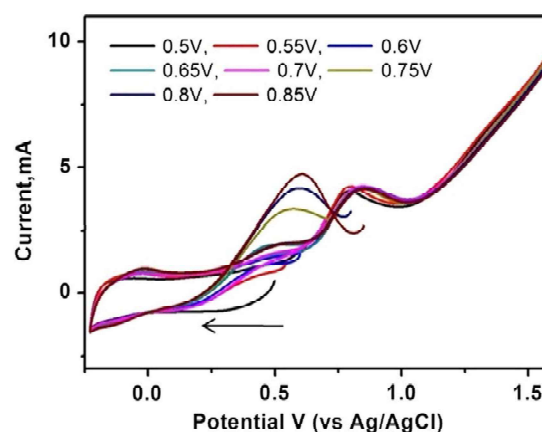


Figure 3. CV recorded using Pt/C in H₂SO₄ and methanol at different cathodic start potentials. The legend in the figure corresponds to the start potential. Scan rate: 50 mV s⁻¹.

would be very less.^[10] Examining the claims of different intermediates being formed and their observed concentrations and comparing them with the charges associated with P_{c1} , it is hard to believe that only these other intermediates and not CO would Faradically contribute to the total current observed for P_{c1} . Moreover, recent attempts of analyzing the MOR intermediates through highly sensitive in situ techniques also detected CO as major intermediates of MOR.^[13,14] All these facts strongly point to CO as the most probable electroactive intermediate; thus, we focused on the CO pathway only during this study for the electro-oxidation of methanol.^[12] Nonetheless, to unequivocally confirm that the species formed by methanol oxidation at potential close to or higher than P_{a1} is CO, we performed the following experiment. We first conducted the linear sweep voltammetry (0–1 V) experiment in methanol (experimental condition: 20% Pt/C in 0.5 M H₂SO₄ and 1 M methanol) and then transferred the same electrode into an electrochemical cell containing 0.5 M H₂SO₄ and recorded the CV (Figure S3, Supporting Information). As can be seen from Figure S3, Supporting Information, an anodic

peak at 0.56 V is observed in the first cycle, which is absent in subsequent cycles. Interestingly, the position and characteristics of the peak at 0.56 V matches with CO stripping and thus strongly suggesting that the intermediate being formed is CO.^[24–26]

Thus, this experiment and the aforementioned literature^[10–12] clearly confirm CO as an intermediate of MOR when the potential is at or above the potential of P_{a1} and the dependency of P_{c1} on P_{a1} suggest that P_{c1} is due to electro-oxidation of CO, although we cannot completely deny the contribution of other intermediates as well toward P_{c1} . After confirming that CO is indeed one of the species responsible for the peak observed at P_{c1} , we proceeded to evaluate its role as a catalyst poison as alluded to by Mancharan and Goodenough.^[12]

After ascertaining that CO poisoning has been linked to its adsorption on the catalyst, we contended that in the CV, it should show characteristics similar to that of surface adsorbed species.^[27] To check this, we recorded that the CVs for MOR at different scan rates (Figure 4A). Surprisingly, with increase in scan rate, an additional peak (termed as P_{a2} in Figure 4B) started developing at 0.5 V in the anodic segment (Figure 4B). This peak always invariably appeared after the first cycle (from the second cycle onward). Furthermore, the current at P_{a2} increases relative to the P_{c1} as we increase the scan rate (Figure S4, Supporting Information). Recently, Haram and co-workers also observed this peak in a fast scan voltammetry experiment using a Pt/carbon nanotubes (CNTs) microelectrode and attributed it to oxidative adsorption of CO on the electrode surface.^[28] Nevertheless, to identify the origin of this peak in our experiments, we first analyzed the variation of peak current (I_p) for P_{c1} and P_{a2} with respect to the scan rate.

In Figure 5A, it is clear that the current value (I_p) associated with P_{c1} varies linearly (linear fit with $R^2 = 0.99$) with respect to the square root of the scan rate ($v^{1/2}$). On the other hand, linear fitting of P_{c1} peak current against scan rate is poor (Figure S5A, Supporting Information).

This clearly points to the diffusion-controlled nature of the species responsible for this peak. In contrast, the current observed at P_{a2} showed good linear relation with respect to the scan rate (Figure 5B), which suggests adsorption-controlled behavior. The electrochemical nature of the species responsible for P_{c1} and P_{a2} was further confirmed by plotting the $\log(v)$ versus $\log(I_p)$ (Figure 5C,D). It is well established that for

diffusion-controlled processes, the slope is expected to be 0.5, whereas for adsorption-controlled process it would be 1.^[29,30] As can be seen, in the current case, the slopes are found to be 0.45 and 1.25 for processes associated with P_{c1} and P_{a2} , respectively, and are close to the expected values for diffusion and adsorption-controlled processes respectively. Thus, this analysis clearly suggests that the electro-oxidation of CO at P_{c1} is diffusion controlled, whereas the electrochemical process related to P_{a2} is adsorption controlled. To further support the diffusion-controlled behavior associated with P_{c1} , we recorded the CVs at different electrode rotation speeds. For this, we have started the CV at 0 V without electrode rotation and then began the electrode rotation when the potential reached 1 V, so that there would not be any interference of rotation as the P_{a1} peak emerged. We surmised that if the entire CO that gets generated is truly not surface confined then during the scan reversal, the P_{c1} peak current would decrease. Expectedly, the P_{c1} peak current systematically decreased with an increase in electrode rotation speed (Figure 6), which clearly confirmed that not all CO is surface confined and that there must be some contribution from the solution phase CO to this peak. To avoid confusion between solution-phase CO and methanol, we performed another experiment in which we started the CV at 0 V for MOR with electrode rotation so that the effect due to the interference of rotation on P_{a1} and P_{c1} was the same. The logic behind this experiment was that if both the peaks belong to the same chemical species, then the effect of rotation should be the same for both the peaks, i.e., the current ratio of these two peaks must be constant with respect to change in the rotation speed. Furthermore, the current should increase with the electrode rotation speed which is a characteristic features for the species present in the solution. However, the results clearly (Figure S6A,B, Supporting Information) suggested that although the peak current of P_{a1} decreased only slightly, the current for P_{c1} decreased significantly strongly indicating that P_{c1} is not associated with the solution phase species, i.e., methanol. A slight decrease in current for P_{a1} with respect to the rotation speed has been attributed to the adsorption characteristics of methanol during that potential region and this possibility can be ruled out for P_{c1} , due to the presence of the oxide layer. More importantly, this experiment unambiguously points out that the species responsible for P_{a1} and P_{c1} are distinct from each other.

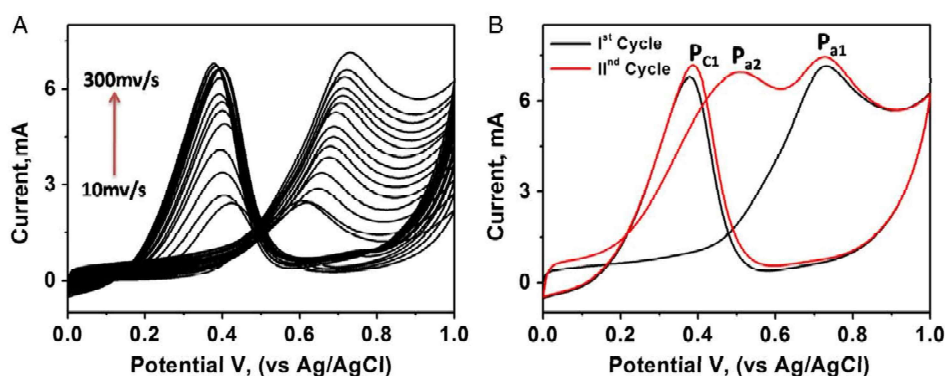


Figure 4. A) CV (first cycles) recorded using Pt/C in 0.5 M H_2SO_4 and 1 M methanol at different scan rates. B) First and second cycle recorded at scan rate: 300 mV s^{-1} . Scan rate-dependent comparison of second cycle is included in Figure S4, Supporting Information.

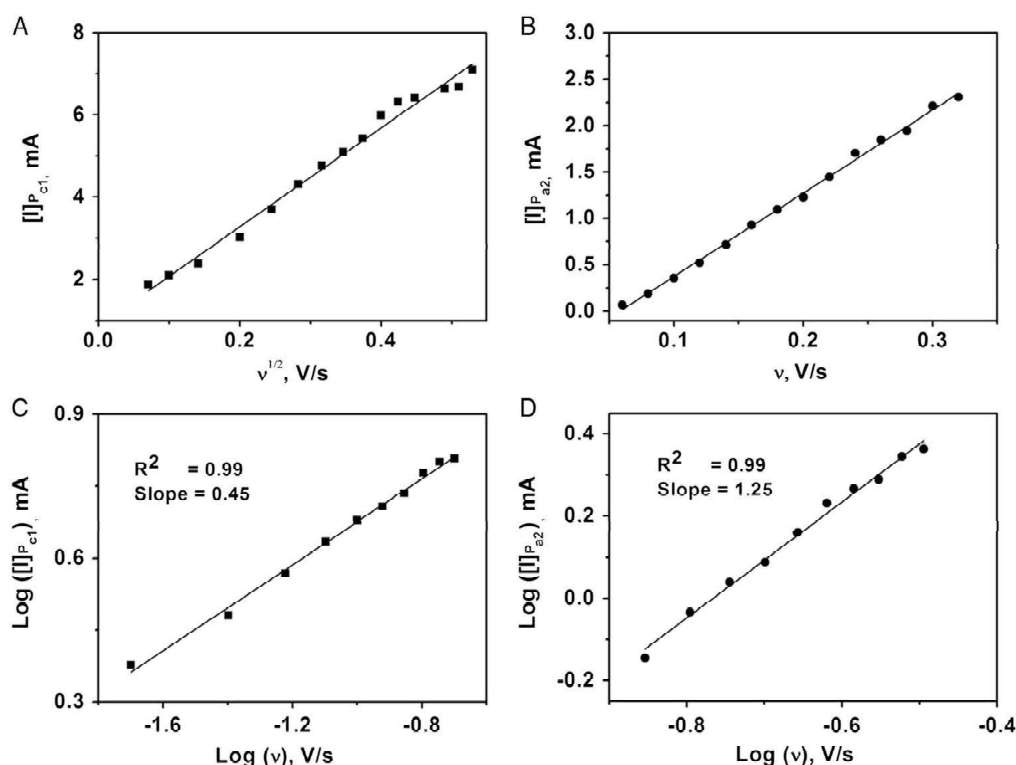


Figure 5. Variation of peak current (I_p) A) for P_{c1} with respect to the square root of the scan rate B) for P_{a2} with respect to the scan rate. Linear relationship between logarithm of peak current C) P_{c1} and D) P_{a2} and logarithm of scan rate.

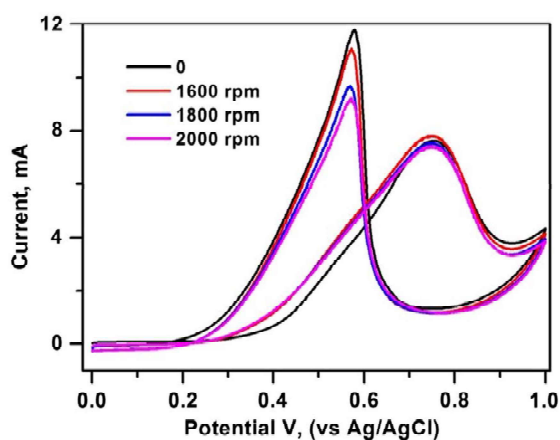


Figure 6. CVs recorded using Pt/C in 0.5 M H_2SO_4 and 1 M methanol at different electrode rotation speed. Scan rate: 50 mV s^{-1} .

Furthermore, we determined the oxide monolayer coverage on the electrode surface by recording the CVs at different anodic potential limits, which was deduced to be 1.4 V (see Figure S7A,B, Supporting Information, and refer to the corresponding discussion). Keeping this view, the CV was recorded in the presence of methanol, where it was clearly observed that the peak at P_{c1} appeared irrespective of the level of oxide coverage on the electrode surface (even beyond the 1.4 V anodic potential limit, Figure S7C, Supporting Information). This can be only

possible when the entire CO in the system is not completely in the adsorbed state.

Second, the MOR CVs recorded at different anodic potential limit and at higher scan rate (300 mV s^{-1}) (Figure S8, Supporting Information) clearly demonstrated the presence of a peak corresponding to the reduction of the surface oxide layer on the catalyst, which happens at a positive potential compared with the P_{c1} where CO oxidation occurs (Figure S8, Supporting Information, denoted by arrows). This undoubtedly confirms that the reduction of surface oxide on the catalyst happens first, followed by the CO oxidation process. Based on this, we propose the following processes to be occurring. The presence of surface oxide at extreme positive potential protects the electrode surface from complete CO coverage. Reductive cleaning of oxide from the electrode surface creates a fresh metallic surface,^[15] which is more active than the catalytic surface present at the beginning of the reaction. Such an active electrode surface oxidizes the solution phase CO at P_{c1} . As all the CO that is getting oxidized at P_{c1} is not surface confined, the I_f/I_b concept is not an appropriate one to evaluate the electrocatalyst performance in MOR. We believe that it can only be used to determine the Faradic efficiency of the MOR process. Another important point that needs to be clarified is the appearance of P_{a2} at faster scan rates. As mentioned previously, this peak has been observed only in a few reports and was attributed to the oxidative adsorption of CO. To verify this, we again recorded the CV for MOR (starting from 0 to 1 V a complete cycle), where the CV scan was stopped at the negative potential end followed by transferring the

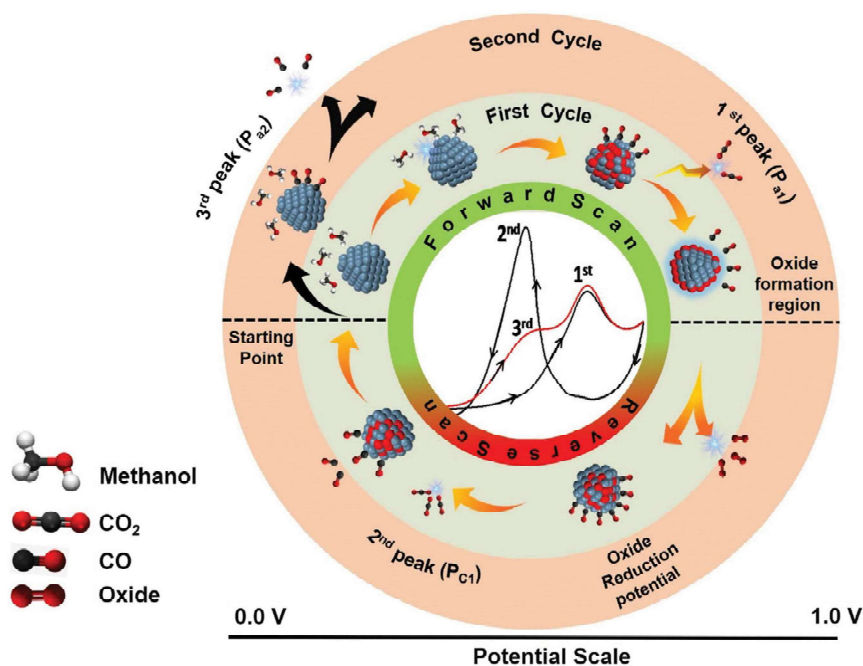


Figure 7. Schematic representation of the electrochemical MOR on Pt/C electrocatalyst in acidic medium.

electrode to a 0.5 M H_2SO_4 electrolyte and the recording of the CV (Figure S9, Supporting Information). Interestingly, we observed a peak whose characteristics and position matches with the CO stripping process, which clearly suggests that P_{a2} belongs to oxidative desorption of adsorbed CO and not to the adsorption of CO, as mentioned by Haram and co-workers.^[28]

Based on all the aforementioned systematic studies, we finally propose the following as the most plausible MOR mechanism (Figure 7).

As we start the CV from 0 V, during the first anodic scan methanol oxidizes to CO at P_{c1} part of which gets oxidized to CO_2 at P_{a1} . The majority of the remnant unoxidized CO stays in the solution phase, whereas a small part resides adsorbed on the electrode surface. This adsorbed CO, along with the CO present in the solution, oxidizes at P_{c1} on scan reversal (cathodic scan). However, at higher scan rates, as the kinetics of catalyst surface oxide reduction is slower, it impedes the extent of CO oxidation at P_{c1} and, hence, restricts complete oxidation of CO. This left over CO gets reductively adsorbed on the electrode surface,^[24–26] which ultimately oxidatively desorbs at P_{a2} . With increase in scan rates, the proportion of leftover CO increases due to sluggish catalyst surface oxide reduction kinetics. This leads to an increase in the CO concentration in the system and, hence, the current for P_{a2} increases at faster scan rates. In fact, the results in few recent reports also hint at the presence of leftover CO.^[13,14] Although the presence of this leftover CO was not discussed clearly in those reports, our results are successful in explaining its presence.

3. Conclusion

The exact mechanism of electrochemical MOR in the acidic medium using Pt/C was reinvestigated through a systematic

CV technique. The origins of the reverse peak in the cathodic direction (denoted as P_{c1} in this report) was identified, through selection of the appropriate starting potential and scan direction, and it was concluded that the major contribution is from the electro-oxidation of CO. It was clearly established that the CO formed in the methanol oxidation process followed diffusion-controlled behavior and, hence, it is not completely responsible for electrode poisoning through adsorption. Therefore, the concept of I_f/I_b is not appropriate to evaluate the electrocatalyst performance in MOR. Rather, it can be used to determine the Faradic efficiency of the MOR process. Furthermore, the origin of an additional peak in the successive anodic cycle has been unveiled and was demonstrated to be associated with the oxidative desorption of leftover CO and not due to the previously reported oxidative adsorption of CO.

4. Experimental Section

CV experiments were performed using the CHI660B potentiostat in a three-electrode system. The working electrode was prepared by depositing the electrocatalyst material on a glassy carbon (3 mm diameter) disc. Electrocatalyst ink was prepared by dispersing 10 mg of 20% Pt/C (Johnson Matthey, Batch#108X029) in 1 mL of a 1:1 water:ethanol mixture containing 0.5% Nafion through sonication, drop-casted on a glassy carbon electrode, and allowed to dry at room temperature. Ag/AgCl (3 M KCl) and Pt mesh were used as reference and counter electrodes, respectively. H_2SO_4 (0.5 M) was used as an electrolytic medium and MOR was performed using 1 M methanol concentration, unless and until mentioned otherwise. During the electrochemical measurements, inert atmosphere was maintained by bubbling nitrogen gas and also jacketed during measurement. 20% Pt/C was first characterized by recording CV in 0.5 M H_2SO_4 and also by performing X-ray powder diffraction analysis (Figure S1, Supporting information). For MOR, electrode was stabilized by recording the repetitive CVs (mostly ≈ 20 cycles) until a stable voltammogram was obtained and then further data were collected.

A few experiments were also performed using rotating disc electrodes. For this purpose, a 2 mm-diameter glassy carbon was used to deposit the electrocatalyst material.

CO stripping experiments were performed in CO-saturated 0.5 M H₂SO₄ solution. CO gas (purity 99%) was bubbled for 15 min and the electrode potential held at -0.2 V for 5 min. Stripping was done in nitrogen-saturated 0.5 M H₂SO₄ solution.

Supporting Information

Supporting Information is available from the Wiley Online Library or from the author.

Acknowledgements

P.S.D. thanks DST-INSPIRE for Junior Research Fellowship. V.R.C. thanks DST, New Delhi for financial support. The authors thank Dr. Kumar Vanka for carefully reading the manuscript and for useful discussions.

Conflict of Interest

The authors declare no conflict of interest.

Keywords

carbon monoxide, cyclic voltammetry, electrocatalysts, electrode poisoning, methanol oxidation

Received: August 9, 2019

Revised: December 10, 2019

Published online: January 30, 2020

- [1] M. Mansor, S. N. Timmiati, K. L. Lim, W. Y. Wong, S. K. Kamarudin, N. H. N. Kamarudin, *Int. J. Hydrogen Energy* **2019**, *44*, 14744.
- [2] Y. Kin, K. Saito, H. Oda, T. Ando, K. Nakagawa, *Catal. Lett.* **2019**, *149*, 1.
- [3] P. Sridhar, S. D. Bhat, A. K. Sahu, *Electrochemistry* **2017**, *14*, 102.
- [4] N. Kakati, J. Maiti, S. H. Lee, S. H. Jee, B. Viswanathan, Y. S. Yoon, *Chem. Soc. Rev.* **2014**, *114*, 12397.
- [5] S. Sankar, G. M. Anilkumar, T. Tamaki, T. Yamaguchi, *ACS Appl. Energy Mater.* **2018**, *1*, 4140.
- [6] B. Beden, C. Lamy, A. Bewick, K. Kunimatsu, *J. Electroanal. Chem.* **1981**, *121*, 343.
- [7] K. Kunimatsu, *J. Electroanal. Chem.* **1982**, *140*, 205.
- [8] K. Kunimatsu, *J. Electroanal. Chem.* **1983**, *145*, 219.
- [9] K. Kunimatsu, *J. Electron Spectrosc. Relat. Phenom.* **1983**, *30*, 215.
- [10] H. W. Buschmann, S. Wilhelm, W. Vielstich, *Electrochim. Acta* **1986**, *31*, 939.
- [11] J. Willsau, O. Wolter, J. Heitbaum, *J. Electroanal. Chem.* **1985**, *185*, 163.
- [12] R. Mancharan, J. B. Goodenough, *J. Mater. Chem.* **1992**, *2*, 875.
- [13] Y. X. Chen, A. Miki, S. Ye, H. Sakai, M. Osawa, *J. Am. Chem. Soc.* **2003**, *125*, 3680.
- [14] A. M. Hofstead-Duffy, D. J. Chen, S. G. Sun, Y. J. Tong, *J. Mater. Chem.* **2012**, *22*, 5205.
- [15] Y. Zhao, X. Li, J. M. Schechter, Y. Yang, *RSC Adv.* **2016**, *6*, 5384.
- [16] D. Y. Chung, K. J. Lee, Y. E. Sung, *J. Phys. Chem. C* **2016**, *120*, 9028.
- [17] D. J. Chen, Y. J. Tong, *Angew. Chem. Int. Ed.* **2015**, *54*, 9394.
- [18] K. I. Ota, Y. Nakagawa, M. Takahashi, *J. Electroanal. Chem.* **1984**, *179*, 179.
- [19] C. Korzeniewski, C. L. Childers, *J. Phys. Chem. B* **1998**, *102*, 489.
- [20] T. Iwasita, *J. Electroanal. Chem.* **1986**, *201*, 403.
- [21] A. V. Miller, V. V. Kaichev, I. P. Prosvirin, V. I. Bukhtiyarov, *J. Phys. Chem. C* **2013**, *117*, 8189.
- [22] J. Wang, R. I. Masel, *J. Am. Chem. Soc.* **1991**, *113*, 5850.
- [23] M. P. Hogarth, G. A. Hards, *Platinum Metals Rev.* **1996**, *40*, 150.
- [24] P. Ochal, J. L. G. de la Fuente, M. Tsytkin, F. Seland, S. Sunde, N. Muthuswamy, M. Ronning, D. Chen, S. Garcia, S. Alayoglu, *J. Electroanal. Chem.* **2011**, *655*, 140.
- [25] A. D. Pozio, M. De Francesco, A. Cernri, F. Cardellini, L. Giorgi, *J. Power Sources* **2002**, *105*, 13.
- [26] M. K. Jeon, H. Daimon, K. R. Lee, A. Nakahara, S. I. Woo, *Electrochem. Commun.* **2007**, *9*, 2692.
- [27] A. J. Bard, L. R. Faulkner, *Electrochemical Methods: Fundamental and Applications*, Vol. 2, John Wiley & Sons, New York **2001**, p. 408.
- [28] V. S. Joshi, D. C. Poudyal, A. K. Satpati, K. R. Patil, S. K. Haram, *Electrochim. Acta* **2018**, *286*, 287.
- [29] J. I. Gowda, S. T. Nandibewoor, *Asian J. Pharm. Sci.* **2014**, *9*, 42.
- [30] D. K. Gosser, *Cyclic Voltammetry Simulation and Analysis of Reaction Mechanisms*, Vol. 43, VCH, New York **1993**, p. 154.

Alloying with Mn Enhances the Activity and Durability of the CoPt Catalyst toward the Methanol Oxidation Reaction

Pooja Deshpande and Bhagavatula L. V. Prasad*



Cite This: <https://doi.org/10.1021/acsami.3c01140>



Read Online

ACCESS |



Metrics & More



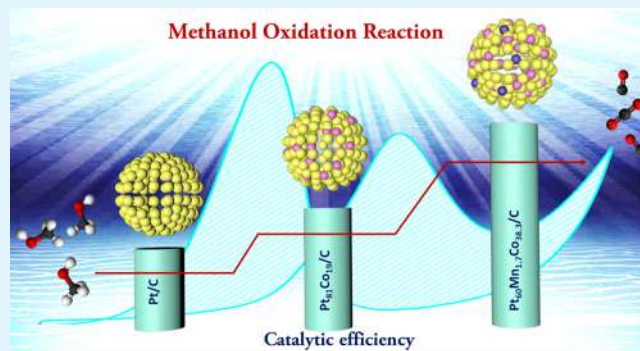
Article Recommendations



Supporting Information

ABSTRACT: To improve the catalytic performance and durability of Pt catalysts used for the methanol oxidation reaction (MOR) in direct methanol fuel cells (DMFCs), alloying of Pt with other transition metals such as Ru, Co, Ni, and Fe is considered an effective approach. Despite the significant progress made in the preparation of bimetallic alloys and their utilization for MOR, improving the activity and durability of the catalysts to make them commercially viable remains a stiff challenge. In this work, trimetallic $\text{Pt}_{100-x}(\text{MnCo})_x$ ($16 < x < 41$) catalysts were successfully synthesized via borohydride reduction followed by hydrothermal treatment at 150 °C. The electrocatalytic performance of the synthesized trimetallic $\text{Pt}_{100-x}(\text{MnCo})_x$ ($16 < x < 41$) catalysts toward MOR was studied using cyclic voltammetry and chronoamperometry. The results affirm that all $\text{Pt}_{100-x}(\text{MnCo})_x$ ($16 < x < 41$) alloys have superior MOR activity and durability as compared to bimetallic PtCo alloys and commercially available Pt/C (comm. Pt/C) catalysts. Among all the compositions studied, the $\text{Pt}_{60}\text{Mn}_{1.7}\text{Co}_{38.3}/\text{C}$ catalyst exhibited superior mass activity (1.3 and 1.9 times higher than those of $\text{Pt}_{81}\text{Co}_{19}/\text{C}$ and comm. Pt/C, respectively) toward MOR. Furthermore, all the newly synthesized $\text{Pt}_{100-x}(\text{MnCo})_x/\text{C}$ ($16 < x < 41$) catalysts showed better CO tolerance when compared with comm. Pt/C. This improved performance of the $\text{Pt}_{100-x}(\text{MnCo})_x/\text{C}$ ($16 < x < 41$) catalyst can be attributed to the synergistic effect of Co and Mn on the Pt lattice.

KEYWORDS: electrocatalysis, trimetallic alloy catalysts, direct methanol fuel cells, methanol oxidation reaction (MOR), CO tolerance



1. INTRODUCTION

Direct methanol fuel cells (DMFCs) have long been considered an attractive alternate power source for a large number of energy applications due to their high energy density, high efficiency, and low operating temperature. DMFCs are also much safer to operate because they deal with liquid fuel (methanol).^{1–3} The methanol oxidation reaction (MOR) at the anode and the oxygen reduction reaction (ORR) at the cathode are the main processes that determine the performance of DMFCs. Out of these, MOR is considered more important and determines the overall efficiency of DMFC technology. It is well known that Pt is the most effective catalyst for MOR.⁴ However, key obstacles like sluggish kinetics, high manufacturing cost (mainly due to the expensive Pt-based catalyst), and the poisoning of the Pt catalyst by CO make the commercialization of DMFCs a difficult task.^{5–10} Therefore, the search for an alternative Pt-based catalyst that circumvents the above issues is one of the most pressing research problems.

Alloys of Pt with other transition metals such as Ru, Co, Ni, and Fe are known to enhance the activity and durability of the electrocatalyst.¹¹ Thus, Pt-based alloys such as PtRu,¹² PtNi,¹³ PtAu,¹⁴ PtPd,¹⁵ and PtCo¹⁶ have attracted widespread

attention in recent years. Among the various Pt-based alloys, PtCo bimetallic alloys have been the most promising catalysts for MOR.^{17,18} Despite great progress made in the development of bimetallic alloys as MOR catalysts, a material that displays better activity and durability than commercial Pt-based catalysts is still elusive. Recently, a few reports have claimed that the addition of a small quantity of another metal to the bimetallic system can enhance the durability of the Pt-based bimetallic catalyst, making it better tolerant to CO poisoning.^{19–25} In addition, a ternary Pt-based alloy is likely to show better activity than a single or bimetallic alloy due to change in the electronic and structural characteristics of Pt.²⁶ Therefore, it is expected that trimetallic alloys of the variety PtMCo (where M is any transition metal) could further enhance durability as well as display better electrocatalytic performance. Among the transition metals, Mn is an abundant and

Received: January 25, 2023

Accepted: May 10, 2023

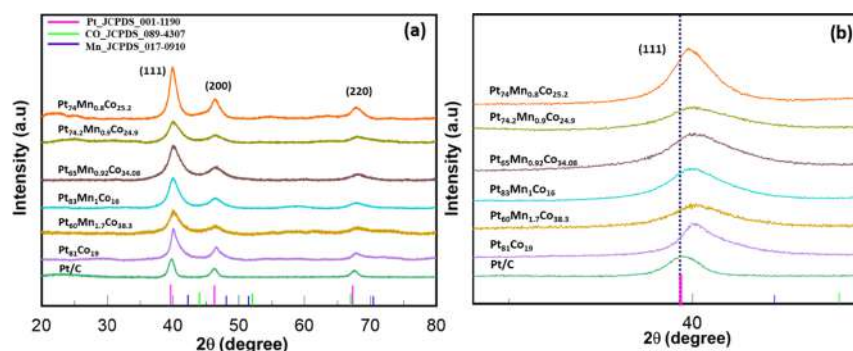


Figure 1. (a) XRD patterns for Pt_{100-x}(MnCo)_x (16 < x < 41) alloys. (b) Zoomed-in image of the peak (111).

inexpensive metal that shows variable oxidation states and therefore could be a good electrocatalyst.^{27–29} Interestingly, while a few investigations show that Mn has a beneficial influence on the electrocatalytic activity of Pt,^{30–33} the impact of Mn doping in PtCo catalysts and their efficiency for MOR is scarcely studied, and that too largely for ORR.^{34–38} Thus, to the best of our knowledge, the effect of trace quantities of Mn on the catalytic activity of the PtCo alloy toward MOR has not been evaluated. The fact that PtCo catalysts are known to perform better as MOR catalysts inspired us to carry out a systematic investigation on the possibility of doping Mn into them and testing their catalytic efficiency for MOR.

Accordingly, herein we report the synthesis of PtCo alloys with a small amount of Mn (Pt_{100-x}(MnCo)_x) (16 < x < 41) and the effectiveness of trimetallic PtMnCo alloys as a catalyst for MOR. The comparative performance of these new PtMnCo catalysts vis-a-vis the bimetallic PtCo alloy and commercially available Pt/C (comm. Pt/C) is also presented.

2. EXPERIMENTAL SECTION

For the synthesis, metal chloride salts like platinum(II) chloride, manganese(II) chloride tetrahydrate, and cobalt(II) chloride hexahydrate were used as metal precursors. All the metal salts were purchased from Sigma-Aldrich and other chemicals like methanol, ethanol, sodium bicarbonate, and NaOH were procured from local agencies. Commercial Pt/C (Comm. Pt/C) with 20 wt % Pt was purchased from Alfa Aesar. All the chemicals were of analytical grade and were used without further purification.

2.1. Synthesis of Nanoparticles. Pt_{100-x}(MnCo)_x (16 < x < 41) alloys were prepared via borohydride reduction followed by 3 h of hydrothermal treatment at 150 °C.³⁹ For the synthesis, the metal precursors were dispersed in a mixture of water and ethanol (20 mL of water and 10 mL of ethanol) in a Teflon bottle. The mixture was stirred for 10 min to ensure complete solubilization of the metal precursor. After complete solubility of the metal precursor, a 5 M NaOH (10 mL) solution was slowly added to the above mixture. As soon as 5 M NaOH solution was added, the color of the mixture changed from pale yellow to black, which shows the formation of metal oxide/hydroxide. A solution of 0.01 g of sodium borohydride in 30 mL of water was used as a reducing agent and was added slowly, drop by drop, using a syringe to the above black-colored mixture. The mixture was kept for vigorous stirring for another 10 min. The Teflon bottle was then placed in a stainless-steel autoclave and sealed tightly. Hydrothermal treatment was performed by keeping the autoclave in an oven at 150 °C for 3 h. After 3 h the autoclave was allowed to cool to room temperature (RT), and the resultant mixture was then treated with a 1 M HCl solution until the pH became acidic. The resultant mixture was magnetic and was separated with the help of a magnet. The separated sample was washed with an excess of water and ethanol, followed by drying at RT.³⁹

2.2. Characterizations of Pt_x(MnCo)_{1-x} Nanoparticles. The synthesized PtMnCo alloys were characterized using different techniques like X-ray diffraction (XRD), high-resolution transmission electron microscopy (HR-TEM), and the inductively coupled microwave plasma atomic emission spectroscopy (ICP-AES) technique. The alloy formation and structural characteristics were primarily tested and concluded by XRD analysis using Cu Kα (1.5418 Å) as a radiation source. XRD analysis was performed on an X'pert Pro model PANalytical diffractometer from Philips PANalytical instruments. For the operation of XRD instrument, the voltage and current were maintained at 40 kV and 30 mA, respectively. The samples for XRD were prepared on a glass slide using ground powder. The samples were scanned in a 2θ range from 10° to 80° with a scan rate of 0.3° per minute. The average crystal size and lattice parameter were calculated using full width half maxima (FWHM) and the angular position of the Pt (111) peak.

Elemental composition was determined using an Agilent 4200 model ICP-AESi instrument. For this analysis, the sample was prepared by dissolving a fixed milligram of the alloy in a minimum quantity of aqua regia and making up the volume to 100 mL.

The size, morphology, and chemical nature of the sample were studied using HR-TEM (JEM-F200, JEOL, operated at 300 kV). The HR-TEM sample was prepared by drop casting a solution of the ultrasonically dispersed catalyst in ethanol on a copper TEM grid (200 mesh) followed by the evaporation of ethanol at RT.

2.3. Electrochemical Measurements. Electrochemical measurements were performed on a conventional three electrode, CH Instruments 660B electrochemical workstation. Pt wire and Ag/AgCl electrodes were used as counter and reference electrodes, respectively. The electrochemical activity of the catalyst toward MOR was measured by drop casting electrocatalyst material ink on a glassy carbon electrode, which acted as a working electrode. For the preparation of catalyst ink, the prepared Pt_{100-x}(MnCo)_x (16 < x < 41) alloy samples were loaded on Vulcan XC-72 carbon first, keeping a 20 wt % loading of the respective sample. These samples will be referred as Pt_{100-x}(MnCo)_x/C (16 < x < 41) in the rest of the paper. For all electrochemical studies, we used 20% loaded samples. In a typical procedure for loading, the catalyst and Vulcan XC-72 carbon ratio were taken as (1:4), such as 4 mg of Pt_{100-x}(MnCo)_x (16 < x < 41) nanoparticles (NPs) and 16 mg of Vulcan XC-72 carbon, and were dispersed separately in 10 mL of ethanol followed by ultrasonication for 30 min. Subsequently, the sample dispersion was added to this carbon dispersion and was stirred for approximately 15 h. After stirring, it was subjected to centrifugation followed by acetone wash and ambient condition drying. TGA analysis for two samples was performed to crosscheck the loading of the catalyst on the carbon support (Figure S1). Finally, for the preparation of the working electrode, electrocatalyst ink was prepared by dispersing 2 mg of Pt_{100-x}(MnCo)_x in 200 μL of a 1:1 ethanol/water mixture containing 5% Nafion solution. From this dispersion, 4 μL was drop-cast on a glassy carbon electrode and dried at RT. A similar procedure was followed for the preparation of the comm. Pt/C (20 wt % Pt) working electrode.

The cyclic voltammetry (CV) measurements were conducted to investigate the electrochemical behavior of different catalysts. The electrochemical active surface area (ECSA) of a Pt-based alloy has been determined by recording CV in $N_2(g)$ -saturated aqueous 0.5 M H_2SO_4 with a scan rate of 50 mV s^{-1} in the potential region 1.4 to -0.23 V vs Ag/AgCl. The first potential region from -0.23 to 0.1 V indicates the adsorption/desorption region of hydrogen on the Pt surface. The electrochemical surface area (m^2/g) was calculated using the monolayer charge on platinum ($210 \mu\text{C}/\text{cm}^2$), loading of platinum, and the integrated charge in the hydrogen adsorption and desorption region. To find out the activity of the catalyst toward MOR, experiments were conducted in a $N_2(g)$ -saturated 0.5 M H_2SO_4 and 1 M CH_3OH aqueous solution, and CVs were recorded at a scan rate of 50 mV s^{-1} in a potential range from 0.0 to 1.0 V vs Ag/AgCl. Chronoamperometry (CA) curves were recorded to check the stability of electrodes for 8000 s. The CO stripping experiment was carried out in CO-saturated 0.5 M H_2SO_4 solution. CO gas (purity 99%) was bubbled for around 20 min to saturate the 0.5 M H_2SO_4 solution. To adsorb CO on the electrode surface, electrode potential was held at -0.2 V for 10 min. Stripping was done at 50 mV s^{-1} .

3. RESULTS AND DISCUSSION

3.1. Crystal Structure and Microstructural Analysis.

The PXRD patterns of $Pt_{100-x}(MnCo)_x$ ($16 < x < 41$) alloys

Table 1. Lattice Constant, Crystal Size, and % Strain for $Pt_{100-x}(MnCo)_x$ ($16 < x < 41$) Alloys Calculated from Corresponding XRD Patterns

sample	lattice constant (<i>a</i>) (Å)	crystal size (nm)	% strain
$Pt_{81}Co_{19}$	3.9059	4.92 ± 0.50	-0.517
$Pt_{60}Mn_{1.7}Co_{38.3}$	3.8785	3.73 ± 0.16	-1.227
$Pt_{83}Mn_1Co_{16}$	3.8996	4.3 ± 0.02	-0.679
$Pt_{65}Mn_{0.92}Co_{34.08}$	3.8954	3.67 ± 0.24	-0.788
$P_{74.2}Mn_{0.9}Co_{24.9}$	3.9047	4.07 ± 0.19	-0.548
$Pt_{74}Mn_{0.8}Co_{25.2}$	3.9146	4.76 ± 0.90	-0.294

are presented in Figure 1. It should be noted that the composition of the alloys as mentioned in Figure 1 has been determined using ICP-AES analysis (Table S1). Along with the compositions that were investigated in detail further in this study, a trimetallic alloy with excess Mn content was also prepared. More detail about this sample is given in the Supporting Information (SI, Figure S2). However, as it did not show any enhanced catalytic activity toward MOR, we did not peruse this sample further. In the PXRD patterns of all other compositions, the diffraction peaks located at 39.8° , 46.4° , and 67.8° for Pt are ascribed to the Pt (111), (200), and (220) facets, respectively. Compared to the standard diffraction peaks of Pt (JCPDS 001_1190), the positions of all the peaks in PtMnCo alloys were found to be slightly shifted to higher 2θ values (Figure 1). The lattice parameter “*a*” for $Pt_{81}Co_{19}$, $Pt_{60}Mn_{1.7}Co_{38.3}$, $Pt_{83}Mn_1Co_{16}$, $Pt_{65}Mn_{0.92}Co_{34.08}$, $P_{74.2}Mn_{0.9}Co_{24.9}$, and $Pt_{74}Mn_{0.8}Co_{25.2}$ were determined to be 3.9059, 3.8785, 3.8996, 3.8954, 3.9047, and 3.9146 Å, which shows discernible reduction in the lattice parameter with respect to the values for comm. Pt/C ($a = 3.9261 \text{ Å}$)⁴⁰ or that of the $Pt_{81}Co_{19}$ sample prepared as part of this study. The average crystallite sizes as determined from the Scherrer formula using the full width at half maximum of the (111) plane were found in the range of 3.5 to 5.0 nm (Table 1).

TEM micrographs for $Pt_{100-x}(MnCo)_x$ ($16 < x < 41$) alloys are presented in Figure 2a–c,g,h. These images suggest that all prepared materials have a nearly spherical morphology with individual particle sizes in the range of 5 to 8 nm, confirming

that the synthesized materials can be classified as NPs. The average TEM particle sizes (Figure 2d–f,i,j) turned out to be 5.0 ± 1.1 , 8.2 ± 2.1 , 5.5 ± 1.3 , 6.7 ± 1.7 , and $7.3 \pm 1.62 \text{ nm}$ for $Pt_{60}Mn_{1.7}Co_{38.3}$, $Pt_{83}Mn_1Co_{16}$, $Pt_{65}Mn_{0.92}Co_{34.08}$, $P_{74.2}Mn_{0.9}Co_{24.9}$, and $Pt_{74}Mn_{0.8}Co_{25.2}$ NPs, respectively. In comparison, the average TEM particle size for the $Pt_{81}Co_{19}$ sample turned out to be $8.3 \pm 2.57 \text{ nm}$ (please see Figure S3 or the TEM and HAADF-STEM images of this sample). We have further analyzed $Pt_{60}Mn_{1.7}Co_{38.3}$, $Pt_{83}Mn_1Co_{16}$, $Pt_{65}Mn_{0.92}Co_{34.08}$, $P_{74.2}Mn_{0.9}Co_{24.9}$, and $Pt_{74}Mn_{0.8}Co_{25.2}$ samples by elemental mapping (Figure S4) and EDS line scanning (Figure S5) to know the distribution of Pt, Mn, and Co in them. These results unambiguously establish the simultaneous presence of Pt, Mn, and Co throughout the examined area in all these samples. It is worth mentioning that the weak signal of Mn was possibly due to the low amount of Mn present in the $Pt_{100-x}(MnCo)_x$ ($16 < x < 41$) NPs.

The $Pt_{100-x}(MnCo)_x$ ($16 < x < 41$) alloys were further subjected to XPS analysis. The detailed discussion about XPS analysis is given in the SI, Figures S6 and S7. In the $Pt_{60}Mn_{1.7}Co_{38.3}$ catalyst, the Pt spectra after deconvolution shows four peaks at 71.20, 72.44, 74.48, and 75.46 eV, of which the peaks at 71.20 and 74.48 eV correspond to the Pt^0 state and those at 72.44 and 75.46 eV correspond to the Pt^{+2} state.⁴¹ XPS spectra of the $Pt_{60}Mn_{1.7}Co_{38.3}$ catalyst mainly show the presence of metallic Pt^0 (Figure S6a). The less noble metals Co and Mn, however, exist mainly in an oxidized state (Figure S6b,c). Despite the presence of Co and Mn in the oxidized state, XRD analysis does not show any distinct peak for metal oxide, confirming the formation of metal alloys as the main material and the oxides being likely present on the surface as detected by XPS. This contention is also supported by the lower binding energies noticed for the Pt 4f peaks in all the XPS spectra of the $Pt_{100-x}(MnCo)_x$ alloys (Figure S6d). This clearly suggests the electron transfer process occurring from Co and Mn to Pt, making it electron-rich.^{42,43} The deconvoluted XPS spectra for the remaining $Pt_{100-x}(MnCo)_x$ ($16 < x < 41$) alloys along with comm. Pt/C are shown in the SI, Figure S7, along with the fraction of Pt^0 and Pt^{+2} content in each catalyst (Figure S7f).

3.2. Electrocatalytic Properties of $Pt_{100-x}(MnCo)_x$ Alloys. The ECSA of all carbon-loaded $Pt_{100-x}(MnCo)_x$ ($16 < x < 41$) alloys, along with comm. Pt/C and $Pt_{81}Co_{19}$ -NPs/C, were determined by a CV experiment in N_2 -saturated 0.5 M H_2SO_4 solution at 50 mV s^{-1} and the CVs (after stabilization over several cycles) obtained are shown in Figure S8. The electrochemical surface area (m^2/g) was calculated using the monolayer charge on platinum ($210 \mu\text{C}/\text{cm}^2$), the loading of platinum, and the integrated charge in the hydrogen adsorption and desorption region. The ECSA for comm. 20% Pt/C and $Pt_{81}Co_{19}/C$, $Pt_{60}Mn_{1.7}Co_{38.3}/C$, $Pt_{83}Mn_1Co_{16}/C$, $Pt_{65}Mn_{0.92}Co_{34.08}/C$, $P_{74.2}Mn_{0.9}Co_{24.9}/C$, and $Pt_{74}Mn_{0.8}Co_{25.2}/C$ was found to be 46.25, 17, 8, 18, 12, 12, and $17 \text{ m}^2/\text{g}$, respectively. The reduction in ECSA values for $Pt_{100-x}(MnCo)_x/C$ alloys compared to the value for comm. Pt/C, even after normalization with only Pt mass, indicates that on the surface of the catalyst, Mn and Co atoms are also present along with Pt.

The process by which methanol oxidizes in an acidic environment can be broken down into a number of steps.^{25,44}

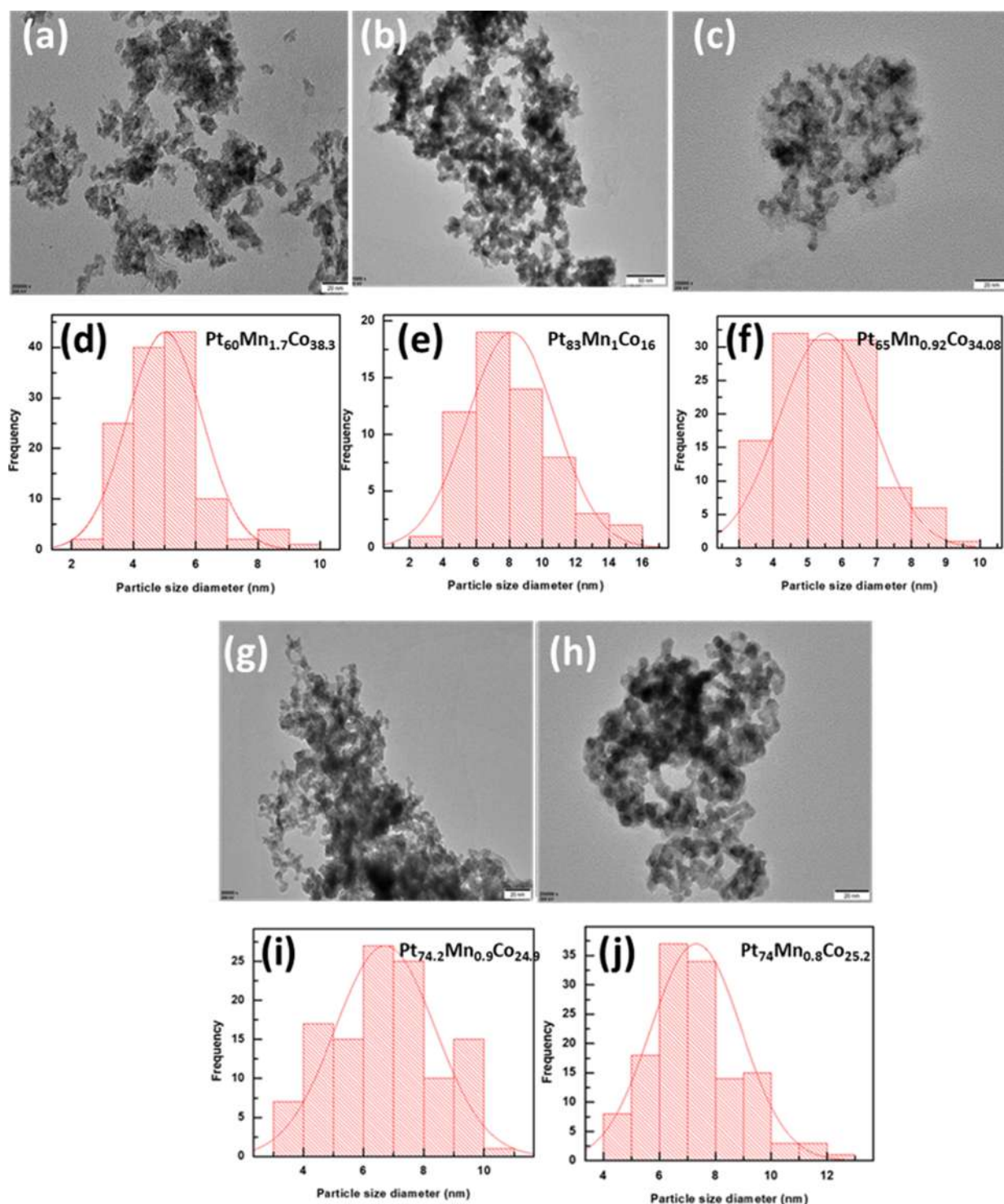


Figure 2. (a–j) TEM images and corresponding particle size distribution plots of $\text{Pt}_{100-x}(\text{MnCo})_x$ ($16 < x < 41$) alloys.

1. Methanol molecules electroadsorb on a Pt electrode, resulting in the generation of intermediates including $-\text{CHO}$, $-\text{COOH}$, $-\text{CO}$, etc.
2. Generation of Pt-OH on the catalyst surface as a result of water breakdown, followed by hydroxyl group participation in the oxidation of intermediate products.
3. Interaction of Pt-OH with intermediates resulting in the formation of CO_2 , and its elimination.

The most common intermediate formed during MOR is CO. The Pt catalyst surface becomes chemisorbed with CO

molecules, blocking the catalyst's active surface area and decreasing its activity. Doping the Pt catalyst with different noble metals (Pd, Ru, and Au) and some transition group d-metals (Cu, Ni, Fe, Mn, Co, etc.) helps the removal of this CO from the surface, enabling its oxidation to CO_2 . The catalytic activity for MOR of $\text{Pt}_{100-x}(\text{MnCo})_x/\text{C}$ ($16 < x < 41$) was investigated in 1 M methanol and 0.5 M H_2SO_4 solution, and the respective CV profiles are shown in Figure 3a. From CV traces, it can be observed that all the catalysts show two well-defined characteristic oxidation peaks, one in the forward

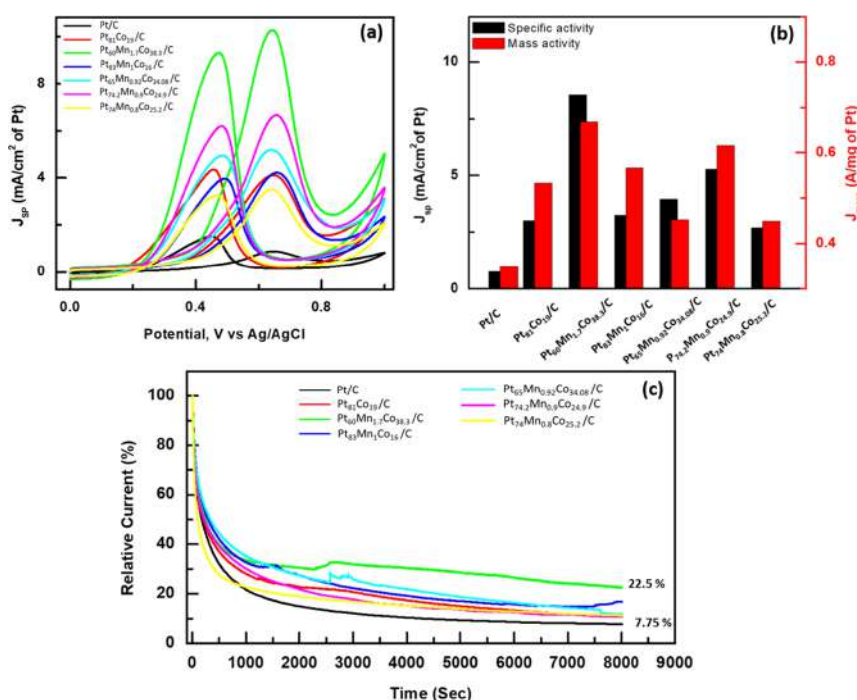


Figure 3. (a) CV profiles for MOR measured using comm. Pt/C and $\text{Pt}_{100-x}(\text{MnCo})_x/\text{C}$ ($16 < x < 41$) as a catalyst in 0.5 M H_2SO_4 and 1 M methanol. (b) Corresponding J_{sp} and J_{mass} for comm. Pt/C and $\text{Pt}_{100-x}(\text{MnCo})_x/\text{C}$ ($16 < x < 41$). (c) CA curves for comm. Pt/C and $\text{Pt}_{100-x}(\text{MnCo})_x/\text{C}$ ($16 < x < 41$) measured for 8000 s obtained by normalizing the initial current density value to 100% vs time.

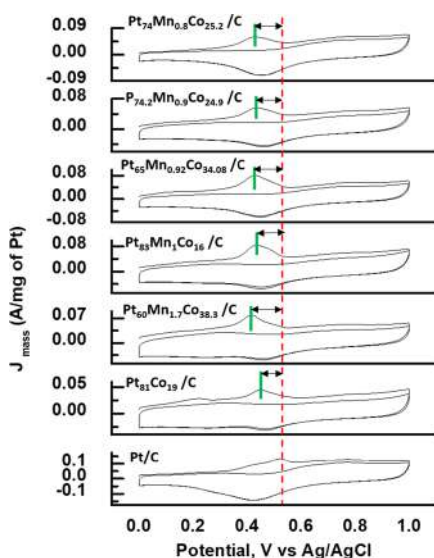


Figure 4. CO-stripping CV curves in N_2 -saturated 0.5 M H_2SO_4 solution for $\text{Pt}_{100-x}(\text{MnCo})_x/\text{C}$ ($16 < x < 41$) catalysts.

direction (anodic scan- I_f) and other oxidation peak in the backward direction (cathodic scan- I_b). Generally, the current observed in the forward direction is used to evaluate the activity of the catalyst toward MOR. The current obtained in the backward direction is related to the amount of residual unoxidized CO. Therefore, more the height of the reverse peak, more the poisoning. For all $\text{Pt}_{100-x}(\text{MnCo})_x/\text{C}$ ($16 < x < 41$) samples, it can be observed that the reverse peak is shifted to higher potential with lower current values, which clearly indicate the less amount of residual CO and hence less poisoning of the catalyst as compared to Pt/C.

The current densities were processed both in terms of mass and specific activity, as represented in Figure 3b. The mass activity of $\text{Pt}_{60}\text{Mn}_{1.7}\text{Co}_{38.3}/\text{C}$ was found to be 0.67A/mg, which is 1.3 and 1.9 times higher than that of $\text{Pt}_{81}\text{Co}_{19}/\text{C}$ (0.53 A/mg) and comm. Pt/C (0.35 A/mg), respectively. In the SI, a comparison table of the $\text{Pt}_{100-x}(\text{MnCo})_x/\text{C}$ ($16 < x < 41$) catalyst with other trimetallic platinum catalysts is provided (please see Table S2). Furthermore, the ratio of the forward peak current (I_f) to the backward current (I_b) is generally used to judge the tolerance of the catalyst toward CO.⁴⁵ The higher the value of I_f/I_b , the more catalyst is considered tolerant toward CO. I_f/I_b values for comm. 20% Pt/C and $\text{Pt}_{81}\text{Co}_{19}/\text{C}$, $\text{Pt}_{60}\text{Mn}_{1.7}\text{Co}_{38.3}/\text{C}$, $\text{Pt}_{83}\text{Mn}_1\text{Co}_{16}/\text{C}$, $\text{Pt}_{65}\text{Mn}_{0.92}\text{Co}_{34.08}/\text{C}$, $\text{Pt}_{74.2}\text{Mn}_{0.9}\text{Co}_{24.9}/\text{C}$, and $\text{Pt}_{74}\text{Mn}_{0.8}\text{Co}_{25.2}/\text{C}$ were found to be 0.50, 0.74, 0.94, 0.86, 0.85, 0.89, and 0.87, respectively.

Higher I_f/I_b values for $\text{Pt}_{100-x}(\text{MnCo})_x/\text{C}$ ($16 < x < 41$) as compared to comm. 20% Pt/C clearly indicate the superior CO tolerance of $\text{Pt}_{100-x}(\text{MnCo})_x/\text{C}$ ($16 < x < 41$) catalysts. Furthermore, the onset potential of the forward peak (I_f) in MOR for all $\text{Pt}_{100-x}(\text{MnCo})_x/\text{C}$ ($16 < x < 41$) catalysts were also found to be lower as compared to comm. 20% Pt/C (Figure S9). Table S3 summarizes the electrocatalytic performance of $\text{Pt}_{100-x}(\text{MnCo})_x/\text{C}$ ($16 < x < 41$) catalysts and comm. 20% Pt/C.

Apart from the mass and specific activities, electrochemical durability is another important parameter that is vital to ascertaining the effectiveness of a catalyst. A CA test can be used to study the rate of CO-poisoning during MOR and catalyst stability at a fixed potential. Figure 3c displays the CA profiles for all catalysts recorded at the peak potential for 8000 s in a mixture of 1 M methanol and 0.5 M H_2SO_4 solution. All the samples displayed a sharp drop in current at first, followed by a gentler decay. In Figure 3c, the current retention vs time graph is presented. In the literature, it is proclaimed that the decrease of current with time is due to the accumulation and

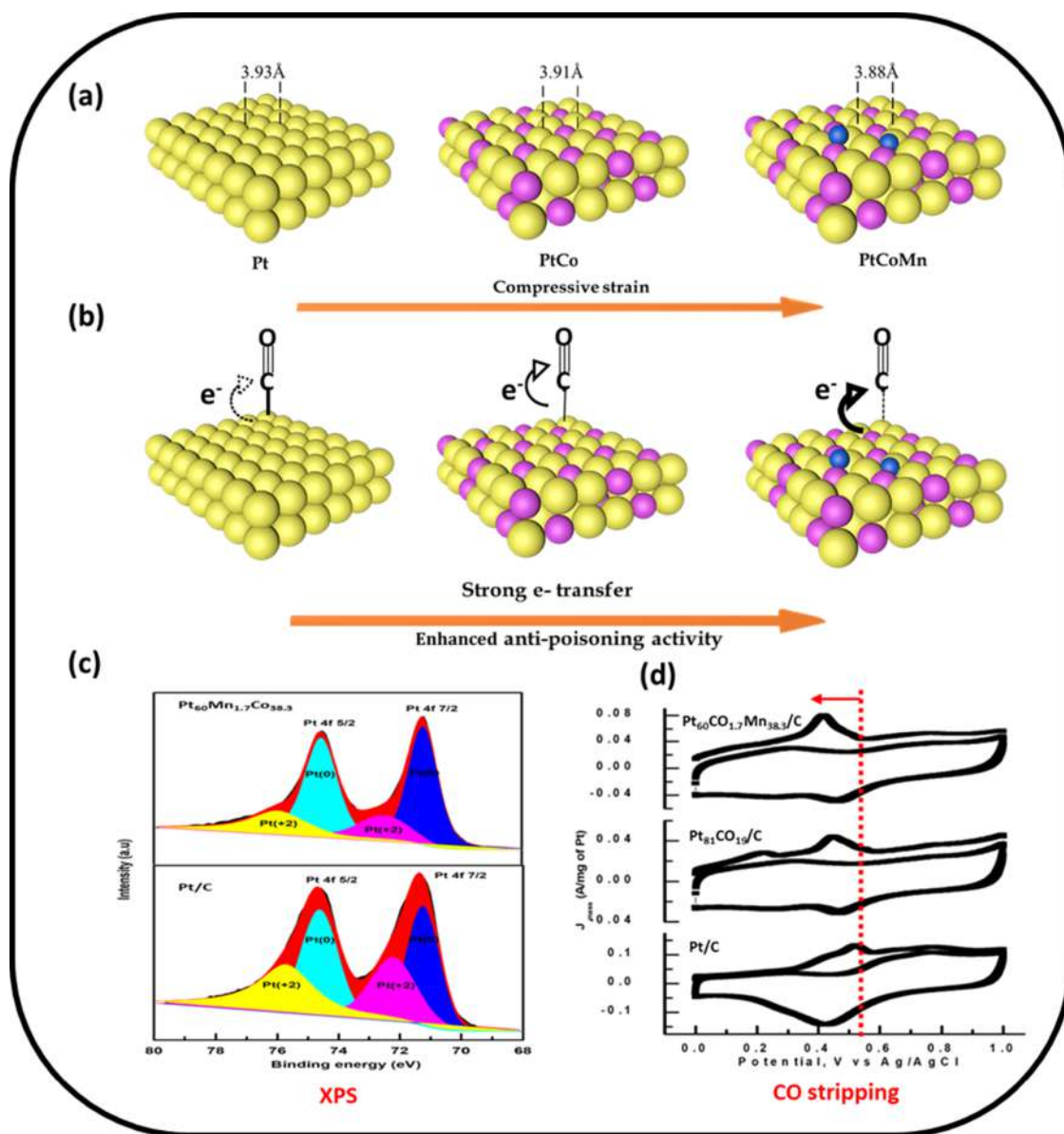


Figure 5. Schematic representation to explain the reason for enhanced activity of trimetallic alloys as compared to Pt/C (a) compressive strain, (b) charge transfer illustration, (c) XPS Pt 4f scan, and (d) Co stripping curves for Pt/C, Pt₈₁Co₁₉/C, and Pt₆₀Mn_{1.7}Co_{38.3}/C, respectively.

adsorption of intermediates such as CO, CHO, and COOH^{46–49,40} species on the catalyst surface, which results in a reduction in activity and affects the durability of the catalyst. Figure 3c clearly demonstrates that among all Pt_{100-x}(MnCo)_x/C catalysts, Pt₆₀Mn_{1.7}Co_{38.3}/C has the highest retention of initial activity (22.5%) after 8000 s, whereas Pt/C has the lowest (7.75%). Furthermore, 1000 cycle accelerated durability tests were performed, and the electrochemical findings are shown in SI Figures S10 and S11. After 1000 cycles, Pt₆₀Mn_{1.7}Co_{38.3}/C exhibits the maximum activity retention of roughly 55%, which is higher than comm. Pt/C. The research on catalyst stability in accelerated durability testing revealed that trimetallic catalysts degrade less than conventional Pt/C catalysts. This was also clearly demonstrated by measuring the CV in 0.5 M H₂SO₄ solution before and after the accelerated stability test (SI Figure S12). The ECSA of comm. Pt/C has dropped, while it almost remains the same for the Pt_{100-x}(MnCo)_x/C (16 < x < 41) catalyst. Pt₆₀Mn_{1.7}Co_{38.3}/C was analyzed by TEM and ICP following

the long-term stability test to further investigate the electrochemical changes in the surface structure and composition. SI Figure S13 depicts the elemental mapping for Pt₆₀Mn_{1.7}Co_{38.3}/C prior to and following the stability test. The figure clearly shows that all three elements were present. Pt₆₀Mn_{1.7}Co_{38.3}/C had the same (111) facet lattice fringes (0.2 nm) before and after the durability study (SI Figure S14). ICP analysis performed on samples before and after the durability test, nonetheless, shows that some amount of the Mn metal does get leached.

In addition to the above experiment, CO oxidation was performed to study the tolerance of the Pt_{100-x}(MnCo)_x/C (16 < x < 41) catalyst after methanol electrooxidation. The CO stripping experiment was carried out in 0.5 M H₂SO₄ solution at a CO adsorption potential of -0.2 V vs Ag/AgCl for 10 min and a sweep rate of 50 mV s⁻¹. As shown in Figure 4, comm. Pt/C shows a small peak around 0.53 V. For Pt₈₁Co₁₉/C, the CO stripping peak shifted slightly to a lower potential value of 0.45 V, and for Pt₆₀Mn_{1.7}Co_{38.3}/C,

Pt₈₃Mn₁Co₁₆/C, Pt₆₅Mn_{0.92}Co_{34.08}/C, Pt_{74.2}Mn_{0.9}Co_{24.9}/C, and Pt₇₄Mn_{0.8}Co_{25.2}/C, the peak was further shifted to a lower potential of 0.41, 0.43, 0.43, 0.44, and 0.43 V, respectively. The low CO-stripping peak potential of Pt₆₀Mn_{1.7}Co_{38.3}/C when compared to all other alloys confirmed that CO is probably weakly adsorbed on its surface compared to other compositions tested, resulting in its better catalytic activity for MOR. All the above results show that all Pt_{100-x}(MnCo)_x/C (16 < x < 41) catalysts have better long-term stability and CO tolerance as compared to comm. Pt/C.

Based on the outcomes of CV and CA evaluations of the catalytic activity, stability, and tolerance to CO, it was found that despite having lower ECSA values compared to comm. Pt/C, trimetallic catalysts have the highest activity and stability for MOR. In our opinion, the increase in activity and stability of the Pt_{100-x}(MnCo)_x/C (16 < x < 41) catalyst is primarily attributable to the following factors:

As the atomic radii of Co and Mn are less than those of Pt, the resulting Pt_{100-x}(MnCo)_x/C (16 < x < 41) catalyst will compress the surface Pt layer. As previously stated, the lattice constant computed for all Pt_{100-x}(MnCo)_x/C (16 < x < 41) catalysts is less than that of comm. Pt/C. This confirms the presence of compressive strain to some extent. According to Nørskov and co-workers, the strain effect causes changes in the metal d-band by changing the geometry of the electron population. The metal–adsorbate bond strength has been observed to alter as a result of d-band center shifts caused by strain variation in the metal structure. Such alterations eventually result in changes in adsorption/desorption capabilities of activating reactants or intermediates,^{50–52} which is one of the important features influencing the electrocatalytic activity. This finding is consistent with the existing XPS study of the Pt 4f XPS spectra and the CO stripping experiment. It is obvious that the higher the proportion of the metallic state on the catalyst surface, the more active sites for MOR electrocatalysis. As discussed earlier in the XPS spectra, as compared to comm. Pt/C, the Pt_{100-x}(MnCo)_x/C (16 < x < 41) catalyst shows a negative shift in binding energy due to the difference in electronegativity. The negative shift in the binding energy of the Pt_{100-x}(MnCo)_x/C (16 < x < 41) catalyst is due to the role of Co and Mn as electron donors and Pt as an electron acceptor. The incorporation of extra transition metals like Mn and Co into Pt in a Pt_{100-x}(MnCo)_x/C (16 < x < 41) catalyst is expected to modify the electronic structure of the Pt surface, promote reaction kinetics, facilitate electron transfer, and also accelerate the removal of CO molecules to improve MOR catalytic activity, as has been confirmed in numerous reports.^{21–25,53} These findings, as summarized in Figure 5, help to explain why the trimetallic Pt_{100-x}(MnCo)_x/C (16 < x < 41) catalyst is active as compared to Pt/C. Previously, we have reported a DFT study for PtCo binary alloy catalysts with different compositions and tested them as catalysts for MOR.¹⁶ In this study, it was concluded that an increase in electron density on Pt significantly improves the electrochemical performance of Pt-based catalysts.^{16,41,42} The current results also endorse this postulation.

4. CONCLUSIONS

In summary, Pt_{100-x}(MnCo)_x (16 < x < 41) catalysts with different elemental compositions were successfully prepared via borohydride reduction followed by hydrothermal treatment. TEM and XRD analyses clearly demonstrate the formation of an alloy with a particle size less than 10 nm. Among all the

compositions prepared, the Pt₆₀Mn_{1.7}Co_{38.3} catalyst exhibited superior mass activity toward MOR, which was 1.3 and 1.9 times higher than those of Pt₈₁Co₁₉/C and comm. Pt/C, respectively. Moreover, the CA test for durability and the CO oxidation reaction for CO tolerance demonstrate that all synthesized Pt_{100-x}(MnCo)_x/C (16 < x < 41) catalysts show better current retention when compared with comm. Pt/C. Here again, the sample with Pt₆₀Mn_{1.7}Co_{38.3}/C was the best among the compositions studied. This improved performance of the Pt_{100-x}(MnCo)_x/C (16 < x < 41) catalyst can be attributed to the synergistic effect of Co and Mn on the Pt lattice.

■ ASSOCIATED CONTENT

Supporting Information

The Supporting Information is available free of charge at <https://pubs.acs.org/doi/10.1021/acsami.3c01140>.

TGA analysis of the sample to check metal loading on carbon; details regarding synthesis of the alloy; XRD and CV profiles for the Pt₉₀Mn_{2.7}Co_{6.5} sample; HAADF-STEM image, EDS line scan profile along the red line, and elemental mapping for Pt₈₁Co₁₉; elemental mapping for the Pt_{100-x}(MnCo)_x/C (16 < x < 41) catalyst; HAADF-STEM image and EDS line scan profile along the red line for the Pt_{100-x}(MnCo)_x/C (16 < x < 41) catalyst; high-resolution XPS peak for the Pt₆₀Mn_{1.7}Co_{38.3} catalyst; deconvoluted XPS spectra for comm. Pt/C along with remaining Pt_{100-x}(MnCo)_x (16 < x < 41); CV profile for commercial Pt/C and all Pt_{100-x}(MnCo)_x/C (16 < x < 41) catalysts measured in 0.5 M H₂SO₄ solution; magnified CV profiles of the forward scan for comm. Pt/C and Pt_{100-x}(MnCo)_x/C (16 < x < 41) to determine onset potentials; comparison table of the Pt_{100-x}(MnCo)_x/C (16 < x < 41) catalyst with other trimetallic platinum catalysts; electrocatalytic performance of comm. Pt/C and Pt_{100-x}(MnCo)_x/C (16 < x < 41); 1000 cycle accelerated durability tests for Pt/C and Pt_{100-x}(MnCo)_x/C (16 < x < 41) catalysts; mass activity and percent activity retention before and after the accelerated durability test; CV recorded in 0.5 M H₂SO₄ solution at 50 mV s⁻¹ before and after the accelerated durability test; elemental mapping for Pt₆₀Mn_{1.7}Co_{38.3}/C prior to and following the accelerated durability test; and TEM image of Pt₆₀Mn_{1.7}Co_{38.3}/C before and after the accelerated durability test (PDF)

■ AUTHOR INFORMATION

Corresponding Author

Bhagavatula L. V. Prasad – Physical and Materials Chemistry Division, National Chemical Laboratory (CSIR-NCL), Pune 411008, India; Academy of Scientific and Innovation Research (AcSIR), Ghaziabad 201002, India; Centre for Nano and Soft Matter Sciences, Bengaluru 562162, India; orcid.org/0000-0002-3115-0736; Phone: +91-80-29630201; Email: pl.bhagavatula@ncl.res.in, pl.bhagavatula@cens.res.in

Author

Pooja Deshpande – Physical and Materials Chemistry Division, National Chemical Laboratory (CSIR-NCL), Pune 411008, India; Academy of Scientific and Innovation Research (AcSIR), Ghaziabad 201002, India

Complete contact information is available at:
<https://pubs.acs.org/10.1021/acsami.3c01140>

Notes

The authors declare no competing financial interest.

ACKNOWLEDGMENTS

P.D. thanks the DST-INSPIRE program for fellowship and Science and Engineering Research Board (Project grant no. CRG/2022/001633) for funding.

REFERENCES

- (1) Reddington, E.; Sapienza, A.; Gurau, B.; Viswanathan, R.; Sarangapani, S.; Smotkin, E. S.; Mallouk, T. E. Combinatorial electrochemistry: A Highly Parallel, Optical Screening Method for Discovery of Better Electrocatalysts. *Science* **1998**, *280*, 1735–1737.
- (2) Blum, A.; Duvdevani, T.; Philosoph, M.; Rudoy, N.; Peled, E. Water-neutral Micro Direct-Methanol Fuel Cell (DMFC) for Portable Applications. *J. Power Sources* **2003**, *117*, 22–25.
- (3) Seo, S. H.; Lee, C. S. Effect of Operating Parameters on The Direct Methanol Fuel Cell Using Air or Oxygen as An Oxidant Gas. *Energy Fuels* **2008**, *22*, 1212–1219.
- (4) Liu, Z.; Tang, H. L.; Pan, M. Synthesis and Characterization of PDDA-Stabilized Pt Nanoparticles for Direct Methanol Fuel Cells. *Electrochim. Acta* **2006**, *51*, 5721–5730.
- (5) Huang, H.; Wang, X. Recent Progress on Carbon-based Support Materials for Electrocatalysts of Direct Methanol Fuel Cells. *J. Mater. Chem. A* **2014**, *2*, 6266–6291.
- (6) Wang, A. J.; Ju, K. J.; Zhang, Q. L.; Song, P.; Wei, J.; Feng, J. J. Folic Acid Bio-inspired FRoute for Facile Synthesis of AuPt Nanodendrites As Enhanced Electrocatalysts for Methanol and Ethanol Oxidation Reactions. *J. Power Sources* **2016**, *326*, 227–234.
- (7) Zhang, J. J.; Sui, X. L.; Huang, G. S.; Gu, D. M.; Wang, Z. B. Hierarchical Carbon Coated Molybdenum Dioxide Nanotubes as a Highly Active and Durable Electrocatalytic Support for Methanol Oxidation. *J. Mater. Chem. A* **2017**, *5*, 4067–4074.
- (8) Sun, X.; Zhu, X.; Zhang, N.; Guo, J.; Guo, S.; Huang, X. Controlling and Self-Assembling of Monodisperse Platinum Nanocubes as Efficient Methanol Oxidation Electrocatalysts. *Chem. Commun.* **2017**, *51*, 3529–3532.
- (9) Feng, L.; Li, K.; Chang, J.; Liu, C.; Xing, W. Nanostructured PtRu/C Catalyst Promoted by CoP as an Efficient and Robust Anode Catalyst in Direct Methanol Fuel Cells. *Nano Energy* **2015**, *15*, 462–469.
- (10) Yin, Y.; Liu, J.; Jiang, G. Sunlight-induced Reduction of Ionic Ag and Au to Metallic Nanoparticles by Dissolved Organic Matter. *ACS Nano* **2012**, *6*, 7910–7919.
- (11) Jiang, K.; Zhao, D.; Guo, S.; Zhang, X.; Zhu, X.; Guo, J.; Lu, G.; Huang, X. Efficient Oxygen Reduction Catalysis by Subnanometer Pt Alloy Nanowires. *Sci. Adv.* **2017**, *3*, No. e1601705.
- (12) Maiyalagan, T. Silicotungstic Acid Stabilized Pt–Ru Nanoparticles Supported on Carbon Nanofibers Electrodes for Methanol Oxidation. *Int. J. Hydrogen Energy* **2009**, *34*, 2874–2879.
- (13) Nagashree, K. L.; Raviraj, N. H.; Ahmed, M. F. Carbon Paste Electrodes Modified by Pt and Pt–Ni Microparticles Dispersed in Polyindole Film for Electrocatalytic Oxidation of Methanol. *Electrochim. Acta* **2010**, *55*, 2629.
- (14) Guo, X.; Guo, D. J.; Qiu, X. P.; Chen, L. Q.; Zhu, W. T. A Simple One-step Preparation of High Utilization AuPt Nanoparticles Supported on MWCNTs for Methanol Oxidation in Alkaline Medium. *Electrochem. Commun.* **2008**, *10*, 1748–1751.
- (15) Lei, Y.; Zhao, G.; Tong, X.; Liu, M.; Li, D.; Geng, R. High Electrocatalytic Activity of Pt–Pd Binary Spherocrystals Chemically Assembled in Vertically Aligned TiO₂ Nanotubes. *ChemPhysChem* **2010**, *11*, 276–284.
- (16) Dalavi, S. B.; Agarwal, S.; Deshpande, P.; Joshi, K.; Prasad, B. L. V. Disordered but Efficient: Understanding the Role of Structure and Composition of the Co–Pt Alloy on the Electrocatalytic Methanol Oxidation Reaction. *J. Phys. Chem. C* **2021**, *125*, 7611–7624.
- (17) Huang, L.; Jiang, Z.; Gong, W.; Shen, P. K. Facile Fabrication of Radial PtCo Nanodendrites for Enhanced Methanol Oxidation Electrocatalysis. *ACS Appl. Nano Mater.* **2018**, *1*, 5019–5026.
- (18) Lee, E.; Kim, S.; Jang, J. H.; Park, H. U.; Matin, M. A.; Kim, Y. T.; Kwon, Y. U. Effects of particle proximity and composition of Pt–M (M= Mn, Fe, Co) nanoparticles on electrocatalysis in methanol oxidation reaction. *J. Power Sources* **2015**, *294*, 75–81.
- (19) Huang, X.; Zhao, Z.; Cao, L.; Chen, Y.; Zhu, E.; Lin, Z.; Li, M.; Yan, A.; Zettl, A.; Wang, Y. M.; Duan, X.; Mueller, T.; Huang, Y. High-Performance Transition Metal–Doped Pt₃Ni Octahedra for Oxygen Reduction Reaction. *Science* **2015**, *348*, 1230–1234.
- (20) Li, K.; Li, X.; Huang, H.; Luo, L.; Li, X.; Yan, X.; Ma, C.; Si, R.; Yang, J.; Zeng, J. One-Nanometer-Thick PtNiRh Trimetallic Nanowires with Enhanced Oxygen Reduction Electrocatalysis in Acid Media: Integrating Multiple Advantages into One Catalyst. *J. Am. Chem. Soc.* **2018**, *140*, 16159–16167.
- (21) Huang, L.; Wei, M.; Hu, N.; Tsiakaras, P.; Shen, P. K. Molybdenum-Modified and Vertex-Reinforced Quaternary Hexapod Nano-Skeletons as Efficient Electrocatalysts for Methanol Oxidation and Oxygen Reduction Reaction. *Appl. Catal., B* **2019**, *258*, No. 117974.
- (22) Liao, W.; Zhou, S.; Wang, Z.; Liu, F.; Cao, J.; Wang, Q. Composition-Controlled Effects of Pb Content in PtPbRu Trimetallic Nanoparticles on the Electrocatalytic Oxidation Performance of Methanol. *Fuel* **2022**, *308*, No. 122073.
- (23) Feng, H.; Luo, Y.; Yan, B.; Guo, H.; He, L.; Tian, Z. Q.; Tsiakaras, P.; Shen, P. K. Highly Stable Cathodes for Proton Exchange Membrane Fuel Cells: Novel Carbon Supported Au@PtNiAu Concave Octahedral Core-Shell Nanocatalyst. *J. Colloid Interface Sci.* **2022**, *626*, 1040–1050.
- (24) Ren, Y.; Li, B.; Lv, C.; Gao, F.; Yang, X.; Li, L.; Lu, Z.; Yu, X.; Zhang, X. Defect-Rich PtPdCu Flower-like Nanoframes with Enhanced Electrocatalytic Activity for Methanol Oxidation. *Appl. Surf. Sci.* **2022**, *593*, No. 153404.
- (25) Menshikov, V. S.; Belenov, S. V.; Nikulin, A. Y. Effect of the Morphology and Composition of Trimetallic PtCuAu/C Catalysts on the Activity and Stability of the Methanol Oxidation Reaction. *Condens. Matter Interphases* **2022**, *24*, 76–87.
- (26) Stamenkovic, V.; Mun, B. S.; Mayrhofer, K. J.; Ross, P. N.; Markovic, N. M.; Rossmeisl, J.; Greeley, J.; Nørskov, J. K. Changing the Activity of Electrocatalysts for Oxygen Reduction by Tuning the Surface Electronic Structure. *Angew. Chem., Int. Ed.* **2006**, *118*, 2963–2967.
- (27) Najafpour, M. M.; Moghaddam, A. N.; Yang, Y. N.; Aro, E. M.; Carpentier, R.; Eaton-Rye, J. J.; Lee, C. H.; Allakhverdiev, S. I. Biological Water-Oxidizing Complex: A Nano-Sized Manganese–Calcium Oxide in a Protein Environment. *Photosynth. Res.* **2012**, *114*, 1–13.
- (28) Najafpour, M. M.; Allakhverdiev, S. I. Manganese Compounds as Water Oxidizing Catalysts for Hydrogen Production via Water Splitting: From Manganese Complexes to Nano-Sized Manganese Oxides. *Int. J. Hydrogen Energy* **2012**, *37*, 8753–8764.
- (29) Stamenkovic, V. R.; Mun, B. S.; Arenz, M.; Mayrhofer, K. J.; Lucas, C. A.; Wang, G.; Ross, P. N.; Markovic, N. M. Trends in Electrocatalysis On Extended and Nanoscale Pt-Bimetallic Alloy Surfaces. *Nat. Mater.* **2007**, *6*, 241–247.
- (30) Shan, A.; Huang, S.; Zhao, H.; Jiang, W.; Teng, X.; Huang, Y.; Chen, C.; Wang, R.; Lau, W.-M. Atomic-Scaled Surface Engineering Ni-Pt Nanoalloys Towards Enhanced Catalytic Efficiency for Methanol Oxidation Reaction. *Nano Res.* **2020**, *13*, 3088–3097.
- (31) Kang, Y.; Murray, C. B. Synthesis and Electrocatalytic Properties of Cubic Mn–Pt Nanocrystals (Nanocubes). *J. Am. Chem. Soc.* **2010**, *132*, 7568–7569.
- (32) Gao, F.; Zhang, Y.; Ren, F.; Song, T.; Du, Y. Tiny Ir Doping of Sub-One-Nanometer PtMn Nanowires: Highly Active and Stable Catalysts for Alcohol Electrooxidation. *Nanoscale* **2020**, *12*, 12098–12105.

- (33) Peng, K.; Bhuvanendran, N.; Ravichandran, S.; Zhang, W.; Ma, Q.; Xu, Q.; Xing, L.; Khotseng, L.; Su, H. Bimetallic Pt₃Mn Nanowire Network Structures with Enhanced Electrochemical Performance for Methanol Oxidation. *Int. J. Hydrogen Energy* **2020**, *45*, 30455–30462.
- (34) Fan, Q.; Strasser, P.; Gorer, A.; Devenney, M.; Chondroudis, K.; Giaquinta, D. M.; He, T.; Oyanagi, H.; Urata, K.; Iwasaki, K.; Fukuda, H. Fuel Cell Electrocatalyst of pt-mn-co. U.S. Patent, 7635533 B2, 2009.
- (35) Mohanraju, K.; Cindrella, L. One-Pot Surfactant-Free Synthesis of High Surface Area Ternary Alloys, PtMCo/C (M= Cr, Mn, Fe, Ni, Cu) with Enhanced Electrochemical Activity and Durability for PEM Fuel Cell Application. *Int. J. Hydrogen Energy* **2016**, *41*, 9320–9331.
- (36) Ammam, M.; Easton, E. B. Oxygen Reduction Activity of Binary PtMn/C, Ternary PtMnX/C (X= Fe, Co, Ni, Cu, Mo and, Sn) and Quaternary PtMnCuX/C (X= Fe, Co, Ni, and Sn) and PtMnMoX/C (X= Fe, Co, Ni, Cu and Sn) Alloy Catalysts. *J. Power Sources* **2013**, *236*, 311–320.
- (37) Bonakdarpour, A.; Stevens, K.; Vernstrom, G. D.; Atanasoski, R.; Schmoekkel, A. K.; Debe, M. K.; Dahn, J. R. Oxygen Reduction Activity of Pt and Pt–Mn–Co Electrocatalysts Sputtered on Nano-Structured Thin Film Support. *Electrochim. Acta* **2007**, *53*, 688–694.
- (38) Ammam, M.; Easton, E. B. Ternary PtMnX/C (X= Fe, Co, Ni, Cu, Mo and, Sn) Alloy Catalysts for Ethanol Electrooxidation. *J. Electrochem. Soc.* **2012**, *159*, B635.
- (39) Lim, D. H.; Choi, D. H.; Lee, W. D.; Lee, H. I. A New Synthesis of a Highly Dispersed and CO Tolerant PtSn/C Electrocatalyst for Low-Temperature Fuel Cell; Its Electrochemical Activity and Long-Term Durability. *Appl. Catal.* **2009**, *89*, 484–493.
- (40) Ravichandran, S.; Bhuvanendran, N.; Xu, Q.; Maiyalagan, T.; Su, H. Improved Methanol Electrooxidation Catalyzed by Ordered Mesoporous Pt–Ru–Ir Alloy Nanostructures with Trace Ir Content. *Electrochim. Acta* **2021**, *394*, No. 139148.
- (41) Shen, C. T.; Wang, K. W.; Tseng, C. J.; Lee, K. R.; Hsueh, Y. J. The Oxygen Reduction Reaction of Ordered Porous Carbon-Supported PtSn Catalysts. *RSC Adv.* **2016**, *6*, 44205–44211.
- (42) Fan, J.; Qi, K.; Zhang, L.; Zhang, H.; Yu, S.; Cui, X. Engineering Pt/Pd Interfacial Electronic Structures for Highly Efficient Hydrogen Evolution and Alcohol Oxidation. *ACS Appl. Mater. Interfaces* **2017**, *9*, 18008–18014.
- (43) Wang, Z.; Yao, X.; Kang, Y.; Xia, D.; Gan, L. Rational Development of Structurally Ordered Platinum Ternary Intermetallic Electrocatalysts for Oxygen Reduction Reaction. *Catalysts* **2019**, *9*, 569.
- (44) Hamnett, A. Mechanism and Electrocatalysis in the Direct Methanol Fuel Cell. *Catal. Today* **1997**, *38*, 445–457.
- (45) Mancharan, R.; Goodenough, J. B. Methanol oxidation in acid on ordered NiTi. *J. Mater. Chem.* **1992**, *2*, 875–887.
- (46) Deshpande, P. S.; Chaudhari, V. R.; Prasad, B. L. V. Mechanistic Aspects of Methanol Electro-Oxidation Reaction through Cyclic Voltammetry: Is It Correct to Blame Carbon Monoxide for Catalyst Poisoning? *Energy Technol.* **2020**, *8*, No. 1900955.
- (47) Cuesta, A.; Escudero, M.; Lanova, B.; Baltruschat, H. Cyclic Voltammetry, FTIRS, and DEMS Study of the Electrooxidation of Carbon Monoxide, Formic Acid, and Methanol on Cyanide-Modified Pt (111) electrodes. *Langmuir* **2009**, *25*, 6500–6507.
- (48) Chen, Y. X.; Miki, A.; Ye, S.; Sakai, H.; Osawa, M. Formate, An Active Intermediate for Direct Oxidation of Methanol on Pt Electrode. *J. Am. Chem. Soc.* **2003**, *125*, 3680–3681.
- (49) Housmans, T. H.; Wonders, A. H.; Koper, M. T. Structure Sensitivity of Methanol Electrooxidation Pathways on Platinum: An On-Line Electrochemical Mass Spectrometry Study. *J. Phys. Chem. B* **2006**, *110*, 10021–10031.
- (50) Strasser, P.; Koh, S.; Anniyev, T.; Greeley, J.; More, K.; Yu, C.; Liu, Z.; Kaya, S.; Nordlund, D.; Ogasawara, H.; Toney, M. F.; Nilsson, A. Lattice-Strain Control of the Activity in Dealloyed Core–Shell Fuel Cell Catalysts. *Nat. Chem.* **2010**, *2*, 454–460.
- (51) Nilsson, A.; Pettersson, L. G. M.; Hammer, B.; Bligaard, T.; Christensen, C. H.; Nørskov, J. K. The Electronic Structure Effect in Heterogeneous Catalysis. *Catal. Lett.* **2005**, *100*, 111–114.
- (52) Abild-Pedersen, F.; Greeley, J.; Nørskov, J. K. Understanding the Effect of Steps, Strain, Poisons, and Alloying: Methane Activation on Ni Surfaces. *Catal. Lett.* **2005**, *105*, 9–13.
- (53) Wang, D.; Chen, Z.; Huang, Y. C.; Li, W.; Wang, J.; Lu, Z.; Gu, K.; Wang, T.; Wu, Y.; Chen, C.; Zhang, Y.; Huang, X.; Tao, L.; Dong, C. L.; Chen, J.; Singh, C. V.; Wang, S. Tailoring Lattice Strain in Ultra-Fine High-Entropy Alloys for Active and Stable Methanol Oxidation. *Sci. China Mater.* **2021**, *64*, 2454–2466.